Università degli studi di Pisa

Scuola di Ingegneria
Corso di Laurea in Ingegneria Nucleare

Neutronic investigations of MOX and LEU fuel assemblies for VVER reactors

RELATORI:
Prof. Valerio Giusti
Prof. Walter Ambrosini
Dott. Ing. Luigi Mercatali

Candidato:
Alessandro Venturini

ANNO ACCADEMICO 2013/2014

To my grandparents

Abstract

The loading of hybrid cores with Mixed Uranium Plutonium Oxide (MOX) and Low Enriched Uranium (LEU) fuels in commercial nuclear reactors requires well validated computational methods and codes capable to provide reliable predictions of the neutronics characteristics of such fuels in terms of reactivity conditions (k-inf), nuclide inventory and pin power generation over the entire fuel cycle length. Within the framework of Joint United States/Russian Fissile Materials Disposition Program an important task is to verify and validate neutronics codes for the use of MOX fuel in VVER-1000 reactors. Benchmark analyses are being performed for both computational benchmarks and experimental benchmarks.

In this thesis new solutions for the (UO_2+Gd) and (UO_2+PuO_2+Gd) fuel assemblies proposed within the "OECD VVER-1000 Burnup Computational Benchmark" are presented, these being representative of the designs that are expected to be used in the plutonium disposition mission. The objective is to test the SERPENT and SCALE codes against previously obtained solutions and to provide new reference solutions to the benchmark with modern nuclear data libraries.

The OECD UAM Benchmark was launched in 2005 with the objective of determining the uncertainty in the simulation of Light Water Reactors (LWRs) system calculations at all the stages of the coupled reactor physics—thermal hydraulics modelling. Within the framework of the "Neutronics Phase" of the Benchmark the solutions of some selected test cases at the cell physics and lattice physics levels are presented. The SCALE 6.2b3 code package has been used for the neutronics modelling of the selected exercises. Sensitivity and Uncertainty analysis (S/U) based on both the generalized perturbation theory and the statistical sampling methodology has been performed in order to assess the uncertainty of the computation of some selected reactor integral parameters due to the uncertainty in the basic nuclear data. These two methodologies have been also applied to the two assemblies described in the "OECD VVER-1000 Burnup Computational Benchmark" and to four different unit cells with different loadings of Gd and Pu.

As a general trend, it has been found that the main sources of uncertainty are the ^{238}U (n,γ) and the ^{239}Pu nubar for the UOX- and the MOX-fuelled test cases, respectively.

Acknowledgements

I am grateful to my supervisor, Dr. Luigi Mercatali, from whom I have learnt an immense amount. Without his support and assistance, the completion of this work would have been impossible. Likewise, my gratitude must be expressed to Dr. Markus Schlenker and Dr. Miriam Däubler whose advice and recommendations greatly contributed to my understanding of the codes used in this work. Furthermore, I am thankful to Prof. Luca Marocco, Dr. Ivan Alessio Maione, Dario Carloni and Bruno Gonfiotti for their suggestions and their help.

Also, my sincere thanks to Dr. Victor Hugo Sanchez Espinoza for the opportunity to study at the "Institut für Neutronenphysik und Reaktortechnik", Karlsruhe Institute of Technology.

At last, I want to thank my supervisors at the University of Pisa, Prof. Walter Ambrosini and Prof. Valerio Giusti, for their kindness and willingness to provide help and prompt responses to my requests.

My heartfelt thanks must be expressed to my family, for their continual support and encouragement.

Contents

List of Figures

LIST OF FIGURES

List of Tables

Chapter 1

Introduction

Mixed oxide (MOX) fuel has only been used on a large scale in the nuclear industry since the 1980's and to a much smaller extent with respect to the more conventional UO_2 fuel. In particular, the irradiation of MOX fuel in existing commercial nuclear reactors (essentially light water reactors) as a disposition method for surplus plutonium from the weapons programs is being pursued by the United States and the Russian Federation within the framework of a mutual agreement [Gehin 2004]. Due to the relatively scarce experience with MOX fuel in these two countries, particularly if compared with the one accumulated in Europe and Japan, an international Expert Group has been established at the OECD/NEA to facilitate the sharing of existing information and experience in the physics and fuel behaviour of MOX fuel as it relates to the disposition of weapons-grade (WG) plutonium. The Russian federation is being pursuing the deployment of WG MOX fuel in the VVER-1000 reactors and R&D activities are needed for the certification of the calculation codes which are envisioned to be used. As part of the efforts performed by the OECD/NEA Expert Group to support this certification process, a burnup computational benchmark exercise has been launched in 2000 [Kalugin et al. 2002] based on the prevailing concept that utilizes U-Gd fuel pins to provide an effective means of introducing burnable absorbers into the MOX assemblies. This is a standard problem for VVER-1000 core physics in which two assemblies are considered, namely a Low Enriched Uranium (LEU) fuel assembly and a MOX fuel assembly, and which will provide a good indication of the current computational methods.

In recent years there has been an increasing demand from nuclear research, industry, safety, and regulation bodies for best estimate predictions of Light Water Reactors (LWRs) performances to be provided with their confidence bounds. In addition to the establishment of LWRs best-estimate calculations for design and safety analysis, understanding uncertainties of evaluated reactor parameters is important for introducing appropriate design margins and deciding where additional efforts should be undertaken to reduce those

uncertainties. In order to address those issues, an in-depth discussion on "Uncertainty Analysis in Modelling" started to take place in 2005 within the OECD/NEA Nuclear Science Committee, which led to the creation of a dedicated Expert Group and to the launching of a Benchmark exercise, the OECD UAM (Uncertainty Analysis in Modelling) LWR Benchmark [K. Ivanov, Avramova, et al. 2013]. The proposed technical approach is to establish a benchmark for uncertainty analysis in best-estimate modelling and coupled multiphysics and multiscale LWR analysis, using as bases a series of well-defined problems with complete sets of input specifications and reference experimental data. The objective is to determine the uncertainty in LWR system calculations at all stages of coupled reactor physics/thermal hydraulics calculation. The UAM benchmark has been conceived to be structured in three different phases, being Phase I the "Neutronics Phase," Phase II the "Core Phase," and Phase III the "System Phase." Additionally, each benchmark phase is subdivided in a number of different Exercises in order to propagate the full chain of uncertainty in the modelling across different scales (multi-scale) and physics phenomena (multi-physics).

The work presented in this thesis was carried out in the "Reaktorphysik und -dynamik" Group at the "Institut für Neutronenphysik und Reaktortechnik" in Karlsruhe Institute of Technology (KIT).

This work is devoted to an assessment of VVER-type fuel assemblies neutronics by means of both Monte-Carlo and deterministic techniques with emphasis on burnup studies and sensitivity and uncertainty (S/U) analysis. More specifically, it provides new solutions (not available in literature) for the OECD VVER-1000 burnup computational benchmark [Kalugin et al. 2002] with the SCALE and SERPENT codes assessing the impact on the solutions of the use of modern nuclear data libraries (NDLs) and different depletion Monte-Carlo algorithms. The application of perturbation and statistical methodologies for evaluating the uncertainties associated to the computation of integral reactor parameters typical of VVER (and generally LWRs) reactors was also a significant part of this work. To this, the test cases of the VVER-1000 and UAM [K. Ivanov, Avramova, et al. 2013] benchmarks has been used.

This work allows, or even suggests, a division of the discussed subjects. For this reason, since the beginning of this thesis, its two main phases, namely the burnup calculation phase and the uncertainty analysis, will be presented separately.

In the present work the VVER-1000 benchmark test cases have been solved by means of the SCALE [ORNL/TM-2005/39 2011] and SERPENT [Leppänen 2008] codes. The SCALE (Standardized Computer Analyses for Licensing Evaluation) code is a software package developed at Oak Ridge National Laboratory (ORNL) that provides a comprehensive, verified and validated tool set for criticality safety, reactor physics, radiation shielding and sensitivity and uncertainty analysis. The SERPENT code is a three-dimensional continuous-

energy Monte Carlo reactor physics burnup calculation code, developed at VTT Technical Research Centre of Finland since 2004. The objective of our study is to provide new solutions with modern Nuclear Data Libraries (NDLs) for the VVER-1000 MOX and LEU computational benchmark. This study allows us to validate the SCALE calculation schemes for VVER-type reactors and to compare deterministic solutions with Monte Carlo reference ones at steady state.

In this work the solutions of some selected test cases at the cell physics and lattice physics levels are presented. The TSUNAMI [Rearden, M. Williams, et al. 2011] and the SAMPLER modules included in the SCALE6.2b3 code package has been used for the neutronics modelling of the selected exercises. Sensitivity and Uncertainty analysis (S/U) based on the generalized perturbation theory has been performed in order to assess the uncertainty of the computation of some selected reactor integral parameters due to the uncertainty in the basic nuclear data. The sampling methodology has also been tested by means of the reference solution provided by the application of the perturbation theory. As a general trend, it has been found that the main sources of uncertainty are the ^{238}U (n,γ) and the ^{239}Pu nubar for the UOX- and the MOX-fuelled test cases, respectively.

1.1 Organization of the thesis

The thesis is arranged in seven chapters, with this introduction as Chapter 1.

Chapter 2 provides an overview about the VVER-type reactors, describing the general aspects and peculiarities of VVER-1000 to contextualize the rest of the work. Several differences in the behaviour of LEU and MOX fuels are highlighted in the last part of the chapter.

Chapter 3 presents a detailed description of the theory which constitutes the basis for all the performed burnup calculations. The focus is on the deterministic and Monte Carlo methodologies and on the differences between them. The codes and the algorithms used to perform the calculations are also described, together with some theoretical problem encountered during the work.

Chapter 4 focuses on the results of the burnup calculations. The results obtained with SCALE are compared with the SERPENT reference ones at steady state. Then the SERPENT results at the following depletion steps are validated with the SCALE ones and with those calculated by the other participants to the OECD VVER-1000 burnup computational benchmark.

Chapter 5 covers the theoretical background for sensitivity and uncertainty analysis, describing the perturbation theory, together with the concept of adjoint flux, and the statistical sampling methodology, introducing also the Wilk's formula and the GRS (Gesellschaft für Anlagen- und Reaktorsicherheit) method.

Chapter 6 presents the results of the sensitivity and uncertainty analysis. In its first part the solutions to the OECD UAM LWR Benchmark are illustrated, while in its second part some additional infomation about the fuel assemblies and the unit cells of the OECD VVER-1000 burnup computational benchmark are given.

In Chapter 7 the work presented herein is summarized and some conclusions are drawn.

Chapter 2

VVER-1000 reactor

2.1 General overview

The Vodo-Vodyanoi Energetichesky Reaktor (VVER), or WWER (Water-Water Energy Reactor), is a type of pressurised water reactor developed in the Soviet Union, and now Russia, by OKB Gidropress, a subsidiary of the state atomic energy corporation ROSATOM. Power output ranges from 300 MWe to 1700 MWe with the latest Russian development of the design. A total of 67 VVER reactors have been constructed since the 1960s by Armenia, Bulgaria, China, Czech Republic, Finland, Hungary, India, Iran, Slovakia, Ukraine and the Russian Federation [*VVER page on Wikipedia* 2014].

The first VVER unit was commissioned in 1964, at Novovoronezh nuclear power plant, in the Voronezh region, Russia, 7 years after the first western PWR reactor (Shippingport, 1957). The first unit was called the V-210, the second the V-365 (the numbers were initially corresponding to electrical output). From that time the Novovoronezh nuclear power plant has been a testing ground for new VVER units. Today, ROSATOM continues the commitment to such an approach – export only the technology which has been thoroughly tested at home [Škoda 2010].

The development of more powerful reactors was encouraged by the successful commissioning and operation of these early units. The VVER-440, built initially at the Novovoronezh site, was the first type of the VVERs which was constructed on a serial basis. The V230 employed six primary coolant loops each with a horizontal steam generator, for better heat transfer. Together they provided a large volume of coolant. Moreover it had isolation valves that allowed the reparation of one or more of the six coolant loops while the plant continues to operate. The principal deficiencies were the absence of emergency core-cooling systems or auxiliary feedwater systems and the design of the Accident Localization System, which served as a reactor confinement: it could handle only one four-inch pipe rupture. If a larger rupture happened, this system vented directly to the atmosphere through

nine large vent valves [*International nuclear society website* 2014].

Model V213, a modified version of VVER-440, was the first VVER reactor designed to comply with the nuclear safety standard adopted by Soviet designers. Emergency core cooling and auxiliary feedwater systems were added by the designers and the Accident Localization Systems was upgraded. The vessel embrittlement represented a great concern in the earlier V230 design: the V213 had a reactor pressure vessel with stainless-steel internal lining to alleviate this concern [ROSATOM 2013].

The VVER-1000 was a milestone both in terms of generating capacity and for the innovative safety systems it incorporated. The VVER- 1000 is the most common VVER design worldwide, 31 units are in operation, and have amassed about 500 reactor-years of operation.

In the early 1980s the design of the VVER-1000 V-320 reactors was completed. Eight sites in Russia, Ukraine, Bulgaria (Kozloduy 5-6) and Czech Replubic (Temelin 1-2) were chosen to host this type of plants. VVER-1000/V320 is a heterogeneous thermal neutrons water-water energy reactor with an electrical output of about 1000 MWe and an efficiency factor of about 34%. Demineralized water with diluted boric acid is used as coolant and as moderator in the primary circuit, with a changing concentration of boric acid during operation. The water is always in a liquid state and this causes the adoption of an indirect cycle with steam generators. To allow the water not to evaporate the primary system pressure must always be higher than the equilibrium vapor pressure at the water highest allowable temperature. For this reason the plant is equipped with a pressurizer, whose main task is to keep pressure within the bounds that were set for the correct functioning of the system.

The V-320 used four coolant loops and horizontal steam generators and adopted a steel-lined, pre-stressed, large-volume concrete containment structure, similar in function to Western nuclear plants. The fuel assemblies have been redesigned and allowed better flow of coolant. Plant worker radiation levels were lower than in many western plants, apparently due to selection of materials, high-capacity system for purifying primary coolant, and water-chemistry control. [*Gidropress website* 2014]

The heat generated in the reactor core is transferred through four cooling loops, which surround the reactor. In each cooling loop, water heated to 321 °C is piped to the steam generator. The steam generator is similar in scale to that of a PWR, but its configuration is different: the cylinder in the VVER is horizontal, whereas in a PWR it is vertical. In the steam generator the radioactive primary circuit water flows through 10978 heating pipes, each of 16 mm in diameter, resulting in the boiling of secondary side water. The cooled water returns to the reactor in the primary circuit at a temperature of 288 °C. Water in the primary side is circulated by the main circulating pump. Each coolant loop can be isolated using a valve. The pressurizer keeps the pressure at the constant value of 15.7 MPa.

Table 2.1: General VVER-1000 parameters

Parameter	Value
Total power [MW_t]	3000
Capacity factor	0.78
Inter refueling period [months]	12
Time of fuel presence in core [years]	4
Service life [years]	30

The primary water, which circulates in small tubes at a temperature of 321 °C, causes the feedwater that enters the steam generator at 6.27 MPa and 220 °C to boil. The moisture content of the generated steam must be lowered, otherwise the turbine blades would be damaged. This is obtained by moisture separator shutters put into the way of steam. Thanks to the use of these plates, the moisture content of the outgoing steam will only be 0.25%. The steam leaves the steam generator at a flow rate of 1470 t/h and heads towards the turbine. Further data about VVER-1000 reactor may be found in [Table 2.1].

In the following paragraphs the main features of a VVER-1000 will be described and, in particular, the V-320 "Kozloduy 6" Nuclear Power Plant (NPP) in Bulgaria will be used as a reference.

2.2 Reactor core and fuel assembly

VVER fuel is held in a hexagonal grid. Light water used as both moderator and coolant is passed at very high pressure trough the core, in a reactor pressure vessel around 14 m high and 4 m in diameter. The reactor core [Figure 2.1] includes in total 211 assemblies: 163 uncased fuel assemblies, identical in design, but different in fuel enrichment, and 48 reflector assemblies. Axially, the core is divided into 10 layers with a height of 35.5 cm, adding up to a total active core height of 355 cm. Both upper and lower axial reflectors have a thickness of 23.6 cm. Radially, the core is divided into hexagonal cells with a pitch of 23.6 cm, each corresponding to one fuel assembly, plus a radial reflector of the same size.

The VVER-1000 fuel assembly [Figure 2.2] is a hexagon and contains 312 fuel rods. The fuel enrichment can be 3.7 or 4.4$wt.$% [NationalRegulatoryAgency 2011]. A frame consisting of 18 guide tubes and 1 central tube bears the load to fuel assembly. The tubes are also useful to support the cellular grid which guarantees the correct spacement between the fuel rods. The fuel assembly head and lower grid hold the the guide tubes. The central tubes house the control rods and neutron and temperature control sensors in them. To improve physical characteristics and safety some fuel rods are

filled with pellets with a content of gadolinium oxide Gd_2O_3 of 4.0$wt.\%$.

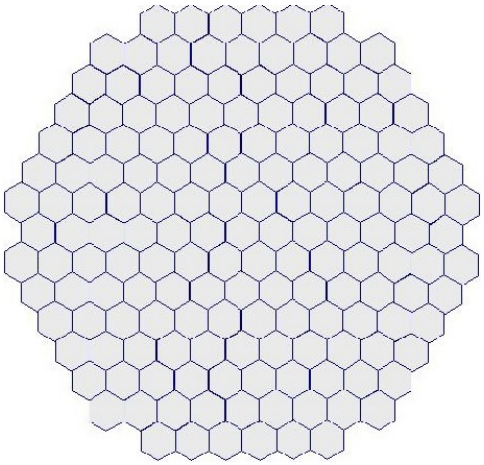

Figure 2.1: Core configuration

Fuel assembly design [Figure 2.3] consists of the following components: top nozzle, bundles of fuel rods, bottom nozzle. The top nozzle provides necessary force of fuel assembly compression in the core. The bottom nozzle provides conjugation of the lower part with the support of the reactor core barrel and presents a guiding device for coolant supply into bundles of fuel rods. Bundles of fuel rods, both standard fuel rods and gadolinium fuel rods, consist of a skeleton that houses the 312 fuel rods. The skeleton is composed of guiding channels and spacing grids. It provides the assemblies and fuel rods strength and geometry and the fuel rods spacing throughout the entire fuel assembly service life. Besides fuel rods, the fuel assembly has a number of structural elements: cap, tailpiece, spacing grids and in some cases – a shroud tube. A cap is designed for gripping during load – unloading operations, and a tailpiece ensures the fuel assembly placement into the reactor and provides channel for coolant for fuel rods. The fuel of the VVER reactor is uranium dioxide (UO_2), which is compacted to cylindrical pellets of about 9 mm height and 7.7 mm diameter. In the centerline of the pellets there is an inner cylindrical hole of 1.4 mm to allow the gaseous fission products escape, reducing the pressure, but also to reduce the fuel temperature. The uranium pellets are inserted in a 3.5 m long and 9.1 mm diameter tube made of zirconium alloy, which is sealed hermetically. The cladding prevents the fission products and other radioactive materials from getting into the cooling water. There is a thick gap (0.08 mm) between the pellets and cladding in order that sufficient space is available for the pellets' heat expansion at the high operational temperatures. Further parameters are shown in [Table 2.2].

The VVER-1000/V320 reactor is equipped with 61 control assemblies, grouped into ten groups. They are full-length control rods except group number 10, which consists of part-length control rods. The part-length control rods have neutron absorber only in its lower half and they are used to damp the xenon oscillations. The full-length control rods contain the strong neutron absorber over a length that spans most of the active core region. In addition to the radial arrangement, the position of control rod insertion in units of cm is given from the bottom of the lower reflector. The total control assembly length, which coincides with the absorber length, is 371 cm. The position of the lower control assembly absorber edge from the bottom

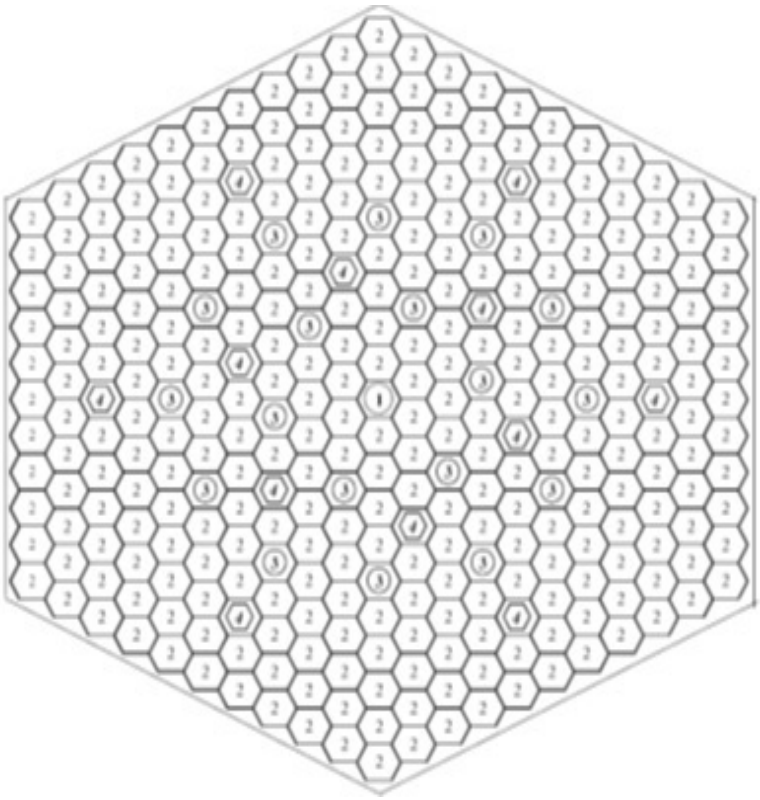

Figure 2.2: Fuel assembly configuration. Cell types: 1- Central tube, 2- Fuel cell, 3- Guide tube, 4- Fuel cell with gadolinium

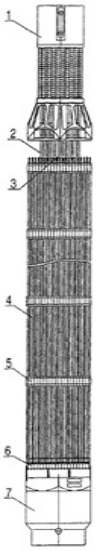

Figure 2.3: General view of fuel assembly 1 - Head, 2 - Guide channel, 3 - Central tube, 4 - Fuel element, 5 - Spacer grid, 6 - Lower grid, 7 - Nozzle

Table 2.2: General core parameters

Parameter	Value
Max fuel enrichment [%]	4.4
Uranium dioxide load [t]	80
Average specific power $[kW/l]$	110
Power density $[W/cm^3]$	107
Max linear heat flow $[W/cm]$	448
Minimal DNBR	1.73

of the lower reflector is 23.6 cm for a completely inserted control assembly, and 378.6 cm for a completely withdrawn control assembly. The definition "completely withdrawn" means withdrawn from the active core, i.e. out of the core. The control rods are inserted into the reactor from the top. [Nikolay 2013]

The control rod cluster assembly is made of 18 absorbing elements, the grip head and springs of an individual suspender. The absorbing element is a tube with outer diameter $8.2 \cdot 10^{-3}$ m and wall thickness $0.5 \cdot 10^{-3}$ m filled with absorbing material and sealed by means of welding. Boron carbide (B_4C) and dysprosium titanate ($Dy_2O_3TiO_2$) are used as absorbing material. Dysprosium titanate in the absorbing element lower part enables to extend rod control cluster assembly service life under maintenance of sufficient worth of emergency protection.

2.3 Reactor vessel and internals

The VVER-1000 reactor vessel [Figure 2.4] is a vertical cylinder used for generation of heat within the NPP nuclear steam supply system. A chemically purified water with boric acid serves as coolant and moderator. Two systems based on different principles allow the regulation of reactor power and the suppression of the fission chain reaction:

- Introducing solid absorbers - control rods system (control & protection system – CPS);
- Injection of liquid absorber - boron regulating system.

These two systems have been designed for different purposes: the former is used for reactor shutdown in normal and emergency operation conditions and to change the reactivity during the maneuvering regimes; the latter is used only to compensate the slow changes in reactivity. As a consequence, the concentration of boron in the water continuously changes during the life cycle. The coolant is heated while it flows around fuel assemblies due to the energy of nuclear fission in the fuel. The coolant enters the vessel through four input

Table 2.3: Reactor vessel design data

Parameter	Value
Overall height [m]	10.9
Total volume [m^3]	110
Inlet nozzle ID [m]	850
Outlet nozzle ID [m]	850
Coolant flow [kg/s]	17611
Outer diameter [m]	4.535
Inner diameter [m]	4.136
Height of elliptical bottom [m]	0.967
Elliptical bottom wall thickness [m]	0.237

nozzles, passes a ring gap between the reactor vessel wall and the core barrel, and, through a perforated bottom plate, reaches the fuel assemblies installed in the reactor core. After the heating across the fuel assemblies, the water exits the reactor vessel through outlet nozzles to the so called "hot leg". The reactor pressure vessel has a total height of 13.75 m and an outer diameter of 3.84 m, its thickness at the height of the reactor core is 14 cm and there is an inner 9 mm-thick stainless steel plating as corrosion prevention. There are four outlet and four inlet pipe connections located at two different heights on the vessel. [Table 2.3] highlights some geometrical data about the vessel. The VVER-1000 reactor vessel design is based on the following principles:

- proven manufacturing process and structural materials;
- complete in-shop manufacture of the vessel, tests included;
- possibility of vessel transportation by rail and by sea;
- possibility of periodic in-service inspection of the vessel.

To build the reactor vessel several forged shells are welded to each other and to an elliptic bottom head and a flange. The flange is sealed with solid ring sealing gaskets and is tightened with 54 M170 studs. [InternationalAtomicEnergyAgency 2011]

The vessel has two nozzle shells. Each of them has four nozzles with an internal diameter of 850 mm, that are connected to the main coolant pipeline of reactor coolant system. The inlet and outlet chambers are kept separated by means of the ring welded to the vessel internal surface clad with austenitic steel. The ring is also used to keep the core barrel from radial displacement and as an housing for the surveillance specimens.

The reactor vessel is made of heat-resistant steel, grade $15X2HM\Phi A$. The principles used to choose the reactor vessel steel and the welding materials

were the analysis of mechanical properties, the stability during irradiation, the lack of susceptibility to brittle fracture and the durability.

The vertical pressurized vessel houses core barrel with the baffle, protective tube unit, fuel assemblies, control rod cluster assembly, in-core instrumentation detectors. The vessel shoulder supports a welded cylindrical shell with a supporting bottom and a flange, called the core barrel. The core barrel has a perforated elliptical bottom to space and support the fuel assemblies. The same purpose is achieved by means of the spacer grids and 163 support tubes.

Inside the core barrel, at the core level, there is the core baffle. It protects the fuel assemblies and separates them from the core barrel. The distance between the core baffle and the fuel assembly periphery is a structural gap. Several big rings are mechanically attached to form the core baffle. The load of the core baffle is supported by the core barrel bottom. The cooling of the core baffle metal is made possible thanks to several longitudinal channels that allow the passage of the water.

A corrosion-resistant steel of austenitic grade has been chosen as structural material for all the internals.

The protective tube unit has two tasks: it houses the control rods and the in-core instrumentation detectors and it makes a rigid support structure that spaces the fuel assemblies and keeps them from lifting. The protective tube unit is installed on the top of the barrel. An elastic element is used to connect the protective tube unit and the core barrel flange. The elastic element is installed between the protective tube unit shoulder and the upper unit top head.

The upper unit structure includes control rod drives and the elliptic top head with a flange and nozzles. A pitch electromagnet drive is used as control rod drive that provides motion of control rods with the velocity of 2 cm/s.

2.4 Steam generator

The steam generator used in VVER reactors [Figure 2.5] is named PGV-1000MK. It is an horizontal single-vessel recuperative heat-exchanger with submerged horizontal heat exchanging surface. The steam is dried at the top of the housing by gravitational separation. Forged shells, stamped elliptic bottoms and forged nozzles connected by welding form the external body of the steam generator. The steam generator is designed to house the internals and to provide an easy access to the secondary side. In this way it is possible to examine and possibly to repair the internals.

The heat exchanging surface comprises 10978 U-tubes with a diameter of 16 mm. The tubes are positioned horizontally in corridor arrangement. The steam generator nominal characteristics are shown in [Table 2.4]. The steam generator can produce 1470 t/h of steam with a steam quality not below

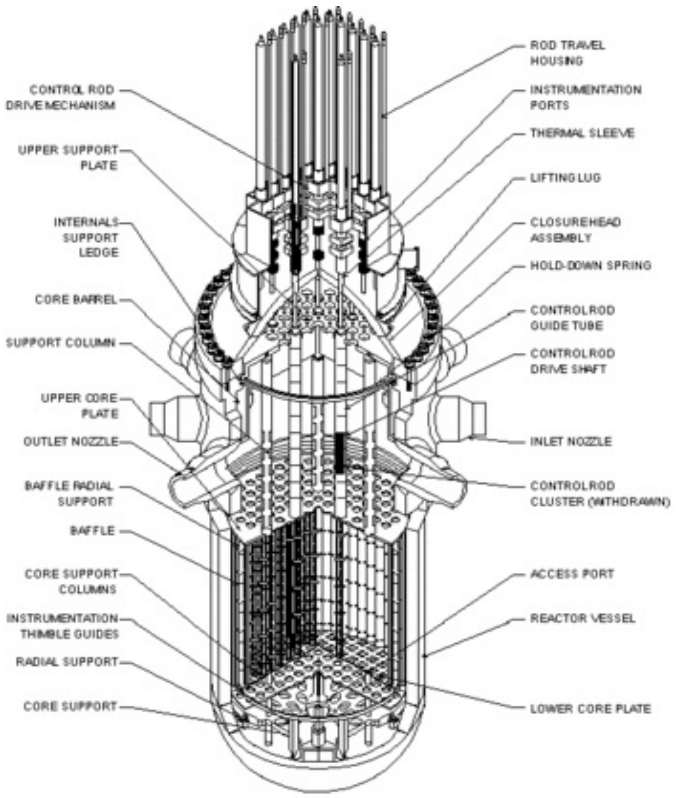

Figure 2.4: VVER-1000 reactor pressure vessel

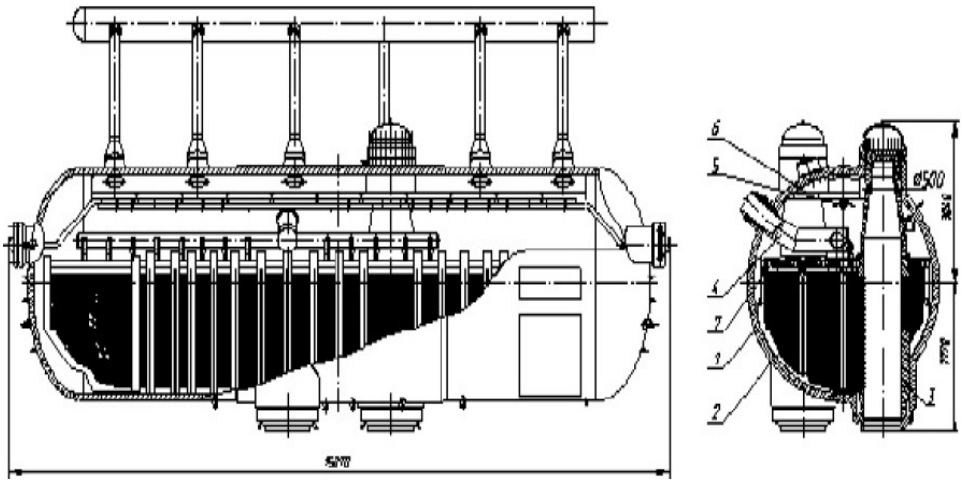

Figure 2.5: General view of steam generator. 1- vessel, 2- heat exchanging surface, 3- primary side collectors, 4- main feedwater distribution devices, 5- emergency feedwater distribution devices, 6- steam distribution perforated plate, 7-submerged perforated plate

Table 2.4: Steam generator nominal characteristics

Parameter	Value
Height of a head [m]	4
Lenght of cylindrical part [m]	11.34
Primary side volume [m^3]	20.5
Tube OD [mm]	16
Tube ID [mm]	13
Average lenght of tubes [m]	11.1
Steam flow [kg/s]	437
Steam temperature [$°C$]	278.5
Steam pressure [MPa]	6.28 ± 0.2
Feedwater temperature [$°C$]	220 ± 5

99.8%.

The steam generator's tubes are connected to primary-side collectors. The tubes are made of austenitic steel. Their edges are hydraulically expanded over the entire collector wall thickness and welded on the inside surface of the collectors by argon-arc welding. The coolant is distributed in the heat exchanging tubes by the primary-side collectors. The collectors are designed also for coolant collection and removal. A two-layer internal cladding is provided to enhance tubes corrosion resistance. The steam is distributed by means of a plate that is collocated in the top section of the steam generator. The equalization of steam load is performed by a perforated plate, arranged under the water level.

Water with high content of salt and other impurities can be found in the salt cell, that is a zone of the steam generator usually located near one of the bottoms. The impurities accumulation is due to the arrangement of supply of feedwater and blowdown of steam generator.

One of the main advantage of PGV-1000MK steam generator is the large water inventory inside the vessel. This fact is the cause of the good dynamic characteristics of the entire reactor in case of loss of feedwater.

A characteristic and distinguishing feature from the steam generator in VVER reactors is that inconel 600 and 690 alloys or incalloy 800 with high nickel content – 75, 60, and 32%, respectively – are used for the tubes in the heat-exchange bank. The tubes of the new steam generators are manufactured from heat-treated inconel 690 alloy. The tube sheet is made of 08Kh18N10T corrosion-resistant steel with 10% nickel content.

The horizontal design is considered to be less susceptible to degradation than the vertical U-tube one. More specifically, the orientation of a tube has effects on boiling and on occurrence of boiling crisis causing differences on their behaviour to stress conditions. On the basis of operating experience

gained over many years, horizontal steam generators have advantages over vertical steam generators. The main ones are:

- moderate steam load (steam outflow rate from the evaporation surface 0.2–0.3 m/s);
- simple gravity-based separation scheme;
- moderate velocity of the medium in the second loop (up to 0.5 m/s), preventing any danger of vibrations of the heat-exchange tubes and damage from foreign objects;
- validated serviceability of the 08Kh18N10T austenitic steel tubes (the maximum operational age is 38 years for PGV-440 and 423 years for PGV-1000);
- vertical arrangement of the first-loop collectors, preventing accumulation of sludge deposits on their surfaces, thereby decreasing the danger of corrosion damage to the heat-exchange tubes in the region where the tubes are built into the tube sheet;
- larger store of water in the second loop, enabling cool-down of the reactor through the steam generator in the case where normal and emergency water feeding has stopped;
- the principle of stepped evaporation, making it possible to maintain an admissible concentration of dissolved impurities in the critical zones and increasing the reliability from the standpoint of corrosion effects;
- horizontal arrangement of the heat-exchange surface, enabling reliable natural circulation of the first-loop coolant even with a massive water level below the top rows of the heat-exchange tubes;
- convenient access to the tube sheet for servicing and checking from the first and second loop sides; there are no heat-exchange tubes at the bottom of the housing, so that sludge is more easily removed through the purge system;
- presence of equipment for disconnecting the collectors from the main circulation pipelines, making it possible to decrease the time required to perform scheduled– preventive maintenance work and to increase the installed capacity utilization factor by performing work simultaneously on several steam generators and refueling the reactor.

One of the main problems of horizontal steam generators is corrosion damage to the heat-exchange tubes, resulting in a large number of plugs due to defects being formed. Vertical steam generators have an irremovable conceptual drawback – the presence of a horizontal tube above which sludge collects, and

corrosion of the tubes in this zone can be prevented only if there is no sludge. It is extremely difficult to accomplish this: regular and careful mechanical or chemical cleaning is needed. As already mentioned, in horizontal collectors sludge settles at the bottom of the housing outside the tube bank and can be easily removed. Nonetheless, the heat-exchange tubes must be washed also in horizontal steam generators. [Bonavigo and De Salve 2011, Trunov et al. 2008]

2.5 Neutronic differences between LEU and MOX fuels

The purpose of this section is to quantify the differences in the neutronic behaviour between mixed oxide (MOX) and low–enriched uranium (LEU) fuels. For this reason the nuclear properties, the flux spectrum, the power distribution, the kinetics parameter and the reactivity coefficients of LEU and MOX fuel assemblies are compared and their effects on the adsorber effectiveness and on the lifetime of the pressure vessel are briefly explained. Further informations on this topic can be found in [Gehin and Ellis 2004].

2.5.1 Nuclear properties

The differences between the two types of assemblies arise from the different fissile material, which is ^{235}U in LEU while are ^{239}Pu and, to a lesser extent, ^{241}Pu in MOX. The fuel used in the MOX assemblies is characterized by a reduced enrichment in uranium, which is depleted to the 0.2% and by a content of weapons-grade and other reactor-grade plutonium. Tables 2.5, 2.6 and 2.7 shows the three plutonium vectors used in the burnup phase of this thesis work. Table 2.8 shows instead the nuclear properties of ^{235}U and ^{239}Pu.

The higher values of thermal fission and absorption cross-sections of ^{239}Pu have two important effects:

- the thermal flux in MOX assemblies is lower than in LEU assemblies;
- the pins located at the MOX/UO_2 interfaces present a severe power peaking.

The first effect deserves a better description. The thermal neutron flux in the MOX assemblies is substantially lower than in LEU ones and also the fast flux is slightly smaller. The fast-to-thermal ratio in the MOX is almost twice that of the UO_2. [Table 2.9]

These facts lead to some particular phenomena. One of the most important is the reduction in reactivity worth of neutron-adsorbing materials. The effectiveness of boric acid (H_3BO_3), that is used to offset the burnup of the fuel and of the burnable adsorber, is reduced since it is a thermal adsorber.

Table 2.5: Plutonium isotopic compositions in the 4.2% pins

Isotope	^{239}Pu	^{240}Pu	^{241}Pu
Content, wt%	93.00	5.99	1.01

Table 2.6: Plutonium isotopic compositions in the 3.0% pins

Isotope	^{239}Pu	^{240}Pu	^{241}Pu
Content, wt%	93.10	5.90	1.00

Table 2.7: Plutonium isotopic compositions in the the 2.0% pins

Isotope	^{239}Pu	^{240}Pu	^{241}Pu
Content, wt%	92.90	6.10	1.00

Table 2.8: Nuclear properties of ^{239}Pu and ^{235}U

Parameter	^{235}U	^{239}Pu
Thermal fission cross-section [barns]	577	741
Thermal absorption cross-section [barns]	678	1015
Average number of neutrons per fission	2.43	2.87
Delayed neutron fraction	0.0065	0.0020
Energy per fission [MeV]	192.9	198.5

Table 2.9: Thermal and fast neutron flux in MOX and LEU assemblies

	UO_2 assembly	MOX assembly
Fast flux (> 0.625 eV)	$8.31 \cdot 10^{13}$	$8.08 \cdot 10^{13}$
Thermal flux (< 0.625 eV)	$9.95 \cdot 10^{12}$	$4.67 \cdot 10^{12}$
Fast/thermal flux ratio	8.35	17.29

To cope with this problem the boron concentration or, as an alternative, the enrichment of the boron in the ^{10}B isotope have to be increased. Each of these ways has a drawback: an increase of the concentration can lead to difficulties in the adjustment of the boron levels and can increase the water and chemical volume which have to be processed; on the other hand the enrichment of the boron, that can solve these operational issues, is very expensive and can require plant modifications to recover the boron.

With regard to the control rods, their worth is fundamental in the evaluation of the shutdown margins, as well as the reactivity insertion rates in response to a reactor scram. The MOX loading causes the shutdown margin and the scram efficiency to decrease, therefore the boron enrichment has to be raised.

The second of the effects listed above, i.e. the power peaking, that is due mostly to the larger fission cross-section of plutonium, can be handled with a careful design of the assemblies. Usually the pins in MOX assemblies are arranged in concentric rings with different plutonium loadings and this trick minimizes the peaking effect. In the MOX assembly of the OECD benchmark there are three rings and, starting from the innermost, they have a fissile plutonium concentration of $4.2wt.\%$, $3.0wt.\%$ and $2.0wt.\%$. Also the use of burnable adsorber can be useful to control this problem.

2.5.2 Assembly reactivity

Figure 2.6 shows a comparison of the infinite multiplication factor of the two types of assembly, without burnable adsorbers. The MOX assembly reactivity decreases more slowly than that of uranium fuel. Therefore, the matching of the MOX and uranium core designs must consider this difference to obtain fuel cycle lengths that are similar. In general this requires that the lifetime-averaged reactivities must match, but this is not necessary when a burnable absorber is used or the MOX and UO_2 assemblies have different residence times in the core.

2.5.3 Kinetics parameters and reactivity coefficients

Kinetic parameters The kinetics parameters affect the time response of the reactor to reactivity changes. Two of the most important are:

- β, the effective delayed neutron fraction;
- Λ, the prompt neutron lifetime.

If β has a smaller value, more neutrons appear as prompt neutron. Therefore the kinetic response of the reactor is quicker. ^{239}Pu has a delayed neutron fraction significantly smaller than ^{235}U and so MOX cores respond more quickly than the UO_2 cores. The results of studies as [A. Pavlovitchev et al. 2001,A. e. a. Pavlovitchev 2004] show a $10 - 15\%$ reduction of β, depending

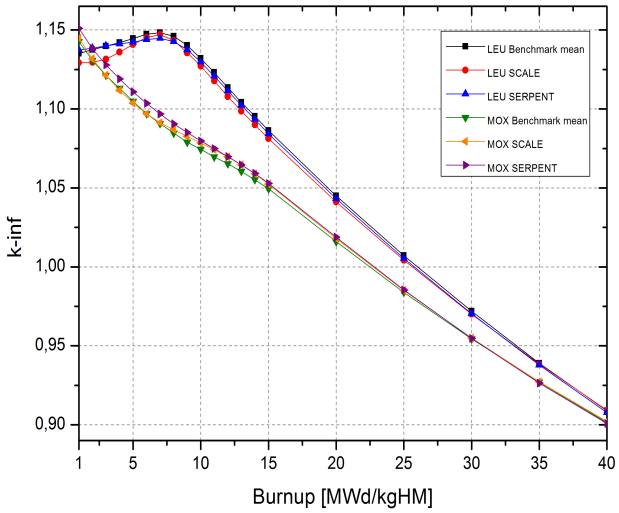

Figure 2.6: Comparison of infinite multiplication factor

of the MOX core fraction. The lowest values of β occur at the end of cicle, because the fraction of fissions from plutonium is highest at that time.

Λ is related to neutron generation time. A bigger prompt neutron lifetime means that the changes in neutron multiplication factor need more time to effect the prompt neutron population. MOX fuels have a shorter Λ, since the slower neutrons are preferentially absorbed. This is caused by the larger thermal absorption cross-section of ^{239}Pu. Like the value of the effective delayed neutron fraction, also Λ exhibits a 15% reduction. [A. e. a. Pavlovitchev 2000, Alioshin 2001]

These values of β and Λ must be considered in the safety analysis and in the evaluation of the core protection system.

Reactivity coefficients The reactivity coefficients relates the change in thermal-hydraulics conditions to the core neutronics through changes in reactivity. As indicated by some previous works, as [A. Pavlovitchev et al. 2001], MOX fuel results in a slightly larger Doppler coefficient and a significantly larger moderator temperature coefficient. This condition can be a concern in accident scenarios characterized by an overcooling of the core. In fact, the overcooling in MOX fuel will result in a larger increase in reactivity than that of UO_2 fuel.

2.5.4 Pressure vessel fluence

As a consequence of the harder spectrum and of the increase in fast flux, there is a potential of a larger fast fluence of the pressure vessel. A bigger fluence can cause a larger embrittlement. The results of a study on this topic [Zaritsky 2004] are given in figures 2.7a and 2.7b, while tables 2.10 and 2.11 shows a summary of the results and the fluxes in the surveillance specimens.

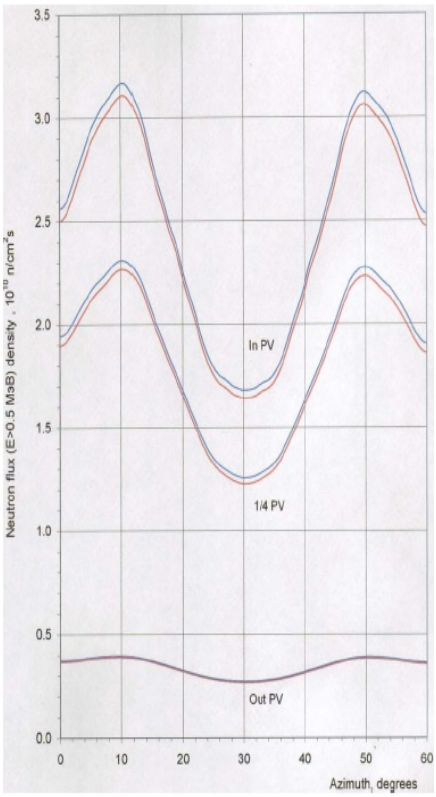

(a) *Azimuthal variation of the fast neutron flux near core midplane*

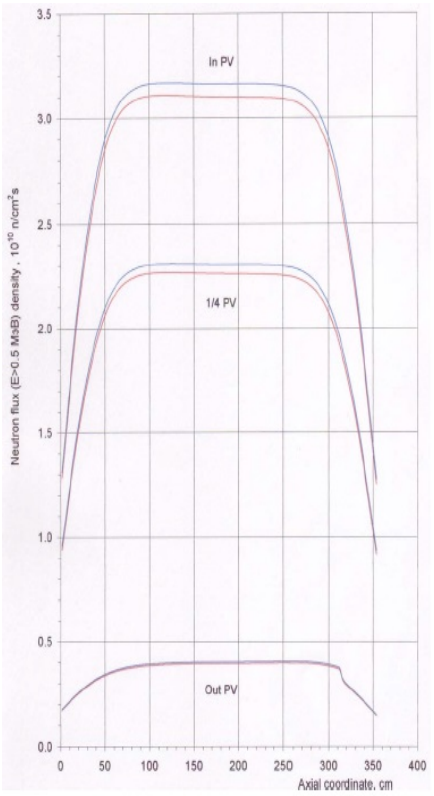

(b) *Axial variation of the fast neutron flux at 10.3 degree*

Figure 2.7: Results of pressure vessel fluence calculations (red line is UO_2; blue line is MOX).
In PV: inner surface; 1/4 PV: one fourth of thickness; Out PV: outer surface.

The neutron flux for the MOX core is insignificantly larger than with the UO_2 core. Even the specimens revealed almost the same neutron fluxes for both types of fuel. This minimal changes in neutron flux on the pressure vessel are the results of careful design of the core loading patterns. The outer ring in the MOX core is constituted by uranium assemblies and by the highest burned assemblies. This ring is the closest to the pressure vessel and has the maximum impact on it, but the assemblies occupying this ring are the same

Table 2.10: Results of fast neutron flux at the pressure vessel ($10^9 n/cm^2 s$)

	Inner surface		1/4 of Thickness		Outer surface	
	UO_2	MOX	UO_2	MOX	UO_2	MOX
Maximum	31.1	31.7	22.7	23.1	3.90	3.98
Minimum	16.4	16.8	12.3	12.6	2.67	2.73

Table 2.11: Results of fast neutron flux at the surveillance assembly($10^9 n/cm^2 s$)

	Lower level		Upper level	
	UO_2	MOX	UO_2	MOX
Maximum	287	285	104	104
Minimum	164	163	64.6	64.2

for both types of core. The tables and the figure above demonstrate that a careful design is sufficient to avoid concerns about the high fluence on the pressure vessel.

Chapter 3

Burnup theory

This chapter presents a brief theoretical overview of the subjects studied to solve the OECD benchmark with the SCALE6.1 and SERPENT code.

3.1 Neutron transport equation

Neutron transport has roots in the Boltzmann equation, which was used in the 1800s to study the kinetic theory of gas. Its big development was caused by the studies about chain-reaction nuclear reactors in the 1940s.

The neutron transport equation is an equation of conservation of neutrons. Each term represents a gain or a loss of neutrons, and the balance, in essence, claims that neutrons gained equals neutrons lost. It is formulated as follows:

$$\begin{aligned}\frac{1}{v}\frac{\partial\phi}{\partial t}\left(\overrightarrow{r},E,\overrightarrow{\Omega},t\right)+\overrightarrow{\Omega}\cdot\nabla\phi\left(\overrightarrow{r},E,\overrightarrow{\Omega},t\right)+\Sigma_t\left(\overrightarrow{r},E\right)\phi\left(\overrightarrow{r},E,\overrightarrow{\Omega},t\right)=\\ =\int_0^\infty\int_{-1}^1\Sigma_s\left(\overrightarrow{r},E'\rightarrow E,\mu_0\right)\phi\left(\overrightarrow{r},E',\overrightarrow{\Omega}',t\right)d\mu_0dE'\\ +\frac{1}{4\pi}\int_0^\infty\int_0^{4\pi}\nu\Sigma_f(\overrightarrow{r},E')\phi\left(\overrightarrow{r},E',\overrightarrow{\Omega}',t\right)dE'd\overrightarrow{\Omega}'\\ +S_{ex}\left(\overrightarrow{r},E,\overrightarrow{\Omega}\right)\equiv q\left(\overrightarrow{r},E,\overrightarrow{\Omega}\right),\end{aligned}\tag{3.1}$$

where

- $\phi(\overrightarrow{r},E,\overrightarrow{\Omega},t)\equiv vN\left(\overrightarrow{r},E,\overrightarrow{\Omega},t\right)$, is the angular flux distribution, with:
  - $N\left(\overrightarrow{r},E,\overrightarrow{\Omega},t\right)$, number of neutrons per unit volume around $\overrightarrow{r}$, per unit energy around E and per unit solid angle around $\overrightarrow{\Omega}$;

  - v, neutron speed;

- Σ_t, Σ_s and Σ_f are, respectively, the total, scattering and fission macroscopic cross-sections;
- ν is the average number of neutrons produced per fission;
- $S_{ex}\left(\overrightarrow{r}, E, \overrightarrow{\Omega}\right)$ is an external source;
- $q\left(\overrightarrow{r}, E, \overrightarrow{\Omega}\right)$ is the emission density;
- $\mu_0 = \Omega \cdot \Omega'$.

The first term of the left hand side represents the change rate of neutrons in the system during the time. The second terms describes the entry or the exit of neutrons from the volume of space of interest. The third term enumerates the collisions in that phase space. The first term on the right hand side accounts for the in-scattering, i.e. neutrons that have a scattering interaction in a different phase space and so enters in the considered space. The second term is the production of neutrons in this phase space due to fission and the third is self explanatory. The spatial, angular, energy, and time variables must be discretized to make possible the numerical solution.

- Spatial variables are typically discretized with a mesh and then the finite difference method can be use to solve the balance equation;
- angular variables can be discretized by discrete ordinates and weighting quadrature sets or with the spherical harmonics, giving rise, in the first case, to the S_n methods, and in the second to the P_n methods;
- energy variables are discretized by the multi-group method;
- the time is usually subdivided into discrete time steps.

These methodologies are just outlined here; a more complete description can be found in textbooks and articles, for example [Stacey 2001] or [Lewis and Miller 1984].

3.2 Monte Carlo method

A different way to solve the transport equation without resorting to deterministic methods is represented by the Monte Carlo method. According to Emilio Segrè, the Monte Carlo method was invented by Enrico Fermi during the thirties, when he was studying the neutron diffusion in Rome. He used this method with small mechanical adding machine to solve many problems, but he never published anything about this.[Metropolis 1987]

The spark that led to Monte Carlo method was triggered by Stanislaw Ulam and John von Neumann, Professor of Mathematics at the Institute for Advanced Study and consultant to Los Alamos National Laboratories. Ulam's background in mathematics and the development of ENIAC (Electronic Numerical Integrator and Computer) allowed for the creation and for the tests of the code.

Nowadays the Monte Carlo method is used in criticality safety analyses, validation of deterministic codes, dosimetry calculations and medical applications. The common need is the will to reach the maximum accuracy in modelling the geometry and in the interaction physics. Burnup calculation is a relatively new application for this method. This type of calculation is very computing-intensive, since the time-consuming transport calculation has to be repeated for a large number of depletion steps.

In Monte Carlo calculations the neutrons paths are followed one at time from the birth to the neutron death by capture or leakage.The randomization of the time, of the type and of the results of neutron interaction is based on distributions, which are different for each nuclide and depend on the neutron energy. [Leppänen 2007]

The attractiveness of Monte Carlo comes from the simplicity and the potential to produce very accurate results, but also from the possibility of using all the the best available knowledge on neutron interactions with matter, without any need of approximations. This knowledge is provided by several organization, which create and update nuclear data libraries. Examples of these organizations and libraries are:

- OECD NEA with JEFF (Joint Evaluated Fission and Fusion) libraries;
- U.S. Cross-Section Evaluation Working Group with the ENDF-B (Evaluated Nuclear Data Files) libraries;
- Japan Atomic Energy Agency with JENDL (Japanese Evaluated Nuclear Data Library).

In addition to nuclear data, problem geometry, temperatures, densities and material compositions are needed for transport calculations. Moreover, since one simulated neutron corresponds to several real neutrons, a normalization condition, such as total power, is also required to discover the correlation among these two quantities.

More details about Monte Carlo can be found in [Lux and Koblinger 1991], [Spanier and Gelbard 2008] or, to a lesser extent, [Reuss 2008].

3.2.1 Statistics

The statistical uncertainties are always present in Monte Carlo calculations and, in accordance with the central limit theorem, they are proportional to $1/\sqrt{n}$, where n is the numbers of the events that contribute to the estimate.

This number depends linearly on the number of neutron histories. Instead, the computational cost of the simulation is directly proportional to the number of histories and so, if a halving of statistical uncertainty is required, the running time will quadruply. Running times can vary widely for different calculations, also in similar geometries and using the same code. [Isotalo 2013]

A little number of neutron contributes to the averages over small volumes and energy ranges, if compared with larger ones. In the former cases it is mandatory to simulate more neutrons to reach the same level of accuracy of the latter cases. Burnup calculations often require to estimate flux or cross-sections for small material regions and so a relatively large statistical variation in the estimated reaction rates occurs. However, since the statistical errors tend to cancel out when the entire geometry is considered, the accuracy of the global results is preserved.

3.3 Comparison between deterministic and Monte Carlo codes

Deterministic neutron transport methods and Monte Carlo are two alternatives to solve burnup calculations. In this paragraph strenghts and weakness of these two families of methods are listed.

All deterministic methods are faster than Monte Carlo and have not the statistical uncertainty associated with Monte Carlo method. Since the efficency of Monte Carlo is low in calculating local quantities and multidimensional distributions, deterministic methods have higher performances and can be several order of magnitude faster in those cases.

On the other hand, the Monte Carlo method can use all the available knowledge to handle the transport calculation and neutron interaction physics, without any need of approximations. Moreover the Monte Carlo methods can model any type of complex geometry consisting of discrete material regions. These features make the method more accurate and problem independent. The latter is a great advantage of Monte Carlo methods, as they can be used for many different problems, while different deterministic methods are needed for problems with different neutron energy, e.g. fast and thermal systems, or with different geometry, e.g. hexagonal and square assemblies. As an alternative the same code needs to be validated separately. The calculation is slowed down by the complexity and the size of geometry, but much lesser than with deterministic methods.

3.4 Codes used for burnup calculations

3.4.1 SCALE

SCALE* (Standardized Computer Analysis for Licensing Evaluations) is a comprehensive modelling and simulation suite for nuclear safety analysis and design developed and maintained by Oak Ridge National Laboratory under contract with the U.S. Nuclear Regulatory Commission, U.S. Department of Energy, and the National Nuclear Security Administration to perform reactor physics, criticality safety, radiation shielding, and spent fuel characterization for nuclear facilities and transportation/storage package designs [*SCALE website* 2014].

The SCALE system was developed for the Nuclear Regulatory Commission to satisfy a need for a standardized method of analysis for the evaluation of nuclear fuel facility and package designs. In its present form, the system has the capability to perform criticality, shielding, radiation source term, spent fuel depletion/decay, reactor physics, and sensitivity/uncertainty analyses using well-established functional modules tailored to the SCALE system.

The SCALE system consists of analytical sequences which are automated to perform the necessary data processing and manipulation of well-established computer codes required by the sequence. Thus the user is able to select an analytical sequence characterized by the type of analysis (criticality, shielding, or heat transfer) to be performed and the geometric complexity of the system being analyzed. The user then prepares a single set of input data for the control module corresponding to this analytical sequence. The control module input is in terms of easily visualized engineering parameters specified in a simplified, free-form format. The control modules use this information to derive additional parameters and prepare the input for each of the functional modules in the analytical sequence. Provisions have also been made to allow the user to execute the functional modules on a stand-alone basis [*NEA website* 2014].

Among these sequences TRITON module has been used for the solution of the OECD benchmark.

TRITON (Transport Rigor Implemented for Transient Depletion with ORIGEN) is a SCALE control module that can be used for problem-dependent cross-section weighting, 2-D transport calculations with NEWT (New ESC-based Weighting Transport code), 2-D depletion calculations through a coupling of NEWT and ORIGEN, and 3-D Monte Carlo depletion calculations coupling KENO and ORIGEN.

Given mixtures and lattice cell structures defined in input, TRITON controls cross-section processing operations using BONAMI to perform Bondarenko calculations for resonance self-shielding in the unresolved resonance range and using CENTRM/PMC for resolved resonance evaluation. The

*For further information about SCALE code see http://scale.ornl.gov/index.shtml

problem-dependent cross-section library and mixing table produced by the sequence are automatically used in the NEWT or KENO calculation so that no mixing table needs to be specified.

The transport solution is followed by COUPLE and ORIGEN calculations. In depletion mode, NEWT creates a three-group weighted library based on calculated and volume-averaged fluxes for each mixture. COUPLE updates the ORIGEN-S cross-section library with cross-section data read from the weighted library. Three-group fluxes calculated by NEWT or KENO are supplied to ORIGEN for depletion calculations. COUPLE/ORIGEN calculations are repeated for each mixture being depleted, as specified by the user, using mixture-specific cross-section data and fluxes. Used in conjunction with TRITON, NEWT also can generate a library of cross-sections as a function of burnup, with a branch capability that provides cross-sections at each burnup step for perturbations in moderator density, fuel and moderator temperatures, boron concentration, and control rod insertion or removal.

Reactor physics problems are solved by the sequential application of the codes described above. Given the sequence for which a calculation is to be performed, TRITON is responsible for processing input, converting the input description to appropriate forms, and executing each module in sequence, with preparation and exchange of required data between modules.

Methods used by TRITON

The use of cross-section data libraries that correctly define nuclear reaction rates during irradiation is necessary to obtain accurate calculations. The cross-sections change as a function of burnup, enrichment, and operating conditions and depend on the fuel assembly design. ORIGEN (Oak Ridge Isotope Generation and Depletion) can provide burnup-dependent cross-sections produced via problem-specific transport calculations and simultaneously track every activation, fission, and decay event for which data are available. ORIGEN currently tracks 1119 individual fission products generated in the fuel during irradiation, 129 actinides, and 698 isotopes associated with structural and/or activation components. [DeHart and S.M. 2011] ORIGEN reads a set of cross-sections from a library created for a generic LWR fuel assembly. Since mixture cross-sections and spatial fluxes change with burnup, the TRITON depletion sequence is made up of two updates of cross-sections. A TRITON iteration is divided in two phases:

- transport calculation for cross-section processing and transport solution;
- depletion calculation with COUPLE and ORIGEN.

COUPLE collapses the multigroup cross-sections from NEWT or KENO for use in ORIGEN. Transport calculations are used to calculate fluxes and prepare weighted cross-sections; depletion calculations are used to update

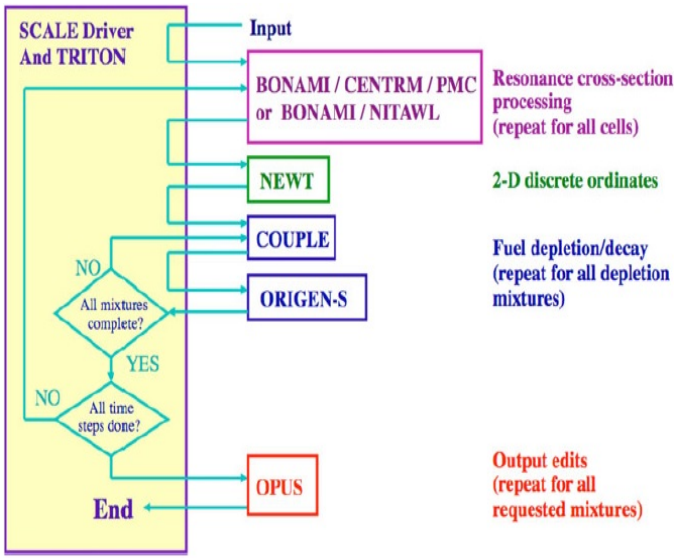

Figure 3.1: The TRITON/NEWT depletion sequence

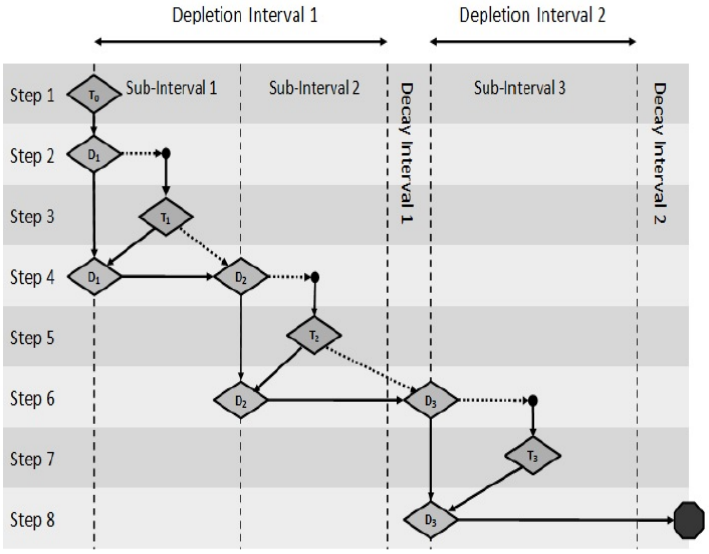

Figure 3.2: The predictor-corrector approach

nuclide concentrations, which are used in the following transport calculation. The TRITON/NEWT depletion sequence was used in our calculations and is illustrated in [Figure 3.1].

TRITON uses a predictor-corrector approach to process the user-defined depletion scheme. This method is better described in 3.7.1. The predictor-corrector approach updates the cross-sections by performing a transport solution based on anticipated concentrations at a time halfway through a given depletion period. Depletion calculations are then performed over a constant-power burn period using fluxes and cross-sections predicted for mid-cycle. Depletion calculations are then extended to a point halfway through the next cycle, followed by another mid-cycle transport calculation. This process is repeated until depletion calculations are completed for all cycles in a depletion case. This process results in cross-sections representative of the predicted mid-cycle burnup, which are applied in the second-pass depletion over all fuel cycles. In order to start the calculation, a "bootstrap case" is required using initial isotope concentrations for the initial cross-section processing and transport calculation. This process is illustrated in [Figure 3.2]. In this figure, transport and depletion calculations are represented by the labels "T" and "D", respectively.

By default, TRITON creates a single library at the midpoint of each cycle used to approximate cross-sections over the full cycle. In practice, it is often the case that a cycle is long enough that significant isotopic changes do occur and a one-step approach gives inadequate temporal discretization. The TRITON depletion sequence allows for refinement of the cross-section update time interval by allowing more intermediate steps within each cycle.

Cross-section libraries are created at the midpoint of each subinterval; because the accumulated burnup is reduced within each interval, the use of an average cross-section for each interval is an improved approximation. Obviously, in the limit, as the number of intervals goes to infinity, the approximation goes to the exact solution. However, because changes in multigroup cross-sections occur relatively slowly with burnup, only a minimal set of cross-section updates are generally required within a depletion cycle.

ORIGEN solves the Bateman equations, introduced in 3.5, by means of matrix exponential method (3.6.1). For a more comprehensive explanation of how ORIGEN works and of its use of Bateman equations see [Gauld et al. 2011].

3.4.2 SERPENT

SERPENT[†] is a continuous energy Monte Carlo reactor physics code. The development of SERPENT started at VTT Technical Research Centre of Finland in 2004, with the title "Probabilistic Scattering Game", or PSG. The

[†]For further information about SERPENT code see http://montecarlo.vtt.fi

name was later changed to SERPENT, due to the various ambiguities related to the acronym. The code was submitted for public distribution to the NEA Data Bank in April 2009 and released one month later. Since the public release of SERPENT 1.1.7 in May 2009, the user community has grown to 300 users in 111 universities and research organizations in 29 countries around the world. [*SERPENT website* 2014]

SERPENT is distributed through OEDC/NEA Data Bank. [*OECD/NEA Data Bank Computer Program Services* 2014]

SERPENT is divided in two separate branches: SERPENT 1 is the official released version and SERPENT 2 is a complete rewrite still in beta-testing. The main goal of SERPENT 2 was to extend the burnup capability from 2D assembly-level calculations to full-core problems consisting of hundreds of thousands of depletion zones, without any limitations in parallelization. The new features of SERPENT 2 are a multi-physics interface for efficient coupling with thermal hydraulics codes and a complete redesign of memory management, which lends itself to memory efficient OpenMP-MPI hybrid parallelization and allows the memory hungry optimization features of SERPENT 1 to be turned off if needed.

The transport routines of SERPENT have numerous performance improving features. Between these there are the mixed use of ray tracing and delta tracking methods during neutron transport, a uniform energy grid for all neutron interaction data, pre-calculated energy dependent total cross-sections for various reaction types, and calculation of one-group cross-sections from high resolution spectra rather than tallying them directly. The burnup capability in SERPENT is entirely based on built-in calculation routines, without any external coupling. The number of depletion zones is not restricted, although memory usage becomes a limiting factor for SERPENT 1 when the number of burnable materials is large.

Methods used by SERPENT

Burnup calculation The burnup capability in Serpent is entirely based on built-in calculation routines, without any external coupling. The number of depletion zones is not restricted, although memory usage becomes a limiting factor for Serpent 1 when the number of burnable materials is large. Predictor-corrector calculation is optional and used by default for each burnup step. In addition to the conventional predictor-corrector method based on linear interpolation, Serpent 2 offers various higher-order methods and sub-step solutions for burnup calculation.[Isotalo and Aarnio 2011a, Isotalo and Aarnio 2011b]

Radioactive decay and fission yield data used in the calculation are read from standard ENDF format data libraries. The decay libraries may contain data for almost 4000 nuclides and meta-stable states, all of which is available for the calculation. The total number of different nuclides produced from

fission, transmutation and decay reactions is generally lower, in the order of 1500. The concentrations of all included nuclides with decay data are tracked in the burnup calculation and the number of nuclides with cross-sections typically ranges from 200 to 300. Energy-dependent fission yields are available for all main actinides (31 nuclides in ENDF/B-VII data).

Integral one-group transmutation cross-sections are calculated either within the transport cycle or by collapsing the continuous-energy reaction cross-sections after the cycle using a flux spectrum collected on the unionized energy grid. The spectrum collapse method speeds up the calculation by a factor of 3-4 and, due to the high energy resolution of the flux spectrum, the errors in the results are practically negligible.

Serpent has two fundamentally different options for solving the Bateman depletion equations. The first method is the Transmutation Trajectory Analysis method (described in 3.6.2), based on the analytical solution of linearized depletion chains. The second option is the Chebyshev Rational Approximation Method (3.6.1), an advanced matrix exponential solution developed for Serpent at VTT. The two methods have shown to yield consistent results, both when used with Serpent [Leppänen and Pusa 2009] and in separate methodological studies [Isotalo 2011].

Fission product poison ^{135}Xe can be handled separately from the other nuclides and iterated to its equilibrium concentration during the transport simulation. The equilibrium calculation is independent of the depletion routine, and the iteration can also be performed in transport mode without burnup calculation.

Woodcock delta-tracking method The Monte Carlo simulation can be run either in k-eigenvalue criticality source or external source mode (for the differences between these two modes see [Leppänen 2007, pages 112-116]). Neutron transport is based on a combination of conventional surface-to-surface ray-tracing and the Woodcock delta-tracking method (to further deepen Woodcock delta-tracking method [Lux and Koblinger 1991, pages 222-226]). The tracking routine has proven efficient and well suited for geometries where the neutron mean-free-path is long compared to the dimensions, which is typically the case in fuel assemblies. The combination of two tracking methods overcomes the efficiency problems normally encountered with delta-tracking in the presence of localized heavy absorbers.

The main drawback of delta-tracking is that the track-length estimate of neutron flux is not available and reaction rates have to be calculated using the potentially less-efficient collision estimator. This is usually not a problem in reactor calculations when reaction rates are scored in regions of high collision density.

Interaction physics and geometry Serpent reads continuous-energy cross-sections from ACE format data libraries. The interaction physics is based on classical collision kinematics, ENDF reaction laws and probability table sampling in the unresolved resonance region.

Serpent includes ACE format cross-section libraries based on JEF-2.2, JEFF-3.1, JEFF-3.1.1, ENDF/B-VI.8 and ENDFB/B-VII evaluated data files. Interaction data are available for 432 nuclides at 6 temperatures between 300 and 1800K. A built-in Doppler-broadening preprocessor routine allows the conversion of ACE format cross-sections into a higher temperature. This capability results in a more accurate description of the interaction physics in temperature-sensitive applications, as the data in the cross-section libraries are available only in 300K intervals.

Serpent has also thermal bound-atom scattering data for light and heavy water and graphite. Since the data format is shared with MCNP, any continuous-energy ACE format data library generated for MCNP can be used with Serpent as well.

SERPENT uses a universe-based combinatorial solid geometry (CSG) model, also implemented by MCNP and KENO-VI, to build the geometry. This model allows the description of practically any two- or three-dimensional fuel or reactor configuration. The geometry consists of material cells, defined by elementary quadratic and derived macrobody surface types.

Unionized energy grid format To speed up the calculations with a great reduction of the number of CPU time consuming grid search iterations a unionized energy grid is used for all reaction modes. Continuous-energy cross-sections in the library files are reconstructed on this single energy grid. Macroscopic cross-sections for each material are pre-generated before the transport simulation. Instead of calculating the cross-sections by summing over the constituent nuclides during tracking, the values are read from pre-generated tables, which is another effective way of improving the performance.

The drawback of the unionized energy grid approach is that there is a wasting of computer memory to allow the redundant data points to be stored. In burnup calculations, in which over 250 actinide and fission product nuclides may be involved, the grid size may become prohibitively large.

3.5 Bateman equations

Some nuclides are naturally radioactive and decay to other nuclides over time. The product might still be unstable, causing it to decay further and so on, creating a chain of decays. Some nuclides can undergo different types of decays leading to different daughter nuclides. Decay chain can thus have branches, which might or might not unite later on.

Moreover nuclides can react with neutrons in different ways and transmute

themselves into other nuclides. Also interactions with gamma rays and other particles can cause similar reactions but they are ignored in burnup calculations for their little significance. [Isotalo 2013]

Decay always proceeds towards less energetic states, while transmutation reactions can also produce nuclides in more energetic states, thanks to the kinetic and binding energy of the incident particle. So, in theory, any nuclides can become any other nuclide with an unrealistic number of decay and transmutations.

The nuclear fuel changes its properties because of changes in composition due to fuel burnup. During the operation the fuel nuclei are transmuted by neutron capture and subsequent decay.

The equations governing decay and transmutation of an arbitrary mixture of N different nuclides in a homogenized material region can be written as

$$\frac{dN_i}{dt} = -\lambda_i^{eff} N_i + \sum_j^N b_{j,i}^{eff} \lambda_j^{eff} N_j \quad \text{for i=1,...,N,} \tag{3.2}$$

where N_i is the atomic density of nuclide i; λ_i^{eff} the effective decay constant of nuclide i, and $b_{i,j}^{eff}$ the effective branching ratio from nuclide i to nuclide j. These are defined as

$$\lambda_i^{eff} = \lambda_i + \phi \sum_j \sigma_{i,j} \tag{3.3}$$

and

$$b_{i,j}^{eff} = \frac{b_{i,j}\lambda_i + \sigma_{i,j}\phi}{\lambda_i^{eff}}, \tag{3.4}$$

where λ_i is the decay constant of nuclide i , ϕ the one-group neutron flux, $\sigma_{i,j}$ the microscopic one-group cross-section for transmutation of nuclide i to nuclide j and $b_{i,j}$ the branching ratio from nuclide i to nuclide j, i.e. the fraction of natural decays of nuclide i that produce nuclide j.

[Isotalo 2011] These equations are known as Bateman equation after Harry Bateman, who first solved them analytically for a linear chain of decay reactions. [Bateman 1910] The equations formulated by Ernest Rutherford [Rutherford 1905] didn't include branching or transmutation, which had not yet been discovered.

There are two difficulties in solving the Bateman equations. First material compositions and neutron flux affect each other leading to a complex combined problem. This problem can be handled by sequentially solving neutronics and material compositions, while assuming the other to remain constant.

Second the system is large and stiff, with thousands of nuclides with half-lives varying from seconds to millions of years. However most of the nuclides are unimportant and can be lumped together in a single pseudo-nuclide that has averaged properties. Furthermore it is possible to remove some short-lived nuclides assuming their instantaneous decay. The great majority of nuclides

can be removed without significantly affecting the neutronics, but which approximations are valid for which nuclides varies from case to case, so the approximations may lead to a degree of problem dependence.

3.6 Methods to solve Bateman equations

There are several ways to solve the system of linear first order differential equations with constant coefficients, represented by the Bateman equations with the assumption of constant reaction rates during the time step. Nevertheless the size and stiffness of the system reduce the number of methods that can be used.

3.6.1 Matrix exponential method

The Bateman equations can be written in a matrix form $d\overrightarrow{N}/dt = A\overrightarrow{N}$, where $A_{i,j} = -\lambda_i^{eff}\delta_{i,j} + b_{j,i}^{eff}\lambda_j^{eff}$. The solution of this equation is $\overrightarrow{N}(t) = e^{At}\overrightarrow{N}(0)$, which employs the matrix exponential notation

$$e^{At} = \sum_{m=0}^{\infty} \frac{1}{m!}(At)^m. \tag{3.5}$$

Different approximations are used to evaluate the matrix exponential in the matrix exponential method. There are numerous algorithms for computing the matrix exponential, but many of them are not applicable in burnup calculations, due to their computational expense or their dubious numerical quality. The approximation of the matrix exponential is difficult, because of great variability of the decay constants and reaction rates of the nuclides that induce the burnup matrix to have a wide spectrum of eigenvalues. One of the most challenging problems is represented by the short-lived nuclides because they can induce eigenvalues of arbitrarily large magnitude. These difficulties have traditionally been solved by simplifying burnup chains or by treating the most short-lived nuclides separately when computing a matrix exponential solution. The characteristics of the problem are substantially one of the main criteria of the selection of a suitable matrix exponential method. When choosing the matrix exponential method, the key aspects that should be taken into consideration are the norm and eigenvalue spectrum of the burnup matrix as well as the length of the time step. [Pusa and Leppänen 2010]

Hereafter the Chebyshev rational approximation method (CRAM) is described, because of its use in the SERPENT code.

Chebyshev rational approximation method

CRAM method is based on the observation that the eigenvalues of the depletion coefficient matrix A appear to be clustered around the negative real

axis. This can be exploited by making a Chebyshev rational approximation of the exponential function for the interval $(-\infty, 0]$. The resulting rational function is then decomposed into a pole-residue form to avoid numerical instability. When the denominator and numerator orders are selected equal and even in the Chebyshev approximation, the poles form conjugate pairs and the imaginary parts cancel out for a real valued variable. Thus, an order (k, k) approximation becomes

$$e^z \approx \frac{P_k(z)}{Q_k(z)} = a_0 + \sum_{i=1}^{k} \frac{a_i}{z + \theta_i} = a_0 + 2\Re \sum_{i=1}^{k/2} \frac{a_i}{z + \theta_i}, \tag{3.6}$$

where P_k and Q_k are polynomials of order k, whose coefficients have been selected to minimize absolute deviation from exponential function on the negative real axis, a_0 is the limiting value of the approximation at infinity, and a_i and θ_i are the residues and poles.

When this approximation is applied to the matrix exponential it becomes

$$\overrightarrow{N}(t) = a_0 \overrightarrow{N}(0) + 2\Re \left[\sum_{i=1}^{k/2} a_i (At + \theta_i I)^{-1} \right] \overrightarrow{N}(0), \tag{3.7}$$

where the matrix inversions can be calculated efficiently thanks to the sparse structure of the matrix A. There is no reason to select any particular value of k as long as it is even.

3.6.2 Transmutation Trajectory Analysis

In this section the Transmutation trajectory analysis (TTA) is described. Then, only for the sake of completeness, the Bateman solution is outlined.

Transmutation trajectory analysis, also known as the linear chains method, is an alternative method for solving the decay and transmutation equations analytically, if the complicated transmutation chains are first resolved into a set of linear sub-chains, or trajectories. [Leppänen and Pusa 2009] Since the Bateman equation is a set of first-order linear differential equations, the general solution can be obtained as a linear superposition of the solutions in simpler cases.

A transmutation trajectory is a sequence of direct nuclide to nuclide transitions, from the first to the last nuclide with all the possible reaction modes. After the assumption that only the first nuclide of the chain has non-zero initial atomic density, the method proceeds calculating the concentrations of nuclides of each chain. Doing this for each nuclide in the initial composition and superposing the results, the solution of the original problem is obtained. Constructing and solving the decay and transmutation chains individually provides TTA with an additional advantage over the matrix exponential method in being able to extract detailed data about the individual chains.

In a transmutation rich environment, such as a nuclear reactor, is impossible to consider all chains since the web of decay and transmutation reactions is too complicated. Because most of the chains are passed through by an insignificant amount of nuclides, these chains are practically meaningless and so it is possible to terminate the construction of a chain when the significance of the rest of it falls below a certain limit.

Now a recent general analytic solution by Cetnar [Cetnar 2006] is introduced, which allows an arbitrary number of repeated effective decay constants. When this solution is used, the only approximation left is the termination of chains of low importance.

For a chain of n nuclides that has d distinct effective decay constants , each repeated m_i times ($\sum_{i=1}^{d} m_i = n$), the general solution is

$$N_n(t) = N_1(0)\frac{B_n}{\lambda_n^{eff}}\sum_{i=1}^{d}\lambda_i^{eff}\alpha_i e^{-\lambda_i^{eff}t}\sum_{m=0}^{\mu_i}\frac{\lambda_i^{eff}t}{m!}\Omega_{i,\mu_i-m}, \tag{3.8}$$

where $\mu_i = m_i - 1$ is used to simplify notation,

$$B_n = \prod_{j=1}^{n-1} b_{j,j+1}^{eff}, \tag{3.9}$$

$$\alpha_i = \prod_{j=1,j\neq i}^{d}\left(\frac{\lambda_j^{eff}}{\lambda_j^{eff}-\lambda_i^{eff}}\right)^{m_j} \tag{3.10}$$

and

$$\begin{aligned}\Omega_{i,j} = &\sum_{h_1=0}^{j}\cdots\sum_{h_{1-1}=0}^{j}\sum_{h_{1+1}=0}^{j}\cdots\sum_{h_d}^{j} \\ &\prod_{k=1,k\neq i}^{n}\binom{h_k+\mu_k}{\mu_k}\left(\frac{\lambda_i^{eff}}{\lambda_i^{eff}-\lambda_k^{eff}}\right)^{h_k}\delta\left(j,\sum_{l=1,l\neq i}^{d}h_l\right),\end{aligned} \tag{3.11}$$

where δ is the Kronecker delta.

The Bateman solution

A linear chain with n distinct effective decay constants, λ^{eff}, i=1,..., n and branching ratios $b_{i,i+1}^{eff}$ can be solved analytically. Assuming that only the first nuclide has a nonzero initial atomic density, $N_1(0)$, the atomic density of the n^{th} nuclide after time t is

$$N_n(t) = N_1(0)B_n\sum_{i=1}^{n}\alpha_i^n e^{-\lambda_i^{eff}t}, \tag{3.12}$$

where

$$\alpha_i^n = \frac{\prod_{j=1}^{n-1} \lambda_j^{eff}}{\prod_{j=1,j\neq i}^{n}(\lambda_j^{eff} - \lambda_i^{eff})}. \tag{3.13}$$

If the effective decay constants in the chain are not distinct, the Bateman solution cannot be applied. This is the case of cyclic chains, but might also happen in other cases if identical decay constants are input for separate nuclides. By relying on the weakness of cyclic chains and terminating the chain when a loop is encountered, the problem is avoided. A more accurate approximation is to introduce small variations to the repeated constants to make them distinct, after which the 3.8 can be used. Since the effective decay constants are usually only known to a few decimal places these variations are easily kept below the level of uncertainty in initial data.

When there are no repeats, i.e., $m_i = 1$ for all i, 3.8 reduces to the Bateman solution 3.12.

3.7 Burnup algorithms

Burnup algorithms, also called coupling schemes, are used to select the constant values of cross-sections and flux for the depletion calculations. Depletion calculations have the purpose to follow the time development of the material compositions and dependent neutronics parameters of a nuclear reactor core, i.e., they focus on long-term changes. Instead the development of the neutronics is essentially quasi-static. This complex combined problem can be modeled by sequentially solving the neutronics and changes in material compositions while assuming the other to remain constant.

Various methods exist for performing these calculations, but they can be divided in two groups.

The first group uses the cross-sections and flux obtained from solving the neutronics to calculate the momentary derivatives of the atomic densities and uses them in a numerical integration with a general purpose ordinary differential equation (ODE) solver. These methods are fast but require short-lived nuclides to be removed from the system to reduce stiffness.

The second group solves changes in the material compositions at each step by evaluating explicit solutions to the Bateman equations with constant microscopic reaction rates. A depletion step with a Bateman solver takes much more CPU time than one with an ODE solver, but some of the available algorithms are accurate, robust and able to handle the full range of half-lives, which simplifies result handling and makes the algorithms problem independent as all nuclides can be modeled explicitly. Such methods are particularly popular with Monte Carlo neutronics as they can be made problem independent and allow for longer steps. [Isotalo and Aarnio 2011b] Longer steps mean that less time is needed to have the Monte Carlo solution.

When a method from the second group is used, one has first to predict the development of the reaction rates during the step and then further approximate these predictions with their averages in the depletion calculation.

The steady state neutronics and Bateman solutions are combined with a wrapper algorithm that uses one or more neutronics solutions to predict the development of the cross-sections and flux, or reaction rates, over a single step and selects constant reaction rates to represent these predictions in the Bateman solutions. Despite their seeming simplicity, or perhaps because of it, the wrapper algorithms have received very limited attention and seem to be lagging behind the neutronics and depletion solvers in development. Usually the behaviour of the cross-sections and flux is predicted with some predictor–corrector method using zeroth and first order predictions or other comparable approximations.

3.7.1 Predictor-corrector algorithms

One way to perform burnup calculations is to proceed in steps: first neutronics is solved with the beginning of step (BOS) material composition and then are solved the changes in material compositions with the reaction rates that stay constant at their initial values. The obtained end of step (EOS) compositions then become the BOS compositions for the next step. This method is called the explicit Euler method even if the real Euler method would calculate BOS derivatives and assume them constant at each step, instead of the microscopic reaction rates. For instance, below is described the Euler method [Algorithm 1]. This method is also known as the beginning-of-step constant flux approximation. [Dufek and Hoogenboom 2009] Instead of using the BOS

Algorithm 1 The Euler method

input: N_0

for $n = 0, 1, \ldots$ **do**
$\phi_n \leftarrow$ solution of $B(N_n)\phi_n = 0$
$N_{n+1} \leftarrow N_n \exp \mathbb{M}(\phi_n)\Delta t_n$

end for

reaction rates for the entire step, that is a coarse approximation unless short steps are used, a predictor-corrector method can be applied. The requirement of two rather than one neutronics solution per step and the consequent greater running time are compensated by improved accuracy. Moreover the bigger accuracy allows the use of twice longer steps.

The predictor-corrector approach performs cross-section processing and transport calculations based on anticipated isotope concentrations at the midpoint of a depletion subinterval. Depletion calculations are then performed

over the full subinterval using cross-sections and flux distributions predicted at the midpoint. Depletion calculations are then extended to the midpoint of the next subinterval (possibly through a decay interval and into a new depletion interval), followed by cross-section processing and transport calculations at the new midpoint. The iterative process is repeated until all depletion subintervals are processed. In order to start the calculations, a "bootstrap case" is required using initial isotope concentration for the initial cross-section processing and transport calculation. The bootstrap calculation is used to determine the anticipated isotope concentrations at the midpoint of the first depletion subinterval. [Jesse and DeHart 2011]

For instance, below is described the predictor-corrector algorithm [Algorithm 2] used by SERPENT code.

Algorithm 2 The predictor-corrector method

Input: N_0

for $n = 0, 1, \ldots$ **do**
$\phi_n \leftarrow$ fundamental mode of$B(N_n)$
$N_{n+1}^{(P)} \leftarrow N_n \exp \mathbb{M}(\phi_n)\Delta t_n$
$\phi_{n+1}^{(P)} \leftarrow$ fundamental mode of$B(N_{n+1}^{(P)})$
$\phi_n^{(C)} \leftarrow \left(\phi_n + \phi_{n+1}^{(P)}\right)/2$
$N_{n+1} \leftarrow N_n \exp \mathbb{M}(\phi_n^C)\Delta t_n$

end for

The predictor step of the method presented above uses the BOS cross-sections and flux for the entire step, which can be seen as using a constant extrapolation to predict their behaviour. The corrector steps can in turn be interpreted as linearly interpolating between the BOS and predicted EOS values, and using the average from this interpolation for the depletion calculations.

If it is wanted, higher order estimates can be used by using the BOS values from the previous step and the EOS values of the current step. In this way it will be possible to substitute the constant and linear interpolations with the linear and quadratic ones respectively. The running time won't be affected by this action because no additional neutronics solutions will be needed.

As shown by A.E. Isotalo and P.A. Aarnio, [Isotalo and Aarnio 2011a] using linear extrapolation on the predictor steps improve the results for long-lived nuclides compared with the ones using the constant extrapolation.

The results from the use of the second order predictions on the corrector steps are not so positive; on the contrary they are quite negative. On the authors' opinion the reason is that linear corrector results in systematic can-

cellation of errors which improves the results past those from a quadratic one, unless very short steps are used. Quadratic interpolation should clearly not be used if the predictor uses constant extrapolation, but when combined with linear extrapolation, the difference between quadratic and linear interpolation is not as conclusive. The predictor and corrector orders had little direct effect on short-lived nuclides.

3.8 Xenon oscillations in Monte Carlo calculations

Xenon driven oscillations have been found in many burnup algorithms. These oscillations differ from physical xenon oscillations because of the time discretization [Isotalo, Leppänen, and Dufek 2013].

In real reactors the xenon oscillations are prevented by active control. Due to various approximations, oscillations in numerical calculations can be much worse than they would in real reactors. A way to handle this problem could be modelling explicitly the control system. This solution would be extremely effortful or even not feasible in Monte Carlo calculations. Therefore a simpler alternative is necessary.

The spatial oscillations that happen in deterministic codes are usually solved by forcing equilibrium at each time step. To do this, special wrapper algorithms can be used. These algorithms perform multiple neutronics solutions to find the equilibrium distributions and the corresponding flux, which is then used for depletion. This approach has also been used in Monte Carlo burnup calculations [Dufek and Gudowski 2006].

Another way that is feasible in Monte Carlo neutronics is to calculate the equilibrium xenon distributions inside the criticality source simulation.

3.8.1 Xenon physical properties

^{135}Xe is produced directly from fission, but the combined direct yield of ^{135}Xe and $^{135\mathrm{m}}$Xe ($T_{1/2} = 15$min) from thermal fissions is only around 0.2%, and by the decay of ^{135}Te, through ^{135}I. These two precursors, together with ^{135}Sb, have a combined yield of 6%. ^{135}Te decays to ^{135}I in about 19 seconds, while ^{135}I has a half-life of 6.7 hours. ^{135}Xe ($T_{1/2} = 9.2$ h) decays to ^{135}Cs, which in turn decays to the stable nuclide ^{135}Ba with a half-life of about 2.3 millions of years. ^{135}Xe has a very large thermal absorption cross-section ($2.6 \cdot 10^6$ barns): this causes its disappearance for transmutation and gives it a deep effect on neutronics. [Guerrini and Paci 1998] Because of these phenomena, changes in the flux affect xenon production rate with a delay, whereas is removal rate, which is dominated by absorption, changes instantly.

If it is assumed that ^{135}I is produced directly from fission with yield γ^{Te}, the equations that govern the xenon and iodine concentration may be written

as:

$$\frac{dI}{dt}(t) = \gamma^{Te}\Sigma_f - \lambda^I I \tag{3.14a}$$

$$\frac{dX}{dt}(t) = \gamma^X\Sigma_f\phi + \lambda^I I - \left(\lambda^X + \sigma_a^X\phi\right)X, \tag{3.14b}$$

where Σ_f is the macroscopic fission cross-section, λ^X and λ^I are the xenon and iodine decay constants, γ^{Te} and γ^X are the tellurium and xenon fission yields, ϕ is the neutron flux, σ_a^X is the xenon absorption cross-section, I is the iodine concentration and X is the xenon concentration. When the flux tilts, reactivity increases in the areas of high flux as xenon is depleted, while in the areas of low flux reactivity decreases as xenon builds up. The flux tilt is reinforced by these changes in reactivity, leading to even larger changes. Over the time the ^{135}I concentration stabilizes and the xenon concentration starts to increase in high flux areas while decreases in the low flux areas. Because of this the flux can begin to tilt in the opposite way and so the cycle repeats. These physical oscillations are prevented by the use of the control system because their time period (some hours) is much longer than the time required for the control rods movement (few seconds).

3.8.2 Xenon numerical effects

The physical xenon oscillation mechanism is not possible in burnup calculations due to the time steps shorter than the timescale involved in xenon oscillations. This allows that ^{135}I and ^{135}Xe reach the saturation level corresponding to the flux at each step.

However an unphysical oscillation is possible: if the flux is tilted, during the depletion step there will be high xenon concentration in the areas with high flux and low xenon concentration in the areas with low flux. So in the following neutronics solution the flux will tilt in the opposite way.

The predictor-corrector algorithm performs two neutronics solutions per step and so the behaviour can be more complex. Moreover it is not easy to detect instability. In fact the results of the calculations are the material compositions and the related neutronics, which are calculated at the beginning of step. Because they come from the same phase of the oscillation, they may seem stable, but the materials were depleted with flux that might not at all represent the ones in the output. The material compositions can also be completely off as the averaged flux used to calculate them is in no way guaranteed to represent the correct one.

The results may seem stable and so the comparison of the results of following burnup steps is not sufficient to assure that a calculation is stable. A straightforward method to discover the oscillations is to measure the difference between the local fluxes in the predictor and corrector steps. These differences are a normal part of predictor-corrector methods and it is not possible to fix a threshold for the width that implies instability.

Some studies [Dufek, Kotlyar, et al. 2013] demonstrate that numerical xenon oscillations occur even with relatively short steps and in higher order methods. In Isotalo 2013 the author concludes that the simplified computational models, with no feedbacks and control mechanisms, do not even describe the stable state we are trying to simulate.

3.8.3 Equilibrium xenon calculations

Since we want stable solutions and the problem of oscillations derives from the model, the model itself has to be changed. The simplest way to achieve this is to directly require that the flux and saturated xenon concentrations must remain in a mutual equilibrium.

As already said, some deterministic codes use wrapper algorithms to obtain the equilibrium xenon distribution and the corresponding flux, which is then used for depletion. The problem to use this method also in Monte Carlo calculations is that the equilibrium has to be iterated every time the neutronics is solved. In Monte Carlo burnup calculations this is made impossible by the high computational cost of the neutronics.

An alternative is to calculate the equilibrium xenon distributions and the neutron flux during the normal transport calculation. In this way the transport simulation becomes slightly longer than a normal one. The algorithm used by SERPENT forces the xenon concentrations and neutron flux to remain in equilibrium and prevents all xenon driven oscillations: the equilibrium calculation is performed during a criticality source simulation by recalculating the concentrations of ^{135}I and ^{135}Xe after each source cycle using the flux and cross-sections tallied during that cycle. The concentrations obtained in that way are used during the next source cycle. Thus a continuous iteration between neutronics and the equilibrium concentration of ^{135}I and ^{135}Xe is performed as the transport simulation is run. For this reason the concentrations of these two nuclides change through all inactive and active cycles. This algorithm causes a $\sim 10\%$ increase in the running time per neutron history, as demonstrated in Isotalo, Leppänen, and Dufek 2013.

Even with the use of this equilibrium method, strong oscillations can occur with too long steps. So the equilibrium xenon does not provide complete stability, but it allows to perform calculations with reasonable step lengths. Geometry, material compositions and power density affect the step length at which oscillations start.

The results obtained after having forced equilibrium are only as accurate as the model they have been calculated for. Forcing equilibrium without modelling the feedback and control systems that would stabilize a real reactor means that their effects on the equilibrium distributions are ignored.

3.8.4 Stochastic Implicit Euler Method

Another method for stabilizing Monte Carlo burnup calculations is the Stochastic Implicit Euler (SIE). This method is a wrapper algorithm, but merges the equilibrium and burnup algorithms to ensure that, while multiple transport solutions are required, they all contribute to the final estimates. The SIE method is presented in algorithm 3, where c denotes the number of iterations, N is the nuclide concentration and Φ is the neutron flux. The abbreviation EOS means "end of step", as in the previous chapters.

Algorithm 3 The Stochastic Implicit Euler method

for $i = 0, 1, \ldots, I-1$ **do** % Loops over steps
$N_{i+1}^0 \leftarrow N_i$ % Initial guess
  for $j = 0, 1, \ldots, c-1$ **do** % Iteration
  $\Phi_{i+1}^j \leftarrow \Phi\left(N_{i+1}^j\right)$ % EOS neutronics
  $\overline{\Phi_{i+1}^j} \leftarrow \frac{1}{j+1} \sum_{k=}^{j} \Phi_{i+1}^k$ % Average over iterations
  $N_{i+1}^{j+1} \leftarrow e^{A(\overline{\phi})(T_{i+1}-T_i)} x_i$ % Recalculated EOS compositions
  end for
$N_{i+1} \leftarrow N_{i+1}^c$ % Final results for step i+1
$\Phi_{i+1} \leftarrow \overline{\Phi_{i+1}^c}$
end for

The greatest advantage of this method is that it is not xenon specific and should also prevent the oscillations that arise when using longer steps with the equilibrium xenon method. SIE has also two disadvantages

- it uses constant backwards extrapolation for predicting the behaviour of the cross-sections and flux;
- the overhead associated with initializing the transport simulation, converging source distribution, storing results, depleting materials and calculating averages is multiplied.

The former causes that the SIE method could become no more accurate than the constant forward extrapolation of the explicit Euler method. Thus short steps are required to produce accurate results, which renders the main advantage useless. The latter is due to the fact that, even when running the same number of active neutron histories, they are spreaded over multiple transport calculations with different materials.

The fact that the initial unconverged iterations are used for in the final results might also make the results worse than the number of contributing histories would suggest.

3.9 Validity of a Monte Carlo simulation

The use of Monte Carlo methods allows the modelling of complex geometries with minimal approximations. However, it is difficult and time consuming to obtain good statistics for localized tallies in eigenvalue calculations. To minimize the errors it is important to comprehend the issues that can induce these errors.

The convergence of the fission source is the first issue to deal with in assessing the validity of a Monte Carlo calculation. The combined observation of the k-eff and the Shannon entropy, defined in the following paragraph 3.9.3, as a function of cycles, is the fundamental method to find when the fission source is converged [Mervin and Maldonado 2011]. Several Monte Carlo codes, including SERPENT, give the values of k-eff and Shannon entropy and this makes possible to understand when the fission source has reached a stationary distribution.

Another important problem is how the cycle-to-cycle correlations affect the statistical estimates. In cases with a dominance ratio, i.e. the ratio of the second largest eigenvalue to the maximum eigenvalue, close to one, these correlations can originate under predictions in the uncertainty of the k-eff by a factor of five or higher [Team 2005].

In the next paragraphs the power iteration procedure to solve the transport equation will be shown and some considerations about the convergence of k-eff and the Shannon entropy will be drawn.

3.9.1 Power iteration procedure in Monte Carlo

The k-eigenvalue transport equation in standard form

$$\begin{aligned}&\left[\Omega\cdot\nabla+\Sigma_T(\overrightarrow{r},E)\right]\Psi(\overrightarrow{r},E,\Omega)=\\&=\iint\Psi(\overrightarrow{r},E',\Omega')\Sigma_S(\overrightarrow{r},E'\rightarrow E,\Omega\cdot\Omega')d\Omega'dE'\\&+\frac{1}{k_{eff}}\frac{\chi(E)}{4\pi}\iint\nu\Sigma_F(\overrightarrow{r},E')\Psi(\overrightarrow{r},E',\Omega')d\Omega'dE'\end{aligned}\tag{3.15}$$

can be written [Brown 2009] as

$$(L+T)\Psi=S\Psi+\frac{1}{k_{eff}}M\Psi\tag{3.16}$$

and then rearranged to

$$\Psi=\frac{1}{k_{eff}}(L+T-S)^{-1}M\Psi=\frac{1}{k_{eff}}F\Psi\tag{3.17}$$

Equation 3.17 may be solved numerically using the standard power iteration method

$$\Psi^{n+1}=\frac{1}{k_{eff}^{n}}F\Psi^{n}\qquad\text{n=0,1,...}\tag{3.18}$$

given k_0^{eff} and Ψ_0 . Concerning the relative convergence of k-eff and the fission source distribution during the power iteration process, if Ψ_0 is expanded in terms of the eigenvectors u_j of Eq. 3.16,

$$\overrightarrow{u_j} = \frac{1}{k_j} F \overrightarrow{u_j}, \tag{3.19}$$

with $k_0 > k_1 > k_2 > \dots$ substituted into Eq. 3.18, and rearranged with some straightforward algebra, then

$$\Psi^{n+1}(\overrightarrow{r}) = \overrightarrow{u_0}(\overrightarrow{r}) + \frac{a_1}{a_0}\rho^{n+1} \cdot \overrightarrow{u_1}(\overrightarrow{r}) + \dots, \tag{3.20}$$

$$k_{eff}^{n+1} = k_0 \Big[1 - \frac{a_1}{a_0}\rho^n (1-\rho) g_1 + \dots \Big] \tag{3.21}$$

where k_0 and $\overrightarrow{u_0}$ are the fundamental mode eigenvalue (exact k-eff) and eigenfunction, k_1 and $\overrightarrow{u_1}$ are the first higher mode eigenvalue and eigenfunction, ρ is the dominance ratio (k_1/k_0) and a_0, a_1 and g_1 are constants determined by the expansion of the initial fission distribution. Eq. 3.21 shows that higher-mode noise in the fission distribution dies off as ρ^{n+1}, while higher-mode noise in k-eff dies off as $\rho^n(1-\rho)$. When the dominance ratio is close to 1, k-eff will converge sooner than the fission distribution due to the extra damping factor $(1-\rho)$ which is close to 0. Thus, it is essential to monitor the convergence of both the fission source distribution and k-eff, not just that of k-eff.

3.9.2 Convergence of k-eff

The power iteration method is at the basis of eigenvalue Monte Carlo calculations, where single-generation random walks are carried out for a "batch" of neutrons to estimate k-eff and the next-generation fission distribution [Brown 2006].

The initial batches have to be divided into two groups:

- inactive, when the stationarity has not been reached;
- active, when the distribution is converged.

To have good results only the tallies that correspond to the active batches must be accumulated. Thus it is important to know when the convergence is reached and how many batches must be discarded. For this reason many codes perform a preliminary calculation and then examinate the trends of k-eff estimators to assess convergence. In this way it is possible to choose the correct number of active and inactive cycles and to start the real calculations. The convergence must be verified for the k-eff and also for the fission source distribution, since it will converge more slowly.

3.9.3 Use of Shannon entropy

The Shannon entropy, H_{src}, is useful to assess the behaviour of the fission source distribution. This parameter has its roots in the information theory and gives a single value for each batch. The Shannon entropy has a single stationary value when the source distribution reaches the convergence. The main advantage of dealing with this quantity is that it allows to avoid the plots of single-cycle k-eff or the multi dimensional plots of the source distribution versus cycle, given that these are more difficult to study than the plots Shannon entropy vs. batch [Brown 2006].

Hereafter the method to calculate the Shannon entropy is explained. A three dimensional grid must be imposed on all the fissionable regions: all the fission sites that fall into one of the grid boxes have to be counted. The resulting number is then used to form a discretized estimate of the source distribution, $\{P_j, j = 1, \ldots, N_s\}$, where N_s is the number of grid boxes in the imposed mesh, and P_j is the number of source sites in j-th grid box divided by the total number of source sites. Then, the Shannon entropy of the discretized source distribution for that batch is given by:

$$H_{rsc} = -\sum_{j=1}^{N_s} P_j \ln_2 P_j. \tag{3.22}$$

H_{src} is 0 for a point distribution and $\ln_2 N_s$ for a uniform distribution. Moreover, when P_j is close to 0, also $P_j \ln_2 P_j$ approaches 0.

It is important to point out that both k-eff and Shannon entropy convergence must be assessed before starting a criticality calculation. If one of these two parameters doesn't converge before the start of the active cycles, the calculation will produce wrong results.

Chapter 4

Submission of the OECD benchmark results

SCALE6.1 and SERPENT Monte Carlo code were tested on the OECD VVER-1000 LEU and MOX assembly computational benchmark [Kalugin et al. 2002]. The benchmark model will be presented in the first section of this chapter. In the following sections the results of this work will be presented.

For the purpose of this thesis, the results obtained with SCALE6.1 and SERPENT were compared with solutions from the OECD benchmark report. Six different solutions were provided by the six participants of this benchmark. Because of the computational nature of the benchmark itself, the average value of the solutions represents a reference and will be used to show the level of agreement among the values obtained in this work.

The solutions of the six participants were obtained with JEFF2.2 [The JEFF2.2 Nuclear Data Library 2000] or ENDF-B/VI.8 [Rose 1991] nuclear data. In this thesis work mainly the ENDF-B/VII [Chadwick et al. 2006] library was adopted, but also JEFF2.2 and JEFF3.1 [The JEFF3.1 Nuclear Data Library 2006] were used to compare the results of SERPENT with those of MCNP4B, used by one of the six benchmark participants, and TRIPOLI4 [Petrov, Todorova, and Kolev 2013]. This comparison is necessary to validate our reference solution with the Monte Carlo code SERPENT. ENDF-B/VI.8 was also tested with SCALE6.1 but no significant differences with respect to ENDF-B/VII have been noticed.

4.1 Benchmark models

The benchmark provides two different configurations that are representative of the advanced assemblies under active development in Russia for the VVER-1000 reactors. The purpose of these designs is to comply with the plutonium disposition mission. The assemblies of the benchmark exercise are:

- uniform LEU fuel assembly with 12 U/Gd rods (UGD variant);

- profiled MOX fuel assembly with 12 U/Gd rods (MOXGD variant).

As said in chapter 2, VVER-1000 fuel assemblies have a hexagonal geometry. One central tube, 312 fuel pin locations and 18 guide tubes are the components of the assembly. Zr-Nb alloys are utilized as clad and structural materials.

The UGD assembly [Figure 4.1] consists of low enriched fuel rods with $3.7wt.\%$ of uranium. These rods are named U1. The 12 rods poisoned with $4.0wt.\%$ of gadolinium (GD1) have a ^{235}U enrichment of $3.6wt.\%$.

The MOXGD assembly [Figure 4.2] contains fuel rods with three different plutonium loadings. The outermost ring of fuel rods (PU1) has a $2.0wt.\%$ of fissile plutonium (consisting of $93wt.\%$ of ^{239}Pu), while the two inner rings the $3.0wt.\%$ (PU2). The MOX pins located in the central region (PU3) have the hightest content of plutonium ($4.2wt.\%$). The U/Gd rods are the same of the UGD case and have the same location in the assembly.

Three different moderator materials are used in the benchmark, namely MOD1, MOD2 and MOD3, these representing light water with different densities ($0.7235g/cm^3$ in MOD1 and MOD2, $1.0033g/cm^3$ in MOD3), temperatures (see table 4.1) and boron concentrations (600 ppm in MOD1, 0 in MOD2 and MOD3).

The benchmark exercise comprises five calculation states, which cover both operational and cold conditions. These states are listed in [Table 4.1]. The five states were chosen to make possible to calculate some effects on reactivity. In fact, between step S1 and step S2 it is possible to see how xenon affects the calculation, between steps S2 and S3 it is possible to estimate the Doppler coefficient, between S3 and S4 the boron effect on reactivity is shown and finally between S4 and S5 the moderator temperature coefficient is calculated. The benchmark requires to perform depletion calculations for State S1 up to 40 MWd/kgHM with a power density of $108MW/m^3$ along with several branch calculations at specific burnup points for states S2-S5 using the isotopic compositions from the burnup calculations of state S1. The requested results include k-inf values, pin-by-pin fission rate distributions and nuclide concentrations for the ^{235}U, ^{236}U, ^{238}U, ^{239}Pu, ^{240}Pu, ^{241}Pu, ^{242}Pu, ^{155}Gd, ^{157}Gd, ^{149}Sm and ^{135}Xe isotopes in cell 1 and 24 according to the cell numeration indicated in Figure 4.3, as well as averaged over the whole assemblies. To provide accurate results a sufficient number of burnup steps were provided, with a particular attention during the burnout of gadolinium absorber. For further informations see [Kalugin et al. 2002, Appendix A]

Several solutions of the benchmark are available in literature, each of one using different methods and combinations of nuclear data libraries [Kalugin et al. 2002,Petrov, Todorova, and Kolev 2013,Thilagam 2009]. Three of the solutions have been obtained by means of Monte-Carlo methods, while the remaining ones are based on collision probability (or similar) methodologies.

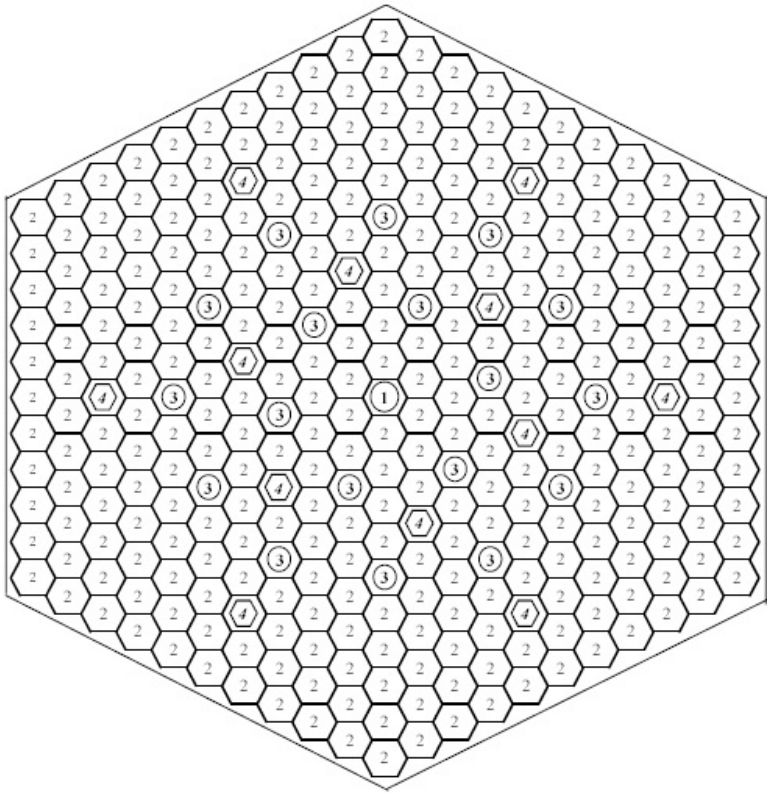

Figure 4.1: UGD assembly configuration.

Cell types:
1- Central tube;
2- Fuel cell (with U1);
3- Guide tube;
4- Fuel cell (with GD1).

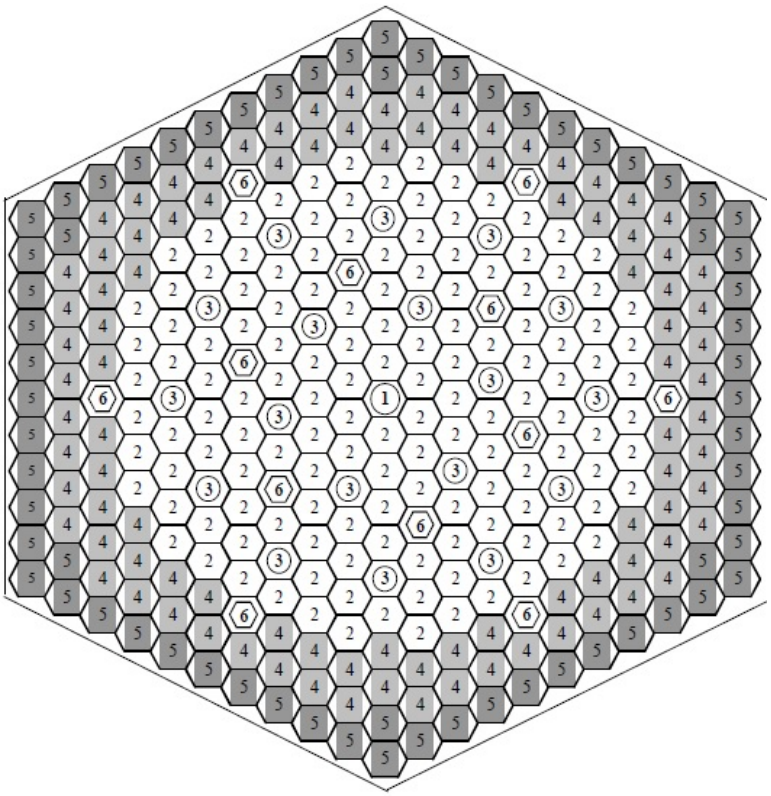

Figure 4.2: MOXGD assembly configuration.

Cell types:
1- Central tube;
2- Fuel cell (with PU3);
3- Guide tube;
4- Fuel cell (with PU2);
5- Fuel cell (with PU1);
6- Fuel cell (with GD1).

Table 4.1: Reactor state parameters

State	Description	Fuel temp. [K]	Non-fuel temp. [K]	Moderator type	^{135}Xe ^{149}Sm
S1	Operating pois.	1027	575	MOD1	Eq.
S2	Oper. non-pois.	1027	575	MOD1	0.0
S3	Hot state	575	575	MOD1	0.0
S4	Hot state w/o B	575	575	MOD2	0.0
S5	Cold state	300	300	MOD3	0.0

4.2 Codes, data and methods

The deterministic calculations presented in this work have been performed with the lattice physics capabilities of the SCALE 6.1 code system. In particular the TRITON sequence has been used, that couples the discrete-ordinates code NEWT (New ESC-based Weighting Transport code) to the depletion code ORIGEN. Cross-section self-shielding is carried out by the BONAMI and CENTRM solvers in the unresolved and resolved resonance regions respectively. The CENTRM module performs transport calculation using data on an ultrafine energy grid to generate effectively continuous energy neutron flux solutions in the resonance and thermal ranges. This is used to weight the multi-group cross-sections to be used in the subsequent transport calculations which are performed with the NEWT code.

NEWT's solution grid is based on arbitrary polygons. The curved surfaces of a cylinder are approximated as an N-sided regular polygon. By default, N=12 is used. The adopted order of S_n level symmetric quadrature set is 6. Both spatial and eigenvalue convergence criteria have been set to $1 \cdot 10^{-3}$. In our analysis the 238 energy groups structure implemented in the SCALE system has been used and a TRITON model of the hexagonal fuel assemblies described by the benchmark specifications have been built.

All the Monte Carlo calculations have been performed using the version 2.1 of the SERPENT code and results have been obtained by simulating $4 \cdot 10^7$ neutrons distributed over 400 cycles and by skipping the first 100 cycles. The correspondent statistical errors are in the order of $8 \cdot 10^{-5}$ and $2 \cdot 10^{-3}$ for k-inf and pin power respectively. The Shannon entropy criterion has also been applied for the correct convergence of the fission source.

As far as the burnup calculations are concerned, in both SCALE and SERPENT the fuel has been depleted at a constant power density of 108 MW/m^3 and a 20 depletion steps over the irradiation time have been considered, this consisting in fifteen steps of 1 MWd/kgHM up to 15 MWd/kgHM followed by five steps of 5 MWd/kgHM up to 40 MWd/kgHM. The predictor-corrector algorithm has been used for the solution of the Bateman equations. Furthermore, in order to account for the spatial and mutual self-shielding

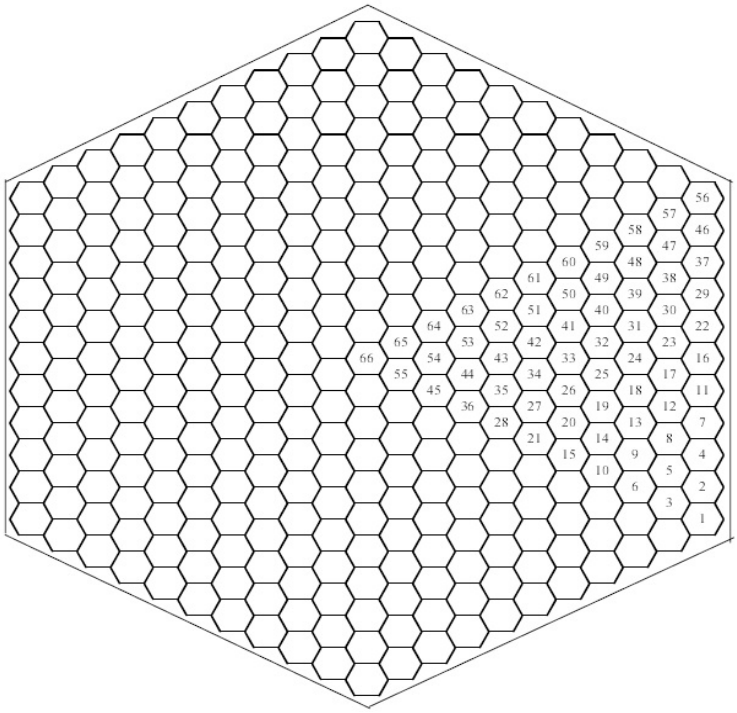

Figure 4.3: Cell numeration

effect of the main gadolinium isotopes the fuel pins containing gadolinium have been divided into ten annular sub-regions of equal area.

In our study different NDLs have also been used. While the SCALE and SERPENT solutions have been compared using the ENDF/B-VII library [Chadwick et al. 2006], SERPENT calculations have also been performed with JEFF2.2 [The JEFF2.2 Nuclear Data Library 2000] and JEFF3.1 [The JEFF3.1 Nuclear Data Library 2006] data in order to assess the consistency of our models with previously obtained solutions.

4.3 Results

4.3.1 Reference states

The SERPENT solutions for k-inf in the states S2-S5 obtained with JEFF2.2 data are provided in Table 4.2. This comparison allows to assess the validity of our model with respect to the reference MCNP4B solutions [Kalugin et al. 2002]. An overall good and consistent agreement between the two codes for all the calculated states can be observed. The small deviations on the computed reactivities are mainly due to the different data library used by MCNP4B for the ^{16}O, ^{152}Gd, ^{nat}Zr and ^{1}H isotopes and also partially to the different statistics adopted in the two codes.

Table 4.2: SERPENT and MCNP4B results for kinf at zero burnup with JEFF2.2 data

LEU	SERPENT (S)	MCNP4B (M)	Δk (M-S)$\cdot 10^{-5}$
S2	1.17987 ± 8.9E-05	1.1800 ± 6E-05	13
S3	1.19365 ± 8.6E-05	1.1925 ± 6E-05	-115
S4	1.25387 ± 8.5E-05	1.2531 ± 7E-05	-77
S5	1.32394 ± 7.6E-05	1.3235 ± 6E-05	-44
MOX	SERPENT (S)	MCNP4B (M)	Δk (M-S)$\cdot 10^{-5}$
S2	1.19258 ± 8.6E-05	1.1922 ± 7E-05	-38
S3	1.20919 ± 8.4E-05	1.2091 ± 6E-05	-9
S4	1.24408 ± 8.5E-05	1.2430 ± 6E-05	-108
S5	1.32487 ± 7.6E-05	1.3256 ± 7E-05	73

In Table 4.3 the new SERPENT reference solutions for k-inf obtained with JEFF3.1 and ENDF/B-VII nuclear data are presented together with the SCALE results obtained with ENDF/B-VII data.

When comparing the reactivity values computed with the SERPENT code and JEFF libraries, a systematic under-prediction when using JEFF3.1 with respect to JEFF2.2 can be outlined for the LEU assemblies. For the MOX assembly, however, the JEFF3.1 yields larger values than JEFF2.2. Furthermore, the k-inf computed with the ENDF/B-VII library are larger by 100-200 pcm with respect to ones evaluated with the JEFF3.1 library. All these highlighted trends are consistent with the expected values as given in literature [The JEFF3.1 Nuclear Data Library 2006, Mahlers 2009]. Moreover, when comparing reactivity values for states S2-S5 computed with SERPENT and SCALE with the ENDF/B-VII nuclear data library one can observe a systematic overestimation of the SERPENT results in the order of 400 - 500 pcm. This difference is due to the multi-group approximation used in the deterministic simulations with SCALE.

4.3.2 Reactivity effects

By definition of the operational states to be calculated within the benchmark exercise (Table 4.1), the reactivity values corresponding to these states allow for the estimation and comparison of some reactivity coefficients related to the two fuel assemblies. In particular, the differences in k-inf for the cases (S2-S1), (S2-S3), (S3-S4) and (S4-S5) provide information about the poisons (Xe and Sm) effects, the fuel Doppler coefficient, the boron effect and the moderator temperature coefficient respectively. As requested by the

Table 4.3: SERPENT and SCALE results for k-inf at zero-burnup with different data library

LEU	SERPENT(SJ) [JEFF3.1]	SERPENT(SE) [ENDF/B-VII]	Δk (SE-SJ)$\cdot 10^{-5}$
S2	1.17399 ± 8.9E-05	1.17587 ± 8.8E-05	188
S3	1.18787 ± 8.7E-05	1.18996 ± 8.6E-05	209
S4	1.24808 ± 8.5E-05	1.24993 ± 8.7E-05	185
S5	1.32088 ± 7.6E-05	1.32305 ± 7.7E-05	217
MOX	SERPENT(SJ) [JEFF3.1]	SERPENT(SE) [ENDF/B-VII]	Δk (SE-SJ)$\cdot 10^{-5}$
S2	1.19596 ± 8.5E-05	1.19762 ± 8.6E-05	166
S3	1.21259 ± 8.4E-05	1.21419 ± 8.4E-05	160
S4	1.24765 ± 8.4E-05	1.24923 ± 8.4E-05	158
S5	1.32908 ± 7.6E-05	1.33013 ± 7.6E-05	105
LEU	SERPENT(SE) [ENDF/B-VII]	SCALE(SCE) [ENDF/B-VII]	Δk (SE-SCE)$\cdot 10^{-5}$
S2	1.17587 ± 8.8E-05	1.17068	519
S3	1.18996 ± 8.6E-05	1.18557	439
S4	1.24993 ± 8.7E-05	1.24538	455
S5	1.32305 ± 7.7E-05	1.31770	535
MOX	SERPENT(SE) [ENDF/B-VII]	SCALE(SCE) [ENDF/B-VII]	Δk (SE-SCE)$\cdot 10^{-5}$
S2	1.19762 ± 8.6E-05	1.19178	584
S3	1.21419 ± 8.4E-05	1.21005	414
S4	1.24923 ± 8.4E-05	1.24491	432
S5	1.33013 ± 7.6E-05	1.32652	361

benchmark specifications, these reactivity effects have been computed for the LEU and MOX assemblies at 0 MWD/kgHM, 20 MWD/kgHM and 40 MWD/kgHM using the isotopic compositions from the burnup calculations of state S1.

To accurately perform this evaluation, each single pin in the model have to be treated separately in order to properly consider the actual value of the fuel compositions depending on the actual flux level in each pins. In our work, we have only considered the detailed pin-by-pin model in the SERPENT evaluations and consequently only these results for the reactivity effects at the different burnup branches are provided. The results are summarized in Tables 4.4 and 4.5.

As far as the poison effects are concerned, since in the SERPENT code

Table 4.4: LEU – Reactivity effects, $100 \cdot (k_{init.} - k_{fin.})$

Initial state	Final state	Burnup (MWd/kgHM)	SERPENT	SCALE	Benchmark mean
S1	S2	0	-3.58	-	-4.03
		20	-2.91	-	-3.96
		40	-2.37	-	-3.29
S3	S4	0	-6.00	-5.98	-5.99
		20	-5.40	-	-5.48
		40	-4.81	-	-4.91
S2	S3	0	-1.41	-1.48	-1.36
		20	-1.48	-	-1.52
		40	-1.35	-	-1.40
S4	S5	0	-7.28	-6.98	-6.90
		20	-6.87	-	-6.72
		40	-4.35	-	-5.33

it is not possible to impose the equilibrium of samarium at beginning of irradiation, only the xenon effect has been considered in our analysis. The effect on the system reactivity due to ^{135}Xe was found to be lower in the case of MOX fuel due to its harder neutron spectrum with respect to the LEU fuel. The calculated difference in k-inf between S2 and S1 are $\sim 358pcm$ and $\sim 263pcm$ in the case of LEU and MOX respectively. The soluble boron effect has been evaluated for a boron change of 600 ppm between the isothermal reactor states S3 and S4. As expected, also in this case because of the harder spectrum, the boron worth is reduced in the MOX assembly with respect to the LEU assembly. The difference is $\sim 71\%$ at the beginning of life and decreases with the burnup, being $\sim 24\%$ at the end of the depletion steps.

The Doppler coefficient has been estimated for a fuel temperature change from $575K$ to $1027K$. It was found to be slightly larger in the case of MOX fuel at beginning of irradiation; however, as plutonium is bred in it, the UO_2 fuel experiences a decrease of its Doppler coefficient which becomes almost equal to the one of MOX already at 20 MWd/kgHM. The isothermal effect on reactivity has been evaluated for a moderator temperature change from $575K$ to $300K$ and was found to be more negative in the case of MOX fuel. These more negative fuel and moderator temperature coefficients are of concern in accident scenarios characterized by an overcooling of the core because MOX fuel would result in a larger increase in reactivity with respect to standard LEU fuel.

From Tables 4.4 and 4.5 one can also observe a general good agreement between our SERPENT solutions and the average of the benchmark solutions

Table 4.5: MOX – Reactivity effects, $100 \cdot (k_{init.} - k_{fin.})$

Initial state	Final state	Burnup (MWd/kgHM)	SERPENT	SCALE	Benchmark mean
S1	S2	0	-2.63	-	-3.33
		20	-2.44	-	-3.44
		40	-2.16	-	-3.08
S3	S4	0	-3.50	-3.49	-3.46
		20	-3.76	-	-3.83
		40	-3.86	-	-3.98
S2	S3	0	-1.66	-1.83	-1.74
		20	-1.48	-	-1.55
		40	-1.33	-	-1.40
S4	S5	0	-8.09	-8.16	-7.93
		20	-6.98	-	-7.03
		40	-5.49	-	-5.41

available in literature.

The SCALE values are missing in the first row of both tables due to the impossibility to model the Xe equilibrium at 0 MWd/kgHM (state S1).

4.3.3 Burnup

The variation of the infinite multiplication factor in state S1 during the burnup for the LEU and the MOX assemblies is provided in Figure 4.4. The reactivity decrease was found to be slower in the MOX case. Furthermore, because of the neutron spectrum differences, different shapes in the reactivity swings can be observed. While for the LEU assembly the burning of gadolinium leads to a slightly increase of reactivity until it burns out, in the MOX assembly the gadolinium isotopes burn slower. Consequently the reactivity does not increase, but rather decreases slowly with burnup up to the point at which the burnable absorber is nearly depleted (at $\sim$ 12 MWd/kgHM) and after that it linearly decreases faster up to 40 MWd/kgHM.

The comparison of the SCALE and SERPENT burnup calculations indicates that SERPENT computed reactivities are generally and systematically higher with respect to the ones obtained with SCALE. The agreement between the two codes to predict kinf values stands within 0.39% and 0.33% over the 40 MWd/kgHM depletion for the LEU and MOX cases respectively.

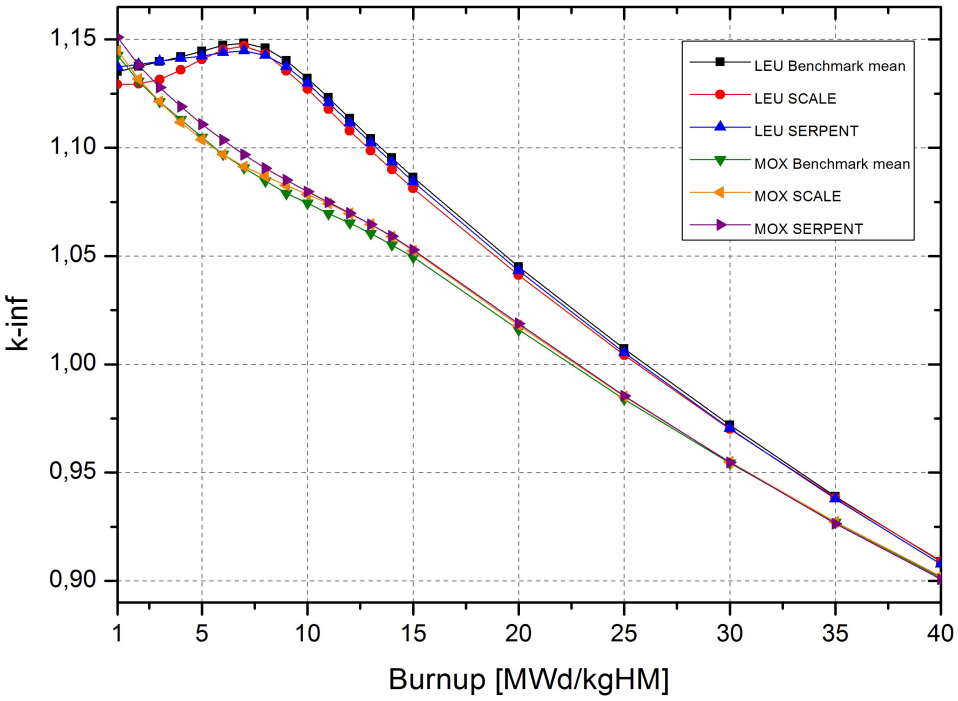

Figure 4.4: Variation of k-inf with burnup for the LEU and MOX FAs

4.3.4 Nuclide concentrations

Assembly averaged isotopic compositions versus burnup as well as isotopic compositions in the corner cell 1 and fuel gadolinium cell 24 (see Figure 4.3) for the LEU and MOX variants are presented in Figures 4.5-4.10 A generally good agreement over the entire irradiation period between our solutions and the benchmark mean values can be outlined for the nuclides ^{235}U, ^{236}U, ^{238}U, ^{239}Pu, ^{240}Pu, ^{241}Pu, ^{242}Pu, ^{155}Gd, ^{157}Gd, ^{149}Sm and ^{135}Xe. For the uranium isotopes the agreement is excellent, however some slight discrepancies that are increasing with the burnup can be observed for the plutonium isotopes, particularly in the case of ^{241}Pu build-up.

As far as the fission product poisons are concerned, while for the ^{135}Xe the SERPENT and SCALE solutions are close to each other and they are systematically slightly underestimating the benchmark mean values, in the case of ^{149}Sm the SERPENT values are closer to the mean ones but systematically higher with respect to the SCALE results. The SERPENT results seem to reproduce also better the mean solutions for the gadolinium isotopes with respect to the SCALE results, particularly for the LEU case.

In Tables 4.6 and 4.7 the deviations of the SERPENT calculated isotopic compositions with respect to the ones obtained with the SCALE code at given burnup steps for the cells 1 and 24 are provided. The very large

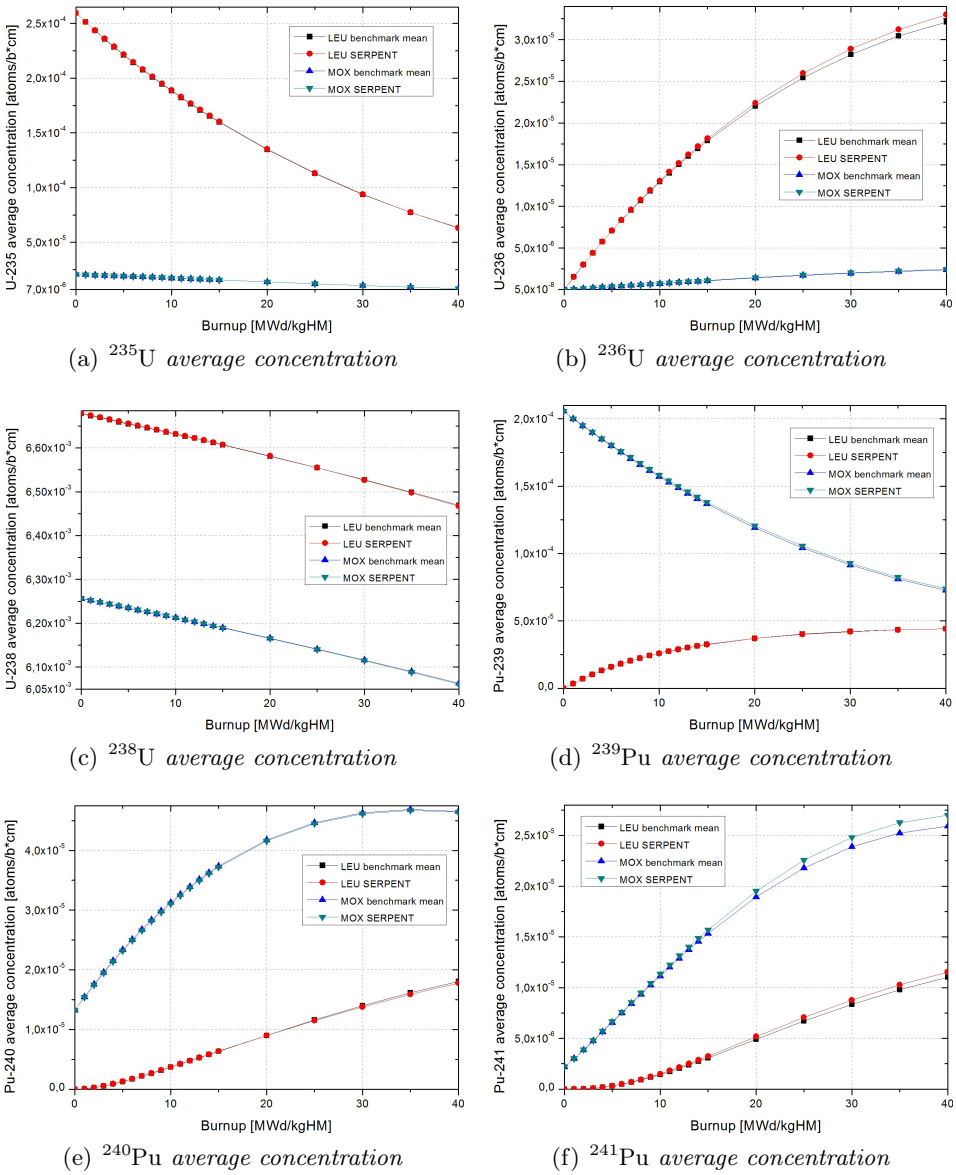

(a) ^{235}U *average concentration*

(b) ^{236}U *average concentration*

(c) ^{238}U *average concentration*

(d) ^{239}Pu *average concentration*

(e) ^{240}Pu *average concentration*

(f) ^{241}Pu *average concentration*

Figure 4.5: Assembly averaged isotopic compositions versus burnup

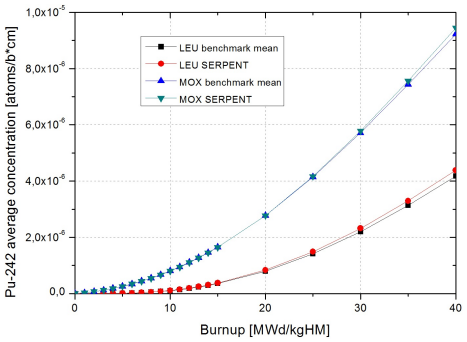

(a) ^{242}Pu *average concentration*

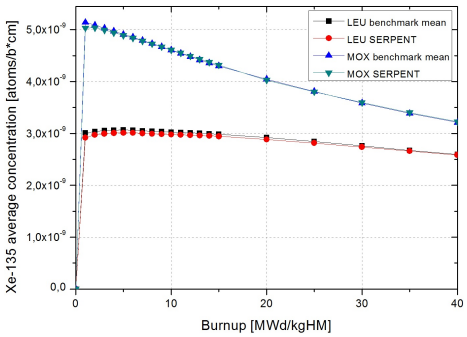

(b) ^{135}Xe *average concentration*

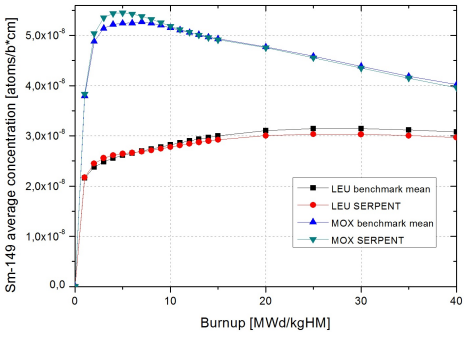

(c) ^{149}Sm *average concentration*

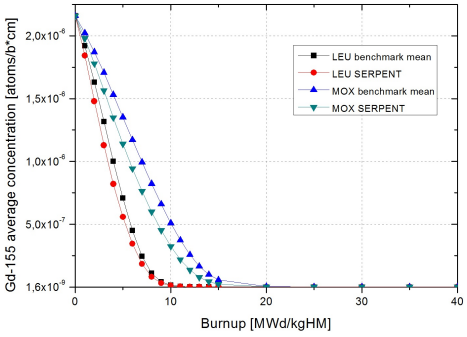

(d) ^{155}Gd *average concentration*

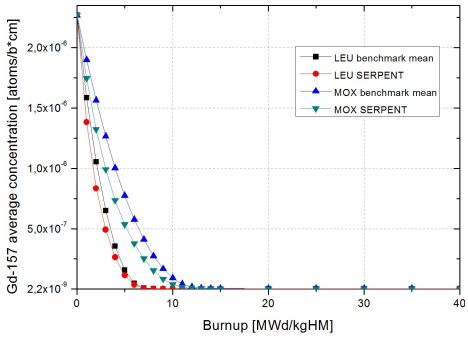

(e) ^{157}Gd *average concentration*

Figure 4.6: Assembly averaged isotopic compositions versus burnup (cont'd)

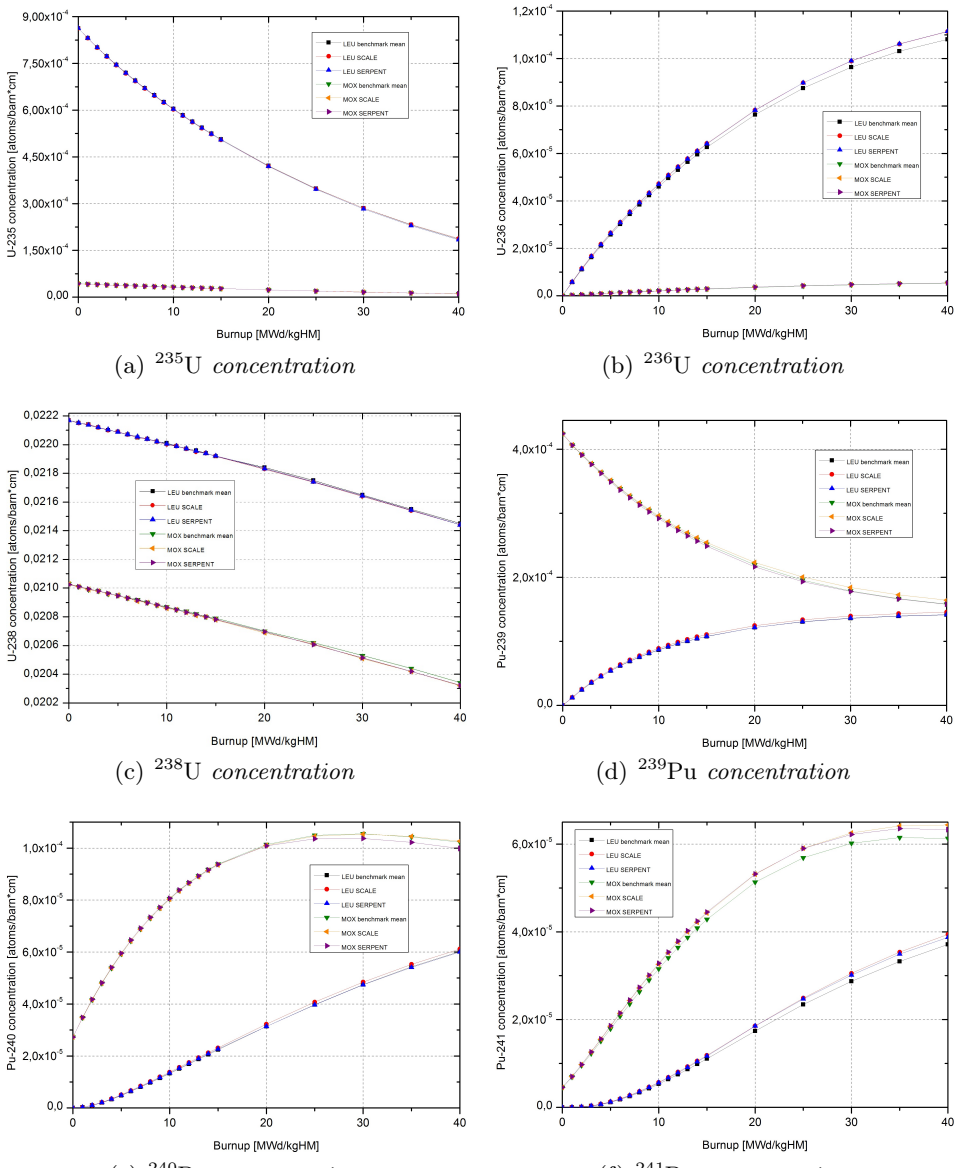

(a) ^{235}U *concentration* (b) ^{236}U *concentration*

(c) ^{238}U *concentration* (d) ^{239}Pu *concentration*

(e) ^{240}Pu *concentration* (f) ^{241}Pu *concentration*

Figure 4.7: Isotopic compositions versus burnup in the corner cell 1

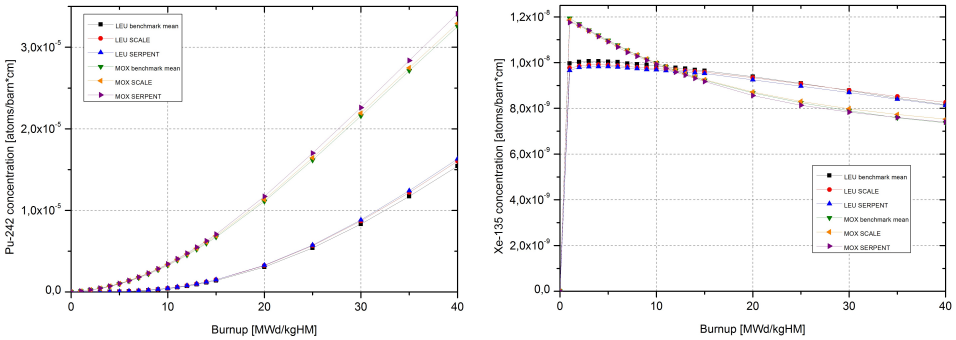

(a) ^{242}Pu *concentration* (b) ^{135}Xe *concentration*

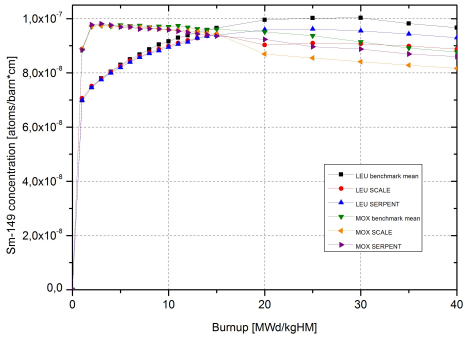

(c) ^{149}Sm *concentration*

Figure 4.8: Isotopic compositions versus burnup in the corner cell 1 (cont'd)

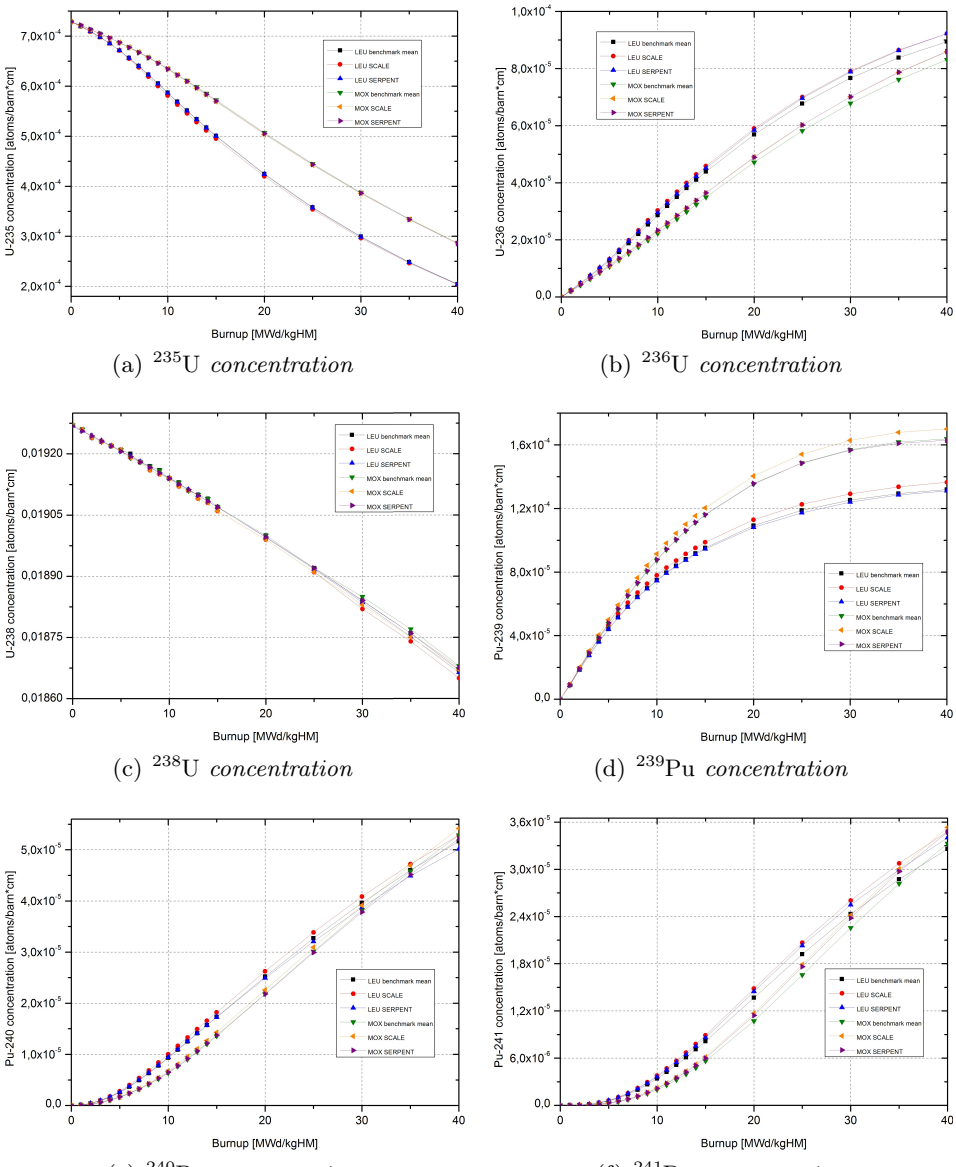

(a) ^{235}U *concentration* (b) ^{236}U *concentration*

(c) ^{238}U *concentration* (d) ^{239}Pu *concentration*

(e) ^{240}Pu *concentration* (f) ^{241}Pu *concentration*

Figure 4.9: Isotopic compositions versus burnup in the fuel Gd cell 24

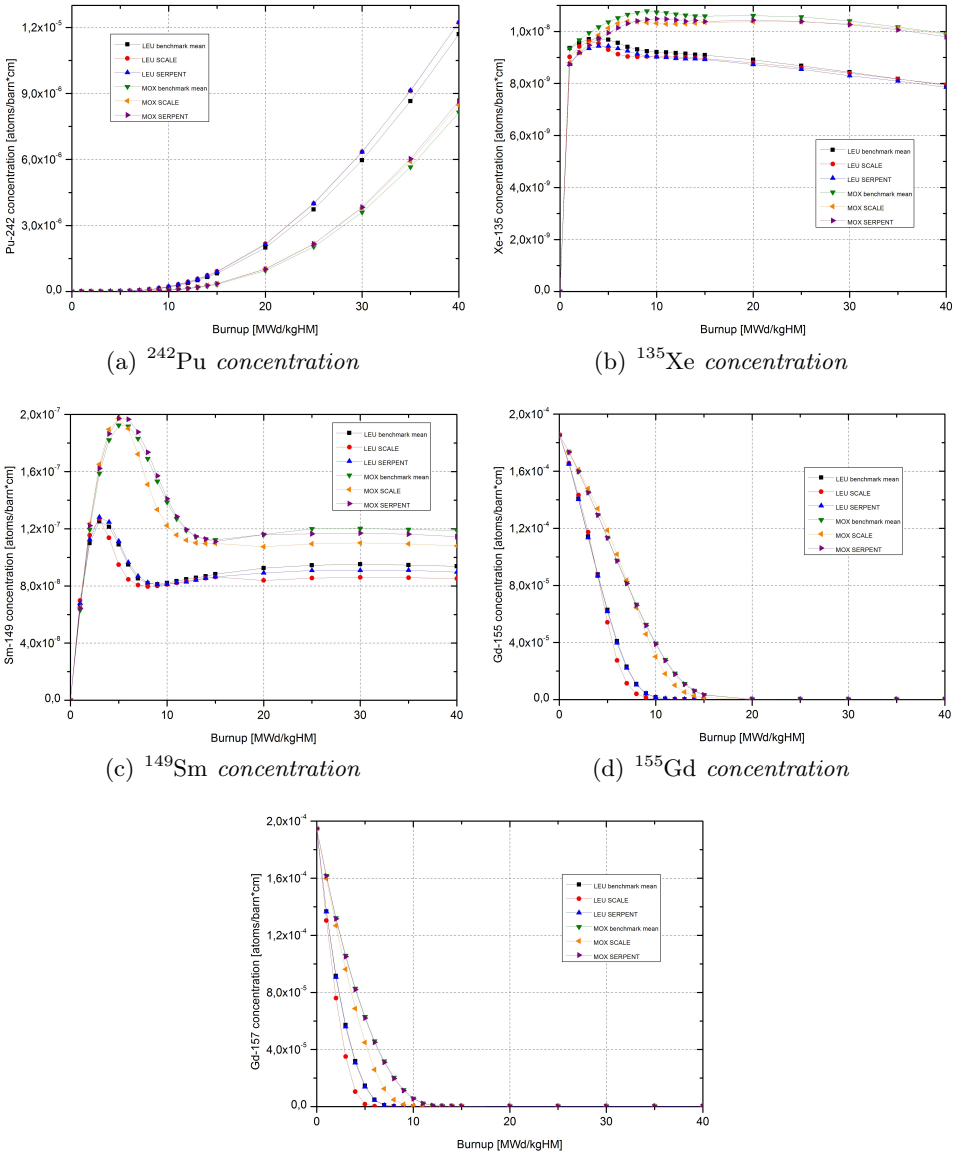

(a) ^{242}Pu *concentration*

(b) ^{135}Xe *concentration*

(c) ^{149}Sm *concentration*

(d) ^{155}Gd *concentration*

(e) ^{157}Gd *concentration*

Figure 4.10: Isotopic compositions versus burnup in the fuel Gd cell 24 (cont'd)

discrepancies for the ^{155}Gd and ^{157}Gd at 10 MWd/kgHM can be explained by the numerical errors of the predictor corrector algorithms when dealing with very low concentration levels of such isotopes at a depletion level close to burn out. Furthermore, since previous studies [Mahlers 2009,Pusa and Leppänen 2010] have underlined the good performance of the SERPENT burnup calculation models in such "extreme" conditions, one can probably consider the SERPENT solutions for gadolinium the more accurate ones.

Table 4.6: LEU Assembly - Deviations (%) between SCALE and SERPENT calculated isotopic compositions: (SCALE–SERPENT)/(SCALE)

	Burnup steps [MWd/kgHM]							
Nuclide	10		20		30		40	
Cell no.	1	24	1	24	1	24	1	24
^{235}U	-0.10	-0.84	0.22	-1.04	0.89	-0.76	2.19	-0.26
^{236}U	0.40	2.35	0.13	1.02	-0.05	0.38	-0.05	0.02
^{238}U	-0.03	0.00	-0.01	-0.03	-0.02	-0.09	0.00	-0.08
^{239}Pu	2.41	4.33	2.43	4.27	2.37	4.07	2.71	4.00
^{240}Pu	2.19	6.10	2.73	5.13	2.13	5.30	1.89	5.15
^{241}Pu	1.77	3.90	0.12	2.42	1.33	2.10	1.71	2.22
^{242}Pu	1.49	4.65	-0.81	1.67	-1.39	0.15	-1.69	-0.05
^{135}Xe	0.58	0.16	1.07	0.75	1.15	1.16	1.65	1.24
^{149}Sm	0.52	-0.26	-6.28	-6.29	-5.26	-5.67	-4.71	-5.31
^{155}Gd	-	-198.27	-	-1.82	-	-0.97	-	-0.69
^{157}Gd	-	-10.29	-	-5.95	-	-4.72	-	-5.88

4.3.5 Pin power distributions

The computed pin-by-pin fission rates with the SCALE and SERPENT codes normalized on the average values are presented in Figures 4.11,4.12 and 4.13 and the results of the inter comparison between the two codes are given in Table 4.8. A systematic slight over prediction of the SERPENT (SE) fission rates with respect to SCALE (SC) can be outlined, with the exception of the values at beginning of irradiation. Furthermore, the deviation between the two codes are higher for the MOX case. As far as it concerns the comparison of our solutions with the mean of the solutions available in literature, the maximum deviation on the pin-by-pin fission rates was found to be -4.2% (pin 35) and -1.6% (pin 63) in the case of SCALE and SERPENT respectively.

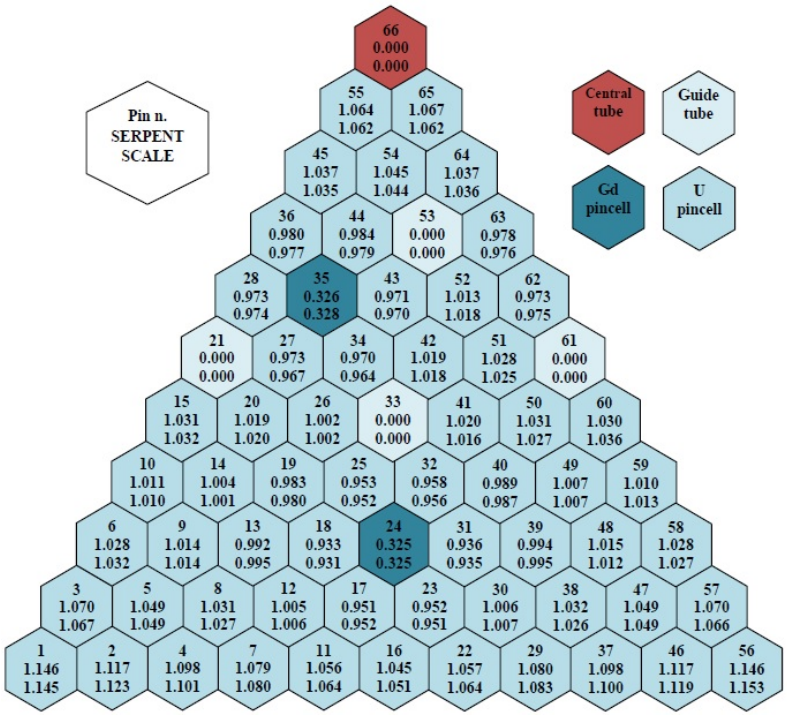

(a) *LEU at 0 MWd/kgHM*

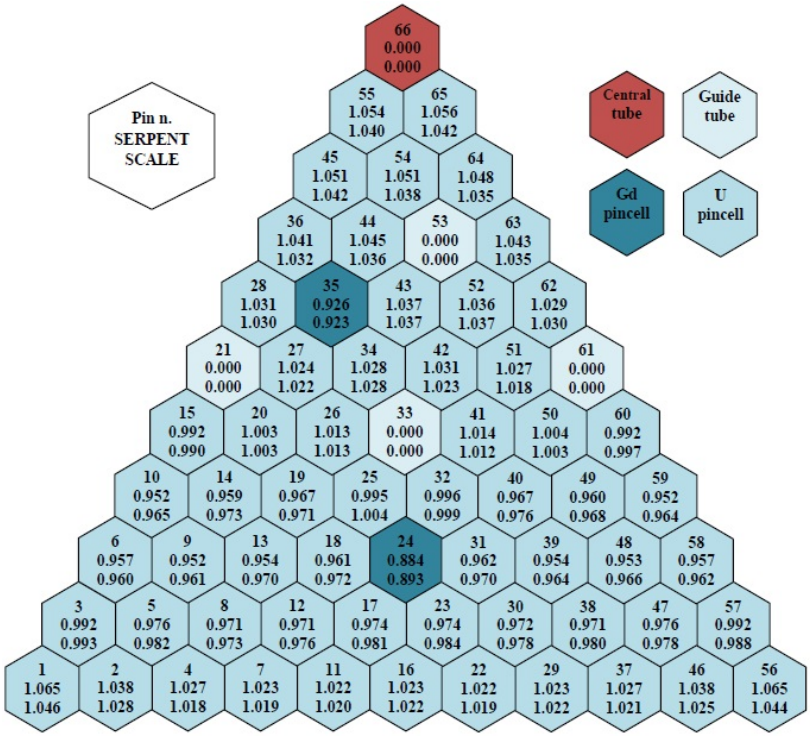

(b) *LEU at 20 MWd/kgHM*

Figure 4.11: Fission rate distributions

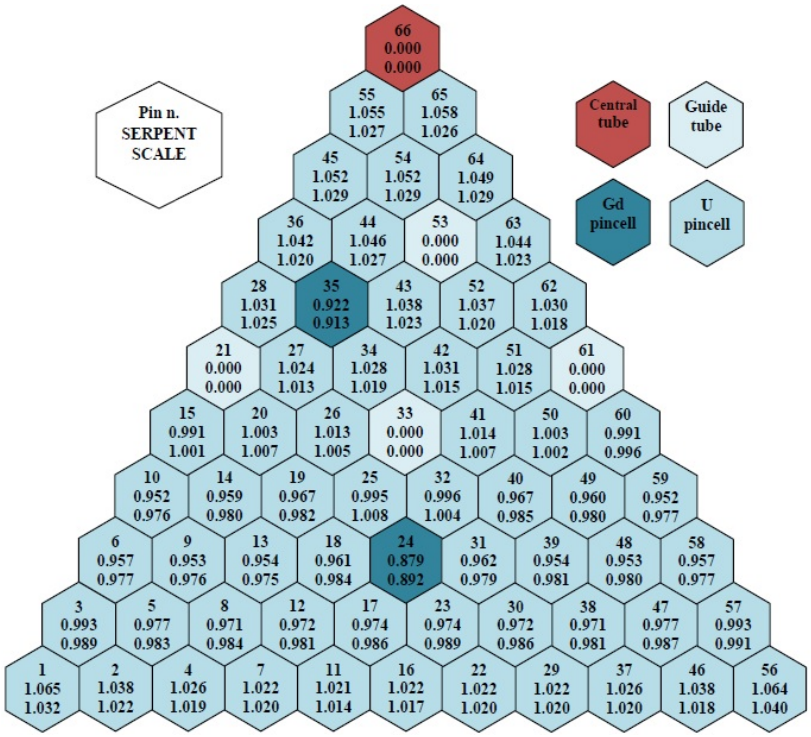

(a) *LEU at 40 MWd/kgHM*

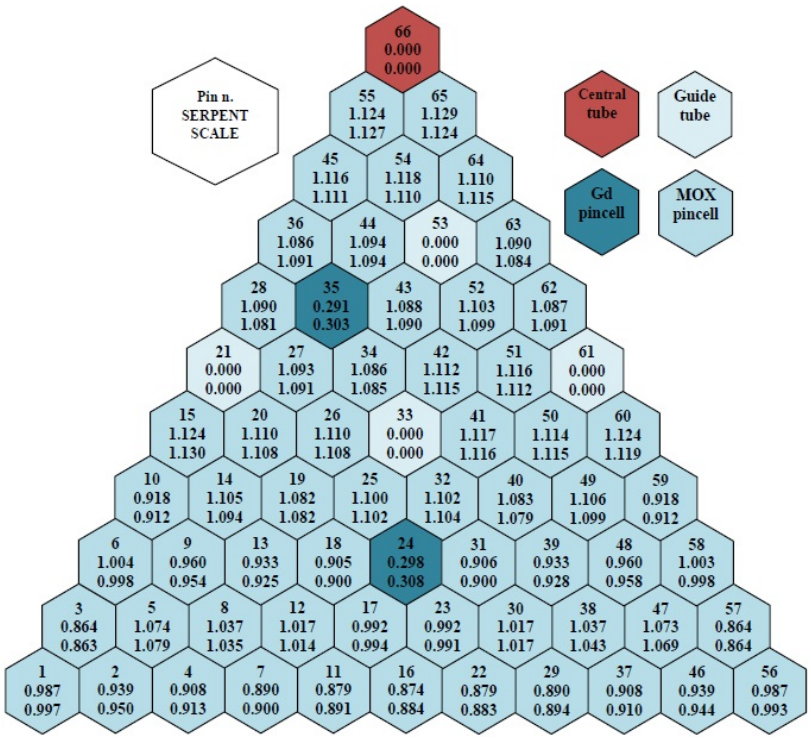

(b) *MOX at 0 MWd/kgHM*

Figure 4.12: Fission rate distributions

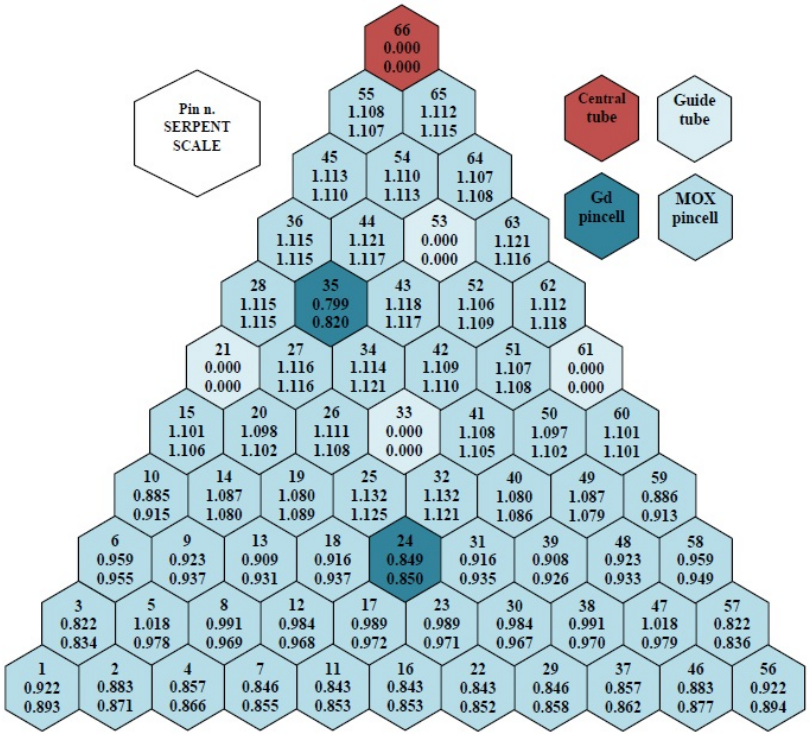

(a) *MOX at 20 MWd/kgHM*

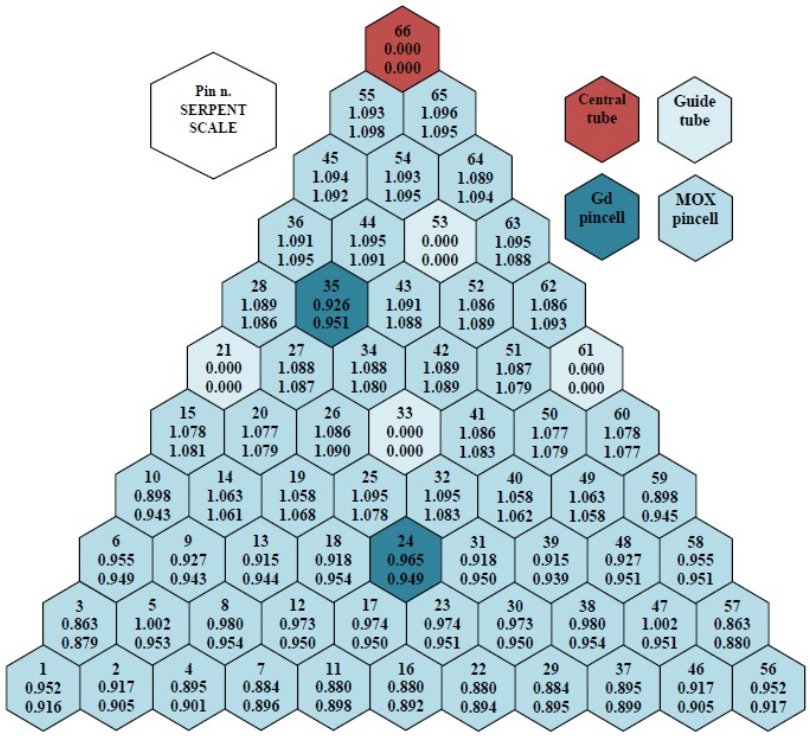

(b) *MOX at 40 MWd/kgHM*

Figure 4.13: Fission rate distributions

Table 4.7: MOX Assembly - Deviations (%) between SCALE and SERPENT calculated isotopic compositions: (SCALE–SERPENT)/(SCALE)

Nuclide	Burnup steps [MWd/kgHM]							
	10		20		30		40	
Cell no.	1	24	1	24	1	24	1	24
^{235}U	0.14	0.12	0.80	-0.37	1.83	-0.13	3.36	0.41
^{236}U	0.12	-1.13	-0.29	0.23	-0.09	-0.03	0.13	-0.03
^{238}U	-0.03	0.00	-0.03	-0.03	-0.02	-0.06	-0.01	-0.03
^{239}Pu	1.43	3.94	3.05	3.33	3.48	3.81	3.94	4.16
^{240}Pu	-0.35	3.31	0.20	3.50	1.58	3.34	2.76	3.65
^{241}Pu	-0.61	2.04	-0.09	2.32	0.56	1.45	1.68	1.70
^{242}Pu	-2.01	-2.49	-3.33	1.19	-3.16	-0.86	-3.58	-2.12
^{135}Xe	0.49	-1.71	1.73	-0.65	1.87	0.26	1.72	1.04
^{149}Sm	0.17	-15.43	-6.19	-7.96	-5.53	-6.24	-5.38	-6.06
^{155}Gd	-	-29.32	-	-30.94	-	-0.65	-	0.16
^{157}Gd	-	-750.55	-	-9.70	-	-4.60	-	-5.72

4.4 Comparison between different depletion algorithms

Two different depletion algorithms have been tested with the SERPENT code: the Predictor-corrector (see 3.7.1) and the Stochastic Implicit Euler (see 3.8.4). The differences between these two algorithms may be seen in Figure 4.14. In this figure the two algorithms are compared with the mean solution of the six participants to the benchmark.

In predicting the k-inf of the LEU fuel assembly, the Stochastic Implicit Euler algorithm greatly overestimates (up to ~ 1800 pcm) the results of both Predictor-corrector and benchmark participants in the first 8 MWd/kgHM, while after that point its prediction is in good agreement with the other two, even if a slightly underprediction ($\sim 200 - 300$ pcm) can be observed at the end of the depletion period (from 25 to 40 MWd/kgHM).

In the MOX fuel assembly the opposite situation occurs. In fact, the SIE algorithm have good performances in the first steps with a maximum difference of 292 pcm at 9 MWd/kgHM, while it starts to underestimate the value of k-inf after 20 MWd/kgHM (686 pcm) and until the end of the depletion steps (1278 pcm).

4.5 Effects of the substeps and mesh refinements

The first steps of the 20 depletion steps over the irradiation time (fifteen steps of 1 MWd/kgHM up to 15 MWd/kgHM followed by five steps of 5

Table 4.8: Comparison of pin-by-pin fission rates computed by SCALE (SC) and SERPENT (S)

LEU Assembly	Burnup [MWd/kgHM]		
	0	20	40
Max δ [%] (SC-SE)	-0.78	2.14	3.22
Average δ [%] (SC-SE)	0.25	0.69	1.45
Pin number	21	55	1
MOX Assembly	Burnup [MWd/kgHM]		
	0	20	40
Max δ [%] (SC-SE)	-1.26	3.97	5.04
Average δ [%] (SC-SE)	0.48	1.08	1.44
Pin number	10	4	46

MWd/kgHM up to 40 MWd/kgHM) have been further subdivided because of some concerns about the gadolinium burnout. In fact the huge absorption cross-sections of ^{155}Gd and ^{157}Gd cause strong spatial shielding effects in gadolinium bearing pins. This effect often requires the use of smaller depletion steps (up to a factor of 10) to avoid errors in the predicted value of the k-inf. Table 4.9, taken from Lee, Rhodes, and Smith 2013, shows this effect for the GE14 10x10 BWR fuel assembly.

Table 4.9: Impact of Gd Pins on Accuracy of GE14 Assembly Burnup Calculation (18.0 MWd/kgU)

	No Gd		17 Gd Pins	
Step size [MWd/kgU]	k-inf	Difference [pcm]	k-inf	Difference [pcm]
0.0625	1.200939	-	1.18231	-
0.125	1.200938	-1	1.18218	-9
0.25	1.200935	-3	1.18174	-41
0.5	1.200930	-6	1.18000	-166
0.0625	1.200921	-12	1.17283	-684

For this reason two types of subdivision have been tested:

- 0.5 MWd/kgHM up to 15 MWd/kgHM and then 2.5 MWd/kgHM up to 40 MWd/kgHM;
- 0.25 MWd/kgHM up to 5 MWd/kgHM and then the "normal" steps are used.

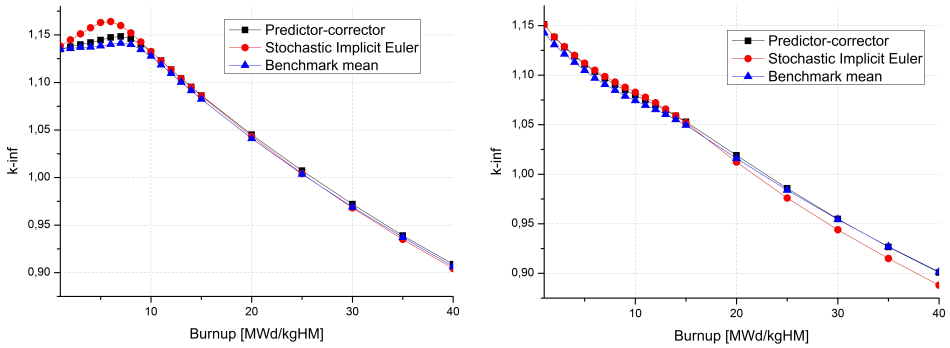

(a) *LEU fuel assembly* (b) *MOX fuel assembly*

Figure 4.14: Reactivity swings for LEU and MOX fuel assemblies with Predictor-corrector and SIE algorithms

The second discretization has been stopped to the first 5 MWd/kgHM to limit the computational time, since the negative effect of gadolinium is important only in the initial depletion steps.

Figure 4.15 shows the differences between these two discretizations and the benchmark one in the first 5 MWd/kgHM. The k-inf values with the two subdivisions are similar and maximum difference between those and the value obtained with the benchmark steps is $\sim$ 100 pcm at 5 MWd/kgHM. This error doesn't propagate in the following steps, being $\sim$ 150 pcm at 40 MWd/kgHM.

The SERPENT code adopts a mesh refinement for the fuel pins containing gadolinium which are divided into ten annular sub-regions of equal area. This idea has been tested also in the SCALE code, dividing the gadolinium pins into four annular sub-regions. The effects of this refinement has been found to be negligible, with a maximum difference of about 20 pcm.

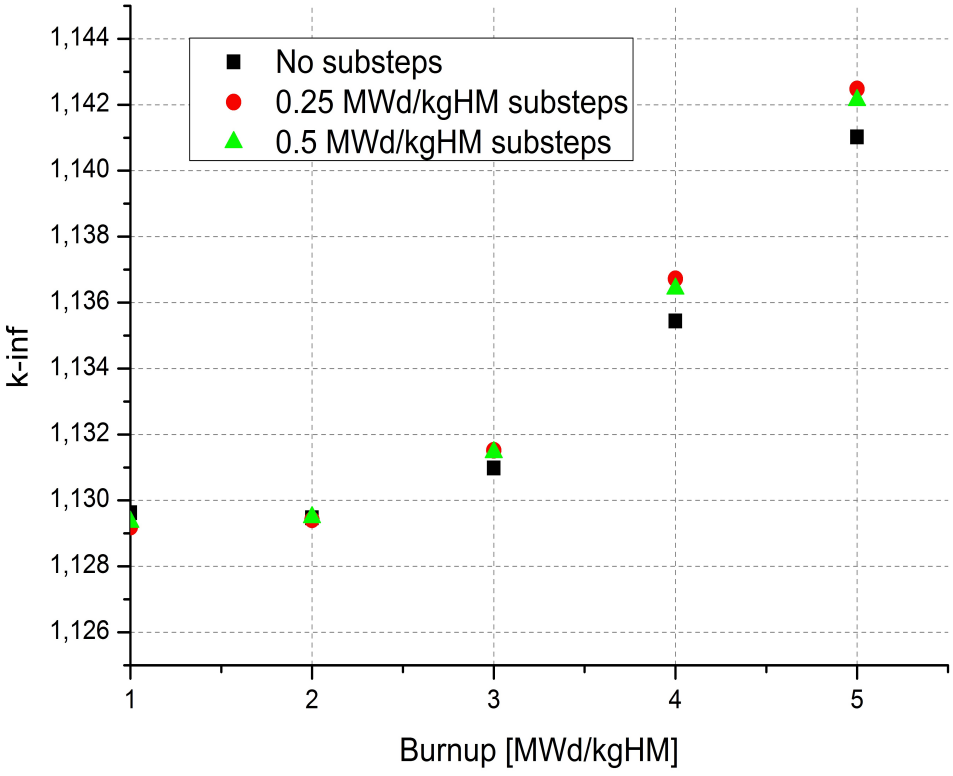

Figure 4.15: Effects of the substeps

Chapter 5

Uncertainty theory

The results of a computer code, no matter if the code simulates thermal hydraulics phenomena or reactor parameters, are subject to uncertainties. These uncertainties come from many sources, which can be divided in four groups:

- code uncertainties;
- representation uncertainties;
- plant uncertainties;
- user effect.

The code uses aprroximations to solve the equations and to represent the material properties and their changes during plant operations. The code can also have some deficiencies that affect the results. The representation uncertainties refer to the nodalization effect. An imperfect knowledge of boundary and initial conditions and the scatter of measured values are called the plant uncertainties. Finally an user effect exists. Two different users with the same code do not always achieve the same results, due to nodalization differences, to the planning of the sensitivity studies and to the interpretation of supplied information, that are often incomplete. [D'Auria 2012]

The influence of the uncertainties on the calculation has to be studied carefully. The reason for this need is to be found in the increase of the costs of nuclear power plants design, due to the use of conservative assumptions. These conservative assumptions were adopted to guarantee the safety and the correct operation of the plant. The uncertainty analysis can reduce the cost of the design, but also increase the safety level, thanks to a better knowledge of phenomena and parameters and to the possibility to establish realiable safety margins. The use of best estimate code plus uncertainty approach (BEPU) is allowed by some national rules, like the USA Code of Federal Regulation 10CFR50.46. [Glaeser 2008]

Solving the differential-integral Boltzmann equation for neutron transport requires to handle seven variables, three in space, two in angle, one in energy and the time. For this reason reactor physics calculations can be complex and it can be difficult to obtain an accurate solution. The main source of uncertainty is represented by the measurements of nuclear cross-sections. In the past the uncertainties were reduced by means of informations deriving from integral experiments. The problem was how to change the design by taking advantage on these informations. For this purpose the use of sensitivity coefficients has been mostly successfull. Sensitivity coefficients have many applications:

- uncertainty estimates;
- design optimization;
- determination of target accuracy requirements;
- adjustment of input parameters;
- evaluation of the representativity of an experiment with respect to a reference design configuration.

In uncertainty evaluation these coefficients are multiplied by the variation of the input parameter to quantify the impact on the targeted quantities. [Palmiotti and Salvatores 2012]

The uncertainty data of the input can be provided by the expert judgment of a designer or can be originated by experiments, as in the case of the neutron cross-sections. These experimental data are gathered in covariance libraries, that are put together with the nuclear data libraries. There are two main methods to assess the magnitude of uncertainties in neutronics:

- the statistical sampling method;
- the use of adjoint fluxes in the framework of the perturbation theory.

The former is used primarily when few input parameters are considered and many outputs are requested. The latter, that is the one mainly adotped in reactor physics, is good in the opposite situation, i.e. many considered input parameters and few requested outputs. Since in reactor physics calculations the uncertainties come from the cross-section libraries (several thousand of values), it's easily understood the choice of the adjoint method for this kind of problem. The adjoint method takes also advantage of the linear property of the Boltzmann equation. However the perturbation methodology is not adequate or is inefficient in some cases, that can be divided in two groups:

- cases with a large number of responses, since it would be necessary to perform adjoint transport calculations for each of them;

- cases with discontinuities or bifurcations, since the first-order perturbation method is not applicable.

There is a third case, which applies to the code SCALE and its module TSUNAMI (Tools for Sensitivity and Uncertainty Analysis Methodology Implementation): the perturbation theory cannot be used when it is required a code for which this theory has not been developed. For example, it is impossible to perform calculations with coupled neutronics and thermal hydraulics, since the generalized adjoint calculations has been implemented only in XSDRN and NEWT transport codes within SCALE. [M. Williams, Ilas, et al. 2013]

Before to briefly explain the two methods listed above, some definitions have to be introduced. One of the important consequences of quantum mechanics is the realization that in the way we describe nature an inherent uncertainty exists. The inherent uncertainty of quantum mechanics is expressed in the so-called "uncertainty principle".

Definition 1 (Heisenberg uncertainty principle)**.** It is impossible to specify, accurately and simultaneously, the values of both members of physical variable pairs that describe the behaviour of a physical system.

Two important pairs are the system momentum and its space coordinate and the system energy and the time at which it is measured. The uncertainty principle states that the product of the uncertainty in the knowledge of two such variables must be larger than Planck's constant h divided by 2π (reduced Planck's constant, $\hbar = h/2\pi = 1.054 \cdot 10^{-34} J \cdot s$). The uncertainty of a variable A is defined as :

$$\Delta A = (< A^2 > - < A >^2)^{1/2}, \tag{5.1}$$

where <A> is the expectation value of A. Systematic and statistical uncertaities have to be distinguished. The systematic uncertainty arises due to some negligence in the experiment or in the theory on which the experiment is based. The statistical uncertainty is considered to arise from the finiteness of the input data ensemble.

Definition 2 (Sensitivity)**.** A sensitivity is a measure of the effect of a given input parameter on a required response.

Usually the sensitivity is defined as the first order derivative of the response R with respect to an input parameter α_i, $\partial R/\partial \alpha_i$. For certain non-linear problems, high order sensitivities are required ($\partial^n R/\partial {\alpha_i}^n$).

It is customary to define the sensitivity in relative terms as $\partial R/\partial \alpha_i \cdot \alpha_i/R$. This definition demonstrates the meaning of the sensitivity as the measure of the importance of an input parameter. Sensitivity analysis is used in combination with uncertainty analysis to easily identify the most important input parameters.

Definition 3 (Covariance)**.** The covariance between two random variables X and Y is defined as the expected value of the product of their distances from the mean:

$$Cov(X,Y) = \mathbb{E}\big[\big(X - \mathbb{E}[X]\big)\big(Y - \mathbb{E}[Y]\big)\big]. \tag{5.2}$$

The covariance measures the propensivity of two random variables to change together. The covariance is positive if the X increases as Y increases, and is negative when to a decrease of X corresponds a increase of Y. The covariance matrix extends the concept of covariance to multiple dimensions. Its element in the (n, m) position represents the covariance between the n^{th} and m^{th} elements of a vector of random variables.

For more informations about the fundamentals about uncertainty and sensitivity calculations see [Cacuci 2003].

5.1 Perturbation theory

The perturbation theory is used in many branches of physics, such as astronomy, and, in the nuclear field, is not limited to reactor physics, since there are some applications in thermal-hydraulics and safety problems. An example of adjoint sensitivity and uncertainty analysis extended to thermal-hydraulics may be found in [Cacuci, Ionescu-Bujor, and Navon 2005]. The reactor physics version of the perturbation theory was born in the 50s, thanks to the work of Usachev. This theory was applied to the evaluation of the k-eff of the critical reactor [Usachev 1955] and makes use of the adjoint flux, a function whose physical meaning was investigated by Lewins [Lewins 1960]. Usachev also extended the theory to variations of any neutron flux functional during the 70s and the 80s. This development allowed the use of the theory also for sensitivity studies. [Usachev 1963]

The generalization to the case of linear and bilinear functions of the flux, both real and adjoint, was reached by Gandini [Gandini 1967]. During the 70s the perturbation method, developed in Europe, began to be used also in some Japanese and U.S. laboratories. Some theoretical improvements extended the theory to the nuclide concentrations and allowed the study of irradiation.

The perturbation theory is used to solve problems with small and nonuniform perturbations, like fuel burnup or poison accumulation, in the reactor core. When a perturbation is uniform throughout the entire core, the problem can be handled by other methods, performing multigroup diffusion calculations. This approach cannot be reliable for small perturbations since the effect of perturbation can be lost in the calculations due to the round-off errors. The main purpose of perturbation theory is to evaluate the changes in the multiplication factor, but also in other parameters of interest (power

distribution, changes of composition, ...) [Lamarsh 1966]. Small perturbations allow to use the first order formulation for the perturbation method, that is the most used world wide, and to neglect the second order terms.

The multiplication factor of a uniform, bare, thermal reactor is expressed as

$$k = \eta f p \varepsilon P_L = \nu \left(\frac{\Sigma_f}{\Sigma_{aF}} f p \varepsilon P_L \right), \tag{5.3}$$

where ε is the fast fission factor, p is the resonance escape probability, f is the thermal utilization factor, P_L is the non-leakage probability, η is the thermal fission factor, ν is the average number of neutrons produced per fission, Σ_{aF} is the macroscopic absorption cross section in fuel and Σ_f is the macroscopic fission cross section. If the parameters in the parentheses are denoted by g, it is possible to write $k = \nu g$. In case of criticality $\nu g = 1$.

As a result of a uniform change in the entire reactor, some of the parameters will change and the reactor will become supercritical or subcritical. Either way it will be $k' = \nu g \neq 1$ and the reactivity will be

$$\rho = \frac{k' - k}{k'} = \frac{g' - g}{g'}. \tag{5.4}$$

To restore the criticality it can be assumed to modify the value of ν in such a way that with the new value ν' the product $\nu' g'$ is again equal to one. This is obviously impossible in reality but is useful to describe the effects of the perturbation. So the reactivity of the perturbed reactor can be written as

$$\rho = -\frac{\nu' - \nu}{\nu} = -\frac{\Delta\nu}{\nu}. \tag{5.5}$$

These equations can be generalized to reactors that are not bare, thermal and homogeneous and to nonuniform perturbations. Regardless of the nature of the perturbation, an appropriate change in ν can take back the reactor to criticality and $\Delta\nu/\nu$ can be used to describe how the reactor is affected by the perturbation.

A more exhaustive and classical presentation of the perturbation theory may be found in the book by [Weinberg and Wigner 1958].

5.1.1 Adjoint flux

The notation $< \Psi, \Phi >$ indicates the scalar product of two functions Ψ and Φ, whatever the functions Φ and Ψ might be. The adjoint operator A^+ of any linear operator A is defined by the following property:

$$< \Psi, A\Phi > = < A^+\Psi, \Phi > . \tag{5.6}$$

This operation of permutation is, in neutronic, the equivalent of travelling the opposite path of true neutrons. Denoting with H the time-independent

Boltzmann operator, the "direct" flux solves the equation:

$$H\Phi = \frac{1}{v}\frac{\partial \Phi}{\partial t}. \tag{5.7}$$

In critical conditions, the equation $H\Phi = 0$ has a non-trivial solution. This solution is the eigenfunction of H associated with a zero eigenvalue. It is possible to show* that an operator and its adjoint have the same eigenvalues. Therefore the adjoint flux can be defined as the solution of

$$H^{+}\Phi^{+} = 0. \tag{5.8}$$

This mathematical definition has an interesting physical meaning, since the adjoint flux represents the neutron importance. To better understand this concept, consider a two group energy discretization in a reactor core with reflector. The thermal adjoint flux is greater than the fast one in the core, but is smaller into the reflector. This fact can be easily explained:

- in the core, the slow neutrons are adsorbed more than the fast neutrons and therefore the chain reaction has a greater contribution from the former ones;
- in the reflector, the fast neutrons have a greater probability to come back into the core after some scattering reactions, while the thermal neutrons are captured.

More generally the importance of a neutron is related to its influence on the reactor. So a neutron placed at the centre of a reactor would be more important than a neutron placed at the surface, since the former has a chance to cause fission, while the latter would probably escape. Likewise a neutron in the thermal zone of the energy spectrum is more important than a neutron near the ^{238}U capture resonance energy. [Reuss 2008] It can be useful to note that the adjoint fluxes have a reverse behaviour than the "direct" fluxes (e.g., in the two-group approximation the fast adjoint flux is less than the thermal one in the core although the fast "direct" flux is greater than the slow flux in the same region).

Another important physical interpretation of the adjoint flux is related to reactivity. It can be shown that «the group adjoint function $\psi_n(\overrightarrow{r})$ is proportional to the gain or loss in reactivity of a reactor due to the insertion or removal of one neutron per second in the group at that point $\overrightarrow{r}$» (Lamarsh 1966).

A more heuristic point of view about the adjoint flux can be found in [Gandini 2014].

*For instance a demonstration may be found in [Lamarsh 1966, chapter 15]

5.1.2 One-group perturbation theory

In this section some concepts of the perturbation theory will be discussed with the approximation of a one-group energy discretization. For a critical reactor the flux can be calculated by solving the equation

$$divDgrad\phi + (\nu\Sigma_f - \Sigma_a)\phi = 0. \tag{5.9}$$

This equation can be written also as $M\phi = 0$, where $M\cdot = divDgrad\cdot + \nu\Sigma_f\cdot - \Sigma_a\cdot$.

Consider a perturbation of the macroscopic cross-sections, that are now denoted by $\Sigma_f^{'}$ and $\Sigma_a^{'}$, with

$$\Sigma_f^{'} = \Sigma_f + \delta\Sigma_f \tag{5.10}$$

and

$$\Sigma_a^{'} = \Sigma_a + \delta\Sigma_a, \tag{5.11}$$

where $\delta\Sigma_a$ and $\delta\Sigma_f$ represent little changes of the values of the macroscopic absorption and fission cross-sections. After the perturbation the reactor is in a subcritical or supercritical condition, but it could be returned critical if a change of ν were possible, as explained in 5.1. Then the diffusion equation is:

$$divDgrad\phi^{'} + (\nu^{'}\Sigma_f^{'} - \Sigma_a^{'})\phi^{'} = M^{'}\phi^{'} = 0. \tag{5.12}$$

Inserting Eq. 5.10 and Eq. 5.11 into Eq. 5.12, writing $\nu^{'} = \nu + \Delta\nu$ and ignoring the term $\Delta\nu\delta\Sigma_f$, since the theory is applied with small perturbations, the operator $M^{'}$ becomes

$$M^{'} = M + \nu\delta\Sigma_f + \Delta\nu\Sigma_f - \delta\Sigma_a = M + P. \tag{5.13}$$

P is known as perturbation operator. The equation 5.12 becomes $(M+P)\phi^{'} = 0$.

By wisely handling the equations above[†], it is possible to get the reactivity introduced by the perturbation as:

$$\rho = \frac{\int_V (\nu\delta\Sigma_f - \delta\Sigma_a)\phi^2 dV}{\nu\int_V \Sigma_f\phi^2 dV}. \tag{5.14}$$

This equation shows that the effect of a perturbation in Σ_f or Σ_a is obtained by weighting the perturbation by the square of the flux. The quantity $\phi^2(\overrightarrow{r})$ is therefore called statistical weighting function of the point $\overrightarrow{r}$.

Until now only changes in Σ_f and/or Σ_a have been assumed. If it is considered also a perturbation of D, following a similar procedure, it can be found that changes in D are weighted by $(\nabla\phi)^2$ instead of ϕ^2.

[†]For those who are interested to the complete procedure see [Lamarsh 1966]

These formulas may be used only when and where the one-group theory gives accurate values of the flux. For example, the one-group theory cannot predict the peaking of the thermal flux in the reflector. Informations about the two-group perturbation theory and also about higher order formulas may be found in several articles and text books, for instance [Reuss 2008], [Cacuci 2003] and [Lamarsh 1966].

5.1.3 Sensitivity and perturbation theory

A generic integral parameter Q, like a reactivity coefficient or k-eff, can be represented as a function of cross-sections:

$$Q = f(\sigma_1, \sigma_2, \ldots, \sigma_J). \tag{5.15}$$

To evaluate the sensitivity coefficients in the perturbation theory, the relative variation of an integral parameter Q due to the variation of the cross-section values can be used:

$$\frac{\delta Q}{Q} = \sum_j S_j \frac{\delta \sigma_j}{\sigma_j}, \tag{5.16}$$

where S_j is the sensitivity coefficient, given by

$$S_j = \frac{\partial Q}{\partial \sigma_j} \cdot \frac{\sigma_j}{Q}. \tag{5.17}$$

The dependence of the parameter Q on the cross-sections can be divided in two parts: an explicit one, σ_i^e, and an implicit one, σ_i^{im}. From this consideration it follows:

$$\frac{\delta Q}{Q} = \sum_j S_j \frac{\delta \sigma_j^{im}}{\sigma_j^{im}} + \left(\frac{\partial Q}{\partial \sigma^e} \cdot \frac{\sigma^e}{Q} \right) \cdot \frac{\delta \sigma^e}{\sigma^e} = I + D. \tag{5.18}$$

The terms I and D represent the indirect and the direct effect. The direct effect reflects the dependence of the integral parameter Q on the energy dependent detector cross-section σ^e. Instead, the indirect effect represents the response perturbation due to flux perturbations. This last term can be subdivided into an implicit and an explicit component. The implicit component reflects the fact that the flux can be perturbated also by the change of the self-shielded cross-section of a nuclide, due to a perturbation of the cross-section of another nuclide. The explicit component is related to flux perturbations caused by the perturbation of any multi-group cross-section which appears explicitly in the transport equation. [Mercatali 2013]

It is convenient to represent the uncertainties associated to the cross-sections in the form of a variance-covariance matrix:

$$D_\sigma = \begin{bmatrix} d_{11} & d_{12} & \ldots & d_{1J} \\ d_{12} & d_{22} & \ldots & d_{2J} \\ \vdots & \vdots & \ddots & \vdots \\ d_{1J} & d_{2J} & \ldots & d_{JJ}, \end{bmatrix}$$

where the elements d_{ij} represent the variances and covariances of the nuclear data [Palmiotti and Salvatores 2012]. Using the variance-covariance matrix and the sensitivities coefficients, it is possible to calculate the variance of the generic integral parameter Q as

$$var(Q) = \sum_{j,i}^{J} S_j S_i d_{ij}. \tag{5.19}$$

5.1.4 TSUNAMI module

Sensitivity and uncertainty (S/U) analysis capabilities for criticality safety are included in SCALE. Both 1-D and 3-D sequences plus several auxiliary codes have been developed into a suite of sensitivity and uncertainty analysis codes called TSUNAMI (Tools for Sensitivity and Uncertainty Analysis Methodology Implementation). TSUNAMI contains a number of codes that were developed primarily to assess the degree of applicability of benchmark experiments for use in criticality code validations. However, the sensitivity and uncertainty data produced by these codes can be used in a wide range of studies. Sensitivity coefficients produced by the TSUNAMI sensitivity analysis sequences predict the relative changes in a system's calculated k-eff value due to changes in the neutron cross-section data. Both TSUNAMI-1D and TSUNAMI-3D fold the sensitivity data with cross-section covariance data to calculate the uncertainty in the calculated k-eff value due to tabulated uncertainties in the cross-section data. The applicability of benchmark experiments to the criticality safety validation of a given application can be assessed using S/U-based integral indices. The TSUNAMI-IP (Indices and Parameters) code utilizes sensitivity data and cross-section covariance data to produce a number of relational integral indices that can be used to assess system similarity.

SCALE is equipped with a library of nuclear data covariance. This library has been created by means of the covariances from ENDF/B and JENDL libraries [M. Williams and Rearden 2008]. These data are combined with the response sensitivity coefficients, calculated by SCALE using the first-order perturbation theory. For this methodology an adjoint transport calculation is necessary for each desired response. When all the adjoint and forward calculations have been done, the sensitivity coefficients can be very efficiently calculated for each input parameter. These parameters include also the material concentrations and the nuclear data [M. Williams, Ilas, et al. 2013]. The main drawback of this method is that it is not applicable in the situations examined in the first part of the chapter.

Figure 5.1 shows the flow diagram of the TSUNAMI-1D sequence. Resonance self-shielding calculations in SCALE consist of two steps. First, the generic infinitely dilute multi-group cross-sections are initially shielded by the Bondarenko method with BONAMI, using tabulated shielding factors

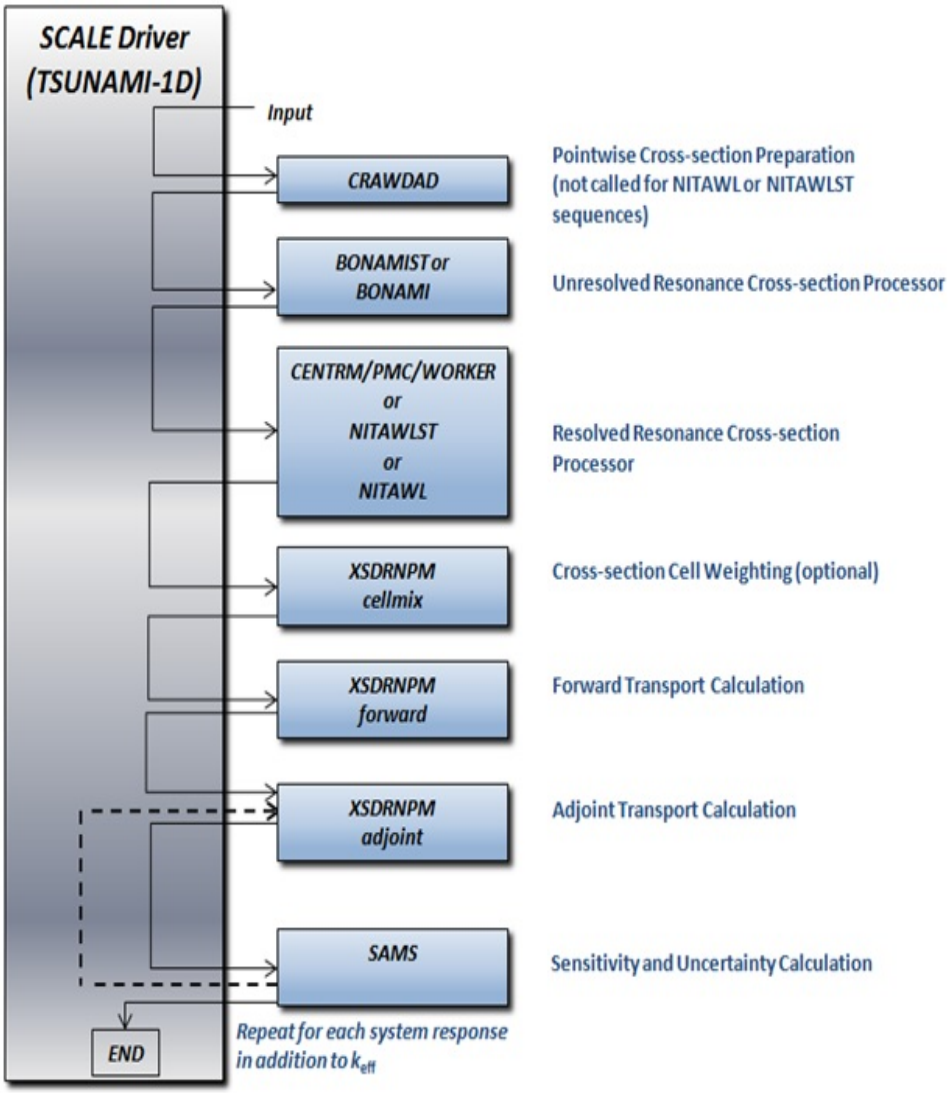

Figure 5.1: The TSUNAMI sequence

on the multi-group libraries. Next, a transport calculation is performed with the one-dimensional discrete ordinates code CENTRM using point-wise cross-sections for the energy range of 0 to $20keV$, which encompasses the resolved resonance ranges of all actinide materials in ENDF/B-VII. The point-wise cross-section data of all nuclides are tabulated on a fine energy grid (e.g., $\sim$ 200000 points for ^{238}U) so that resolved resonances are represented accurately. The point-wise flux spectra computed by CENTRM are used as weight functions in the PMC code to process problem-dependent MG data "on the fly." The shielded cross sections computed by CENTRM/PMC replace the values produced by BONAMI in the resolved range, while the shielded cross sections computed by BONAMI for the unresolved and fast ranges are retained.

After the cross-sections are processed, the TSUNAMI-1D sequence performs two criticality calculations, solving the forward and adjoint forms of the Boltzmann equation, respectively, using the XSDRNPM discrete ordinate code [Greene, Petrie, and M. Williams 2011]. In this step an energy discretization based on a 238-group structure is adopted.The sequence then calls the SAMS module, specifically SAMS5 [Rearden, Petrie, and Jessee 2011], in order to compute the sensitivity coefficients. Once sensitivities are available, the uncertainty on the integral parameters of interest due to the uncertainty in the basic nuclear data are evaluated according to 5.19 using the so-called 44GROUPCOV covariance matrix [M. Williams, Wiarda, et al. 2011].The 44GROUPCOV matrix comprehends a total of 401 materials in a 44-group energy structure.The library includes evaluated covariances obtained from ENDF/B-VII, ENDF/B-VI, and JENDL3.3 for more than 50 materials.

If additional system responses are requested in the input, TSUNAMI-1D executes additional generalized adjoint XSDRNPM and SAMS calculations for each system response. [Rearden, Jesse, and L. Williams 2011]

A similar flow diagram of TSUNAMI-3D sequence can be drawn.The only difference would be the use of NEWT or KENO module to perform forward and adjoint calculations, instead of the XSDRN module. Additional informations can be found in [Rearden 2011].

5.2 The statistical sampling method

In the statistical sampling method all the uncertain parameters are handled as random dependent variables by a sampling procedure. This sampling is performed by using a multi-variate PDF (probabilistic density function). For each randomly sampled set of inputs, a corresponding set of outputs exists: they are the solution to the lattice physics equations acting on the input sample. Inputs can be randomly sampled either one at a time, in groups, or all at once. The dependence of some variables implies that they cannot be sampled without regard to the way they depend on the other variables.

The mean and variance/covariance must be known in order to perform the statistical sampling uncertainty propagation, while the higher order statistical moments can be assumed when not given. The input vector of length n, consisting of all the input variables for a particular system, has a corresponding nxn variance-covariance matrix that describes the uncertainty associated with each element of the input vector, as well as the correlations that exists between elements. The variance-covariance matrix is filled with the second statistical moments of the random variables, so the first statistical moments are put together in the input vector. This vector is used to calculate the best-estimate lattice solution and, for this purpose, is saved in the unperturbed nuclear data library. An example of a part of input vector is showed in figure [5.2]. In this figure the cross-sections are discretized into

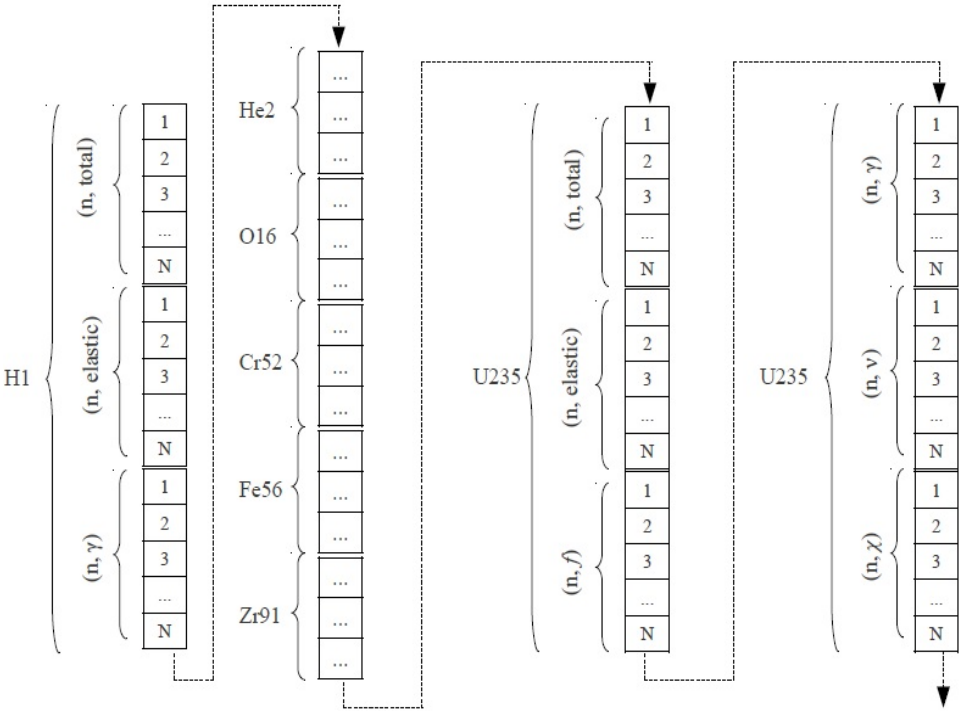

Figure 5.2: An example of input vector

N energy groups. Input vectors usually contain additional parameters, such as tables for the group to group scattering and resonance data. The input vector contains a large number of nuclear data, even for simple systems. In fact, during the sampling procedure, each reaction parameter or cross-section for every nuclide and in every energy group has to be sampled. The number of random variables can amount to tens of thousands also in the analysis of a pin cell. [Ball 2011]

All the problem independent parameters are stored in the multi-group nuclear data libraries, while the problem dependent ones, such as temperatures,

geometry and compositions, are supplied by the user in the input deck.

5.2.1 Theoretical background

The probability of a random variable which corresponds to the individual values assumed by the random variable equals the sum of the probability associated with the values of the set which is:

$$P(a < X < b) = \sum_{a<X<b} P(X = x) \tag{5.20}$$

The random variable is described by the probability density function (PDF) in this way

$$f(x) = \begin{cases} P(X = x), & \{x \in \mathbb{Z} | -\infty \leq x \leq +\infty\} \\ P(x - dx < X < x + dx), & \{x \in \mathbb{R} | -\infty \leq x \leq +\infty\} \end{cases} \tag{5.21}$$

The PDF is the derivative of the cumulative distribution function which is the probability that a random variable X is less or equal to any integer or real number x. The cumulative distribution function is given by

$$F(x) = P(X \leq x) = \begin{cases} \sum\limits_{t \leq x} f(t), & \{t \in \mathbb{Z} | -\infty \leq x \leq x\} \\ \\ \int\limits_{-\infty}^{x} f(t)dt, & \{t \in \mathbb{R} | -\infty \leq x \leq x\} \end{cases} \tag{5.22}$$

Furthermore, the expected value of the population mean (μ), the population variance ($\sigma^2 = E[(X - \mu)^2]$) and the standard deviation (σ) can be expressed by means of the PDF.

$$\mu = E(X) = \begin{cases} \sum\limits_{x} x \cdot f(x), & \{x \in \mathbb{Z} | -\infty \leq x \leq +\infty\} \\ \\ \int\limits_{-\infty}^{+\infty} x \cdot f(x)dx, & \{x \in \mathbb{R} | -\infty \leq x \leq +\infty\} \end{cases} \tag{5.23a}$$

$$\sigma^2 = \begin{cases} \sum\limits_{x} (x - \mu)^2 \cdot f(x), & \{x \in \mathbb{Z} | -\infty \leq x \leq +\infty\} \\ \\ \int\limits_{-\infty}^{+\infty} (x - \mu)^2 \cdot f(x)dx, & \{x \in \mathbb{R} | -\infty \leq x \leq +\infty\} \end{cases} \tag{5.23b}$$

$$\sigma = \sqrt{\sigma^2} = \begin{cases} \sqrt{\sum\limits_{x} (x - \mu)^2 \cdot f(x)}, & \{x \in \mathbb{Z} | -\infty \leq x \leq +\infty\} \\ \\ \sqrt{\int\limits_{-\infty}^{+\infty} (x - \mu)^2 \cdot f(x)dx}, & \{x \in \mathbb{R} | -\infty \leq x \leq +\infty\} \end{cases} \tag{5.23c}$$

The above given formulas express statistical parameters of the input parameters with infinite boundary conditions but are identical for the analysis of output parameter with limited variation.

As the previous formulations indicate, the number of code calculations needs to be defined. The number of code runs is equal to the number of samples which will be generated for each input parameter and is a function of the statistical fidelity. Besides the number of samplings, the distribution of the N values between the minimum and the maximum must be specified. Usually, the distribution, the probability density function (PDF), is not known. By means of empirical distribution function and estimators like quantiles, information about the PDF can be obtained. For a random variable, the quantile is a point in the sample space of the distribution of the considered random variable and can be defined as:

$$P \leq \begin{cases} p, & \{X < x_p\} \\ \\ 1-p, & \{X > x_p\} \end{cases} \tag{5.24}$$

With that definition the tolerance interval can be introduced. The tolerance interval, with L as lower and U as upper interval limit is an estimate of a random variable which contains a fraction of the variables probability, p, with a specified level of confidence, β. That means that the probability of having a sample of the random variable between the lower and upper interval is exactly p and β expresses how sure one is about this. The confidence level accounts for the limited number of samples (or experimental data). For practical reasons, it is possible to write for the first one-sided tolerance limit:

$$P(x_p \leq X^{N+1-l}) \geq \beta \tag{5.25a}$$

$$P(x_p \leq X^{N+1-l}) \geq \sum_{i=0}^{N-m} \binom{N}{i} \cdot p^i \cdot (1-p)^{N-i}. \tag{5.25b}$$

Rewriting the left side of the previous equation 5.25b, which is possible since the sum of the binomial probabilities yield unity, and changing the index, $j = N - i$, will result to the following equation:

$$\sum_{i=0}^{N-l} \binom{N}{i} \cdot p^i \cdot (1-p)^{N-i} = 1 - \sum_{i=N-l+1}^{N} \binom{N}{i} \cdot p^i \cdot (1-p)^{N-i} \tag{5.26a}$$

$$\sum_{i=0}^{N-l} \binom{N}{i} \cdot p^i \cdot (1-p)^{N-i} = 1 - \sum_{j=0}^{l-1} \binom{N}{j} \cdot p^{N-j} \cdot (1-p)^j \tag{5.26b}$$

which yields

$$1 - \sum_{j=0}^{l-1} \binom{N}{j} \cdot p^{N-j} \cdot (1-p)^j \geq \beta. \tag{5.27}$$

The second one-sided tolerance limit can be written as follows:

$$1 - \sum_{i=0}^{u-1} \binom{N}{i} \cdot p^{N-i} \cdot (1-p)^i \geq \beta. \tag{5.28}$$

After the aid of the calculus, the two-sided tolerance limit can be written:

$$1 - \sum_{i=0}^{l+u-1} \binom{N}{i} \cdot p^{N-i} \cdot (1-p)^i \geq \beta. \tag{5.29}$$

Solving the binomial equation yields the following two equations, known as the Wilk's formula for one-side tolerance limit and two-sided tolerance limit:

$$\beta \leq 1 - p^N \tag{5.30a}$$

$$\beta \leq 1 - p^N - N \cdot (1-p) \cdot p^{N-1}. \tag{5.30b}$$

As it can be seen from the equations 5.30a and 5.30b the number of samples depends only on the probability content and on the level of confidence but not on the number of input and source code parameters. [Wilks 1941,Wilks 1942]

5.2.2 GRS method

In this section the method developed by Gesellschaft für Anlagen- und Reaktor-sicherheit (GRS) for uncertainty determination will be presented. The main steps of the GRS method are:

- Identification of potentially relevant uncertainties;
- Definition of uncertainty ranges;
- Specification of subjective probability distributions over these ranges;
- Identification and quantification of dependencies between parameters;
- Generation of a random sample of size N for input parameters from their probability distribution by Monte Carlo method;
- Performing the corresponding simulation runs with the codes;
- Calculation of quantitative uncertainty statements;

- Calculation of quantitative sensitivity measures to identify those uncertain parameters which contribute most to the uncertainty of the results.;
- Interpretation and documentation of results.

A software developed by GRS supports all the steps of uncertainty analysis and is known as SUSA (Software system for Uncertainty and Sensitivity Analyses). Figure 5.3 shows the ranges and probability distributions that are used in the GRS method instead of the parameters' discrete values.

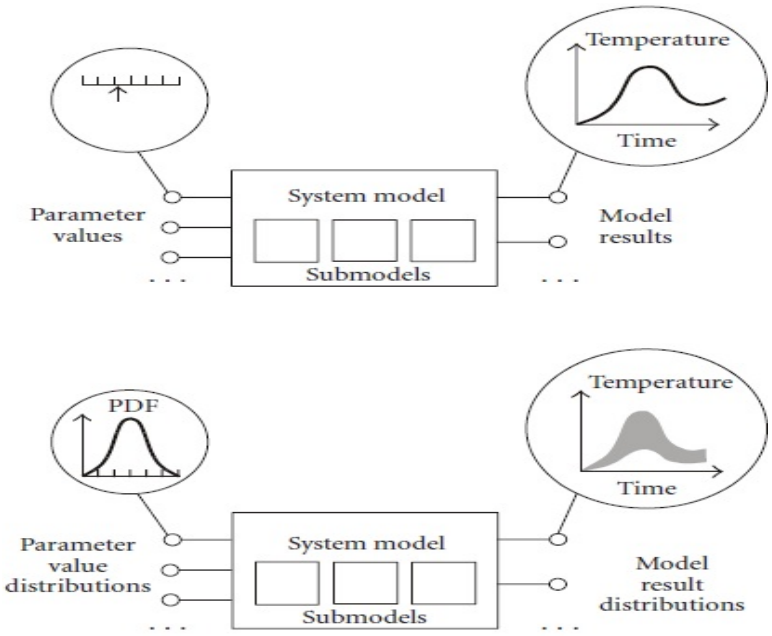

Figure 5.3: Ranges and probability distribution have replaced the discrete values

This method is based on the use of statistical techniques. The main advantage of this approach is that the number of code runs is independent of the number of uncertain parameters. As a consequence, there's no need to create an *a priori* ranking of input parameters in order to reduce the calculation computational cost.

The number of code runs is a consequence of the requested confidence level and probability content, as predicted by the Wilks' formula (Eqs. 5.30a,5.30b). The minimum number of calculations can be found in tables 5.1 and 5.2 for one-sided and two-sided tolerance limits respectively.

Each of the N code calculations is obtained by a simultaneous variation of all input parameters. This variation is performed by means of uncertainty ranges and probability distributions, which represent the state of knowledge of the uncertainties. The choice of a probability distribution for the input

Table 5.1: Minimum number of calculations for one-sided tolerance limits

One-sided	statistical	tolerance	limits
β/p	0.90	0.95	0.99
0.90	22	45	230
0.95	29	59	299
0.99	44	90	459

Table 5.2: Minimum number of calculations for two-sided tolerance limits

Two-sided	statistical	tolerance	limits
β/p	0.90	0.95	0.99
0.90	38	77	388
0.95	46	93	473
0.99	64	130	662

parameters has the consequence that the calculation results show an own probability distribution, from which uncertainty limits or intervals are derived.

The order statistics is used to process the output parameters. The N output values have to be ordered: $X(1) < X(2) < \cdots < X(N-1) < X(N)$. For example, in the case of one-sided tolerance limit with a 95% confidence limit, the 95^{th} percentile is obtained by selecting X(59). For the two-sided tolerance limit X(1) and X(93) have to be chosen, if the same confidence limit and probability content are imposed [Glaeser 2008].

The GRS method has another important characteristic: the possibility to estabilish a ranking of input parameters by means of an evaluation of sensitivity measures of the importance of parameter uncertainties for the global uncertainty of the results. This ranking helps the user to reduce the uncertainty improving the state of knowledge or the modelling of computer codes. It is important to highlight that the ranking is a result of the calculations and not a consequence of *a priori* judgements or estimates, as in other methods.

The ranking is possible thanks to sensitivity measures, like standardised rank regression coefficients, rank correlation coefficients, and correlation ratios. One of the most used sensitivity measure, as in the present work, is the product momentum correlation coefficient (PCC) of Pearson (r)[Bevington and Robinson 2002] which is defined as

$$r = \frac{\sum_{i=1}^{N}(x_i - \mu_x)\cdot(y_i - \mu_y)}{\left[\sum_{i=1}^{N}(x_i - \mu_x)^2 \cdot \sum_{i=1}^{N}(y_i - \mu_y)^2\right]^{1/2}}. \tag{5.31}$$

Another advantage of this method is that it doesn't make use of any approximations, relying only on actual code calculations.

5.2.3 SAMPLER module

SCALE6.2 has three modules to perform sensitivity and uncertainty analysis: KENO, which is not described here since it was not used to perform calculations, TSUNAMI, described in section 5.1.4, and the new SAMPLER, which allows for statistical sampling of any SCALE sequence. SAMPLER is a "super-sequence" that perturbs the input parameters and then use them to solve reactor physics calculations with any SCALE sequence, such as NEWT or KENO.

SAMPLER perturbs multigroup cross-sections, fission yields, decay data and model parameters (temperatures, dimensions, nuclide concentrations) [Rearden, Dunn, et al. 2013]. To do that, SAMPLER uses libraries of perturbation factors previously computed by code such as XSUSA (see 5.2.4). The cross-sections perturbations are sampled from the covariance library of SCALE and the decay ones come from the ENDF/B-VII uncertainties. Moreover the Oak Ridge National Laboratory (ORNL) has developed a library of yield covariances.

Figure 5.4 shows the calculations performed by SAMPLER.

The following list shows the types of responses produced by SAMPLER and the sequences used to obtain the requested output:

- k eigenvalue - XSDRN, NEWT, KENO;
- microscopic reaction rates by nuclide - NEWT and OPUS;
- homogenized/collapsed macro cross sections - NEWT;
- nuclide concentrations, activities - ORIGEN;
- decay heat, radiotoxicity, photon sources - ORIGEN;
- shield responses: doses, radiation damage, etc. - MAVRIC.

For each of these responses at every time-step frequency distributions, mean values and standard deviations, results of chi-squared normality test, covariance and correlation coefficients between responses are printed in the output folder [M. Williams, Havluj, et al. 2013].

The computational time is reduced by the use of parallel computations with MPI or OpenMP.

5.2.4 XSUSA method

The XSUSA code extends the SUSA code package developed by GRS to applications with nuclear data covariances. XSUSA randomly selects nuclear

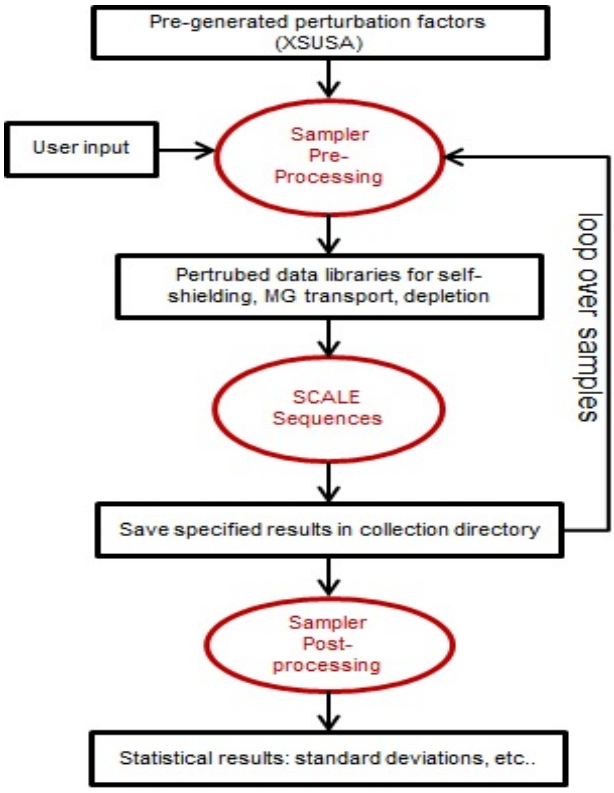

Figure 5.4: Scheme of SAMPLER calculations

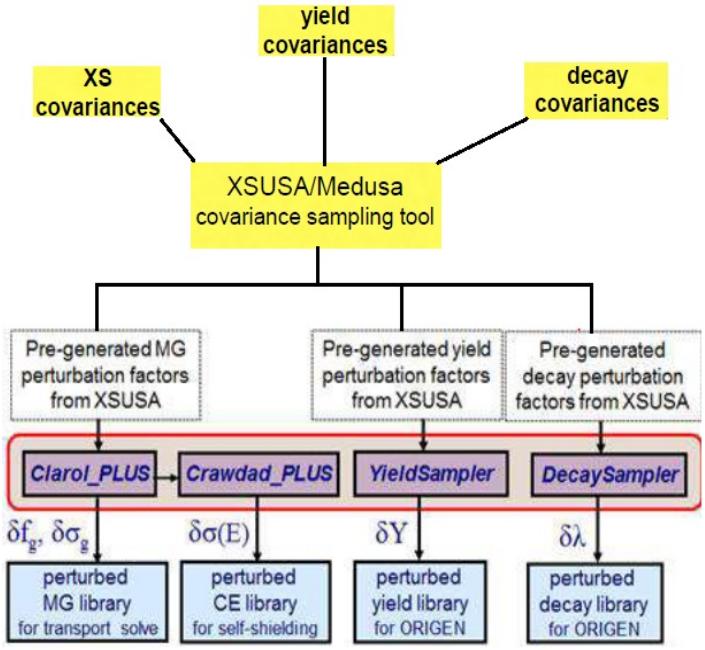

Figure 5.5: Generation of perturbed data libraries

data values with the sampling module MEDUSA and applies the samples to the reference nuclear data. [Krzykacz, Hofer, and Kloos 2014]

XSUSA is used to produce random multi-group (MG) data values by sampling covariances in the SCALE library. The typical approach is to assume that the MG data probability density function is a multivariate normal distribution, which is completely defined by the expected values and covariance matrices for the data. An XSUSA statistical sample consists of a full set of perturbed, infinitely dilute MG data for all groups, reactions, and materials. The SCALE MG covariance data are given as relative values of the infinitely dilute cross-sections, so a random perturbation sample for cross-sections, $\sigma_{x,g}(\infty)$, corresponds to $\Delta\sigma_{x,g}(\infty)/\sigma_{x,g}(\infty)$. XSUSA converts these values to a set of multiplicative perturbation factors $Q_{x,g}$ that are applied to the reference data to obtain the altered values:

$$\sigma'_{x,g} = Q_{x,g}\sigma_{x,g} \tag{5.32}$$

where

$$Q_{x,g} = 1 + \frac{\Delta\sigma_{x,g}(\infty)}{\sigma_{x,g}(\infty)}. \tag{5.33}$$

The multiplicative perturbation factors for all data are preprocessed and stored in a data file for subsequent SCALE calculations. In this manner the

XSUSA data sampling must be done only once. The perturbation library currently consists of 1000 random values for each infinitely dilute MG data parameter.

In addition to infinitely dilute MG data, also point-wise (PW) cross-sections and shielding factors are contained in the computational data vector (CDV) that will be used as an input by SCALE. These quantities are highly correlated, since the PW cross-sections appear in the definitions of infinitely dilute MG data and of the self-shielding factor f [see M. Williams, Ilas, et al. 2013]. For that reason, the three types of data appearing in the CDV cannot be sampled independently. For example, an energy-dependent perturbation in the PW cross-section $\sigma_x(E)$ causes the infinitely dilute MG cross section to be perturbed as follows:

$$\sigma_{x,g}^{'} = \frac{\langle \sigma_x(u)^{'} \rangle}{\Delta u_g}, \tag{5.34}$$

where u is the letargy and the angle brackets indicate lethargy integration over group g.

The perturbed shielding factor can be obtained in a similar way, using the definition of Bondarenko self-shielding factor ($f_{x,g}(\sigma_0) = \sigma_{x,g}(\sigma_0)/\sigma_{x.g}(\infty)$) [M. Williams 2011], as:

$$f_{x,g}^{'}(\sigma_0) = \frac{1}{\sigma_{x,g}^{'}(\infty)} \frac{\left\langle \frac{\sigma_x^{'}(u)}{\sigma_t^{'}(u)+\sigma_0} \right\rangle}{\left\langle \frac{1}{\sigma_t^{'}(u)+\sigma_0} \right\rangle}, \tag{5.35}$$

where $\sigma_{x,g}(\sigma_0)$ is the self-shielded cross-section at σ_0, represented with the narrow-resonance approximation as:

$$\sigma_{x,g}(\sigma_0) = \frac{\left\langle \frac{\sigma_x(u)}{\sigma_t(u)+\sigma_0} \right\rangle}{\left\langle \frac{1}{\sigma_t(u)+\sigma_0} \right\rangle}. \tag{5.36}$$

Since no covariance data are available for the energy-dependent PW cross-sections, a simple approximation is used to obtain consistent, correlated perturbations in $\sigma_x(u)$, $\sigma_{x,g}(\infty)$ and $f_{x,g}(\sigma_0)$. A comparison of the perturbed, infinitely dilute data expressions in Eqs. 5.32 and 5.34 shows that the two expressions are equivalent if the PW data are perturbed in the following manner:

$$\sigma_x^{'}(u) = Q_{x,g}\sigma_x(u), \tag{5.37}$$

i.e., the PW data are changed uniformly at all energy points within a group.

The perturbed MG shielding factor, defined in Eq. 5.35, is evaluated in a similar manner. Applying the approximation in Eq. 5.37, Eq. 5.35 can be written as

$$f_{x,g}^{'}(\sigma_0) = \frac{1}{Q_{x,g}\sigma_{x,g}(\infty)} \frac{\left\langle \frac{Q_{x,g}\sigma_x(u)}{Q_{t,g}\sigma_t(u)+\sigma_0} \right\rangle}{\left\langle \frac{1}{Q_{t,g}\sigma_t(u)+\sigma_0} \right\rangle}, \tag{5.38}$$

After simplifying, Eq. 5.38 becomes

$$f^{'}_{x,g}(\sigma_0) \leftarrow f_{x,g}(\sigma^{'}_0), \tag{5.39}$$

where $\sigma^{'}_0 = \sigma_0/Q_{t,g}$. Therefore the perturbed shielding factor is obtained by simply evaluating the original f-factor tabulation at a modified background cross-section value.

Fig. 5.5 shows an overview of the generation of perturbed data.

Chapter 6

Submission of the uncertainty analysis results

The uncertainty analysis performed in this thesis work is divided into two parts. In the first part TSUNAMI and SAMPLER codes were tested on the Benchmark for Uncertainty Analysis in Modelling (UAM) for the Design, Operation and Safety Analysis of LWRs [K. Ivanov, Avramova, et al. 2013]. In the second part the two assemblies presented in the OECD VVER-1000 LEU and MOX assembly computational benchmark [Kalugin et al. 2002] were analysed to understand how SAMPLER behaves with more complex geometries. Moreover four unit cells taken from these two assemblies (one with gadolinium and three with different loadings of plutonium) are modelled and studied. The UAM benchmark model will be described in the first section of this chapter. In the following sections the results of the work will be presented.

6.1 UAM Benchmark model

In order to determine the uncertainty in the calculations of light water reactors systems, both in the reactor physics calculation and in the thermal hydraulics modelling, a dedicated Expert Group was created in 2005 within the OECD/NEA Nuclear Science Committee and a Benchmark exercise was launched. Several well-defined problems with complete sets of input specifications and reference experimental data were used as bases to establish a benchmark for uncertainty analysis in best estimate modelling and coupled multiphysics and multiscale LWR analysis. This benchmark was created to study the uncertainty in LWR system calculations at all stages of coupled reactor physics/thermal hydraulics calculation.

The UAM benchmark has been structured in three different phases: the "Neutronics Phase", the "Core Phase" and the "System Phase". Each of them is subdivided in three or four exercises with the purpose of studying how the

uncertainty propagates in the modelling across different scales (multi-scale) and physics phenomena (multi-physics).

This work is devoted to the solutions of some selected test problems within the Exercises I-1 ("Cell Physics") and I-2 ("Lattice Physics") of Phase I. Phase I has been thought to understand the uncertainties related with the most important reactor core parameters of LWRs. The sources of these uncertainties are the modelling errors, the numerical approximations and the input data uncertainties.

The "Cell Physics" exercise is focused on the derivation of the multi-group microscopic cross-section libraries and their uncertainties. Its purpose is to address the uncertainties due to the basic nuclear data as well as the impact of processing the nuclear and covariance data, selection of multi-group structure, and self-shielding treatment. Within Exercise I-1 the uncertainties in the evaluated Nuclear Data Libraries (NDLs) are propagated into multigroup microscopic cross-sections.

The "Lattice Physics" exercise is focused on the derivation of the few-group macroscopic cross-section libraries and their uncertainties. The multi-group cross-section uncertainties calculated in Exercise I-1 are input uncertainties which are then propagated through the lattice physics calculations to few-group cross-section uncertainties.

6.1.1 Exercise I-1 specifications

Within the framework of the "Cell Physics" exercise three pin-cell have been considered: a BWR Peach Bottom-2 pin-cell [Solis et al. 2001], a PWR Three Miles Island-1 pin-cell [K. Ivanov, Beam, et al. 1999] and a VVER-1000 Kozloduy-6 pin-cell [B. Ivanov et al. 2002]. The two types of basic geometries for the unit cells are outlined in Figure 6.1.

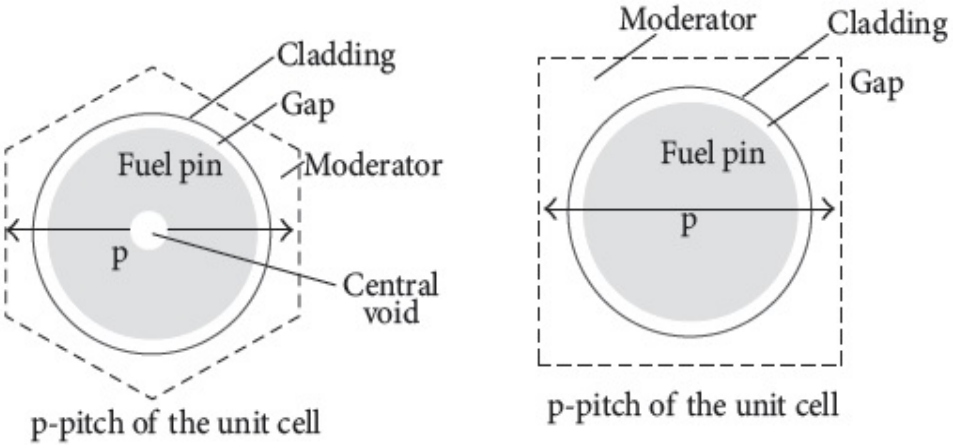

Figure 6.1: Types of geometries for the fuel pin-cell test cases within Exercise I-1

Table 6.1: Parameters of PB-2 BWR unit cell

Parameter	value
Unit cell pitch [mm]	18.75
Fuel pellet diameter [mm]	12.1158
Fuel pellet material	UO_2
Fuel density [g/cm^3]	10.42
Fuel enrichment [w/o]	2.93
Cladding outside diameter [mm]	14.3002
Cladding thickness [mm]	0.9398
Cladding material	Zircaloy-2
Cladding density [g/cm^3]	6.55
Gap material	He
Moderator material	H_2O

Table 6.2: PB-2 BWR operating conditions

Operating conditions	HZP	HFP
Fuel temperature [K]	552.833	900
Cladding temperature [K]	552.833	600
Moderator temperature [K]	552.833	557
Moderator density [kg/m^3]	753.978	460.72
Reactor power [MW_t]	3293	3293
Void fraction [%]	-	40

Each pin-cell model should be analysed at Hot Full Power conditions (HFP) as well as Hot Zero Power (HZP) conditions. The reflective boundary condition should be applied on all surfaces of the VVER-1000, PWR and BWR unit cells. Tables from 6.1 to 6.6 show the specifications of the three test problems and the relative conditions at HFP and HZP.

To enhance the differences between the three pincells (PWR, BWR and VVER) for the Exercise I-1, a 40% void fraction (with a corresponding moderator density of 460.72 kg/m^3) is set for the HFP case of the BWR, instead of 0%. Hence the PWR and BWR cases are for square pitch but with different spectra, while the VVER case is for triangular pitch.

The atom density for ^{234}U is 0.0054 wt % for all the three cases. The composition of the air for the central void of the Kozloduy-6 VVER-1000 unit cell is 79% nitrogen and 21% oxygen.

The requested results include k-eff and its uncertainties and the microscopic absorption and fission cross-section and its uncertainties for ^{235}U and ^{238}U. Moreover, the top five contributors of the uncertainty in k-eff are also requested in order to identify neutron-nuclide reactions that contribute to

Table 6.3: Parameters of TMI-1 PWR unit cell

Parameter	value
Unit cell pitch [mm]	14.427
Fuel pellet diameter [mm]	9.391
Fuel pellet material	UO_2
Fuel density [g/cm^3]	10.283
Fuel enrichment [w/o]	4.85
Cladding outside diameter [mm]	10.928
Cladding thickness [mm]	0.673
Cladding material	Zircaloy-4
Cladding density [g/cm^3]	6.55
Gap material	He
Moderator material	H_2O

Table 6.4: TMI-1 PWR operating conditions

Operating conditions	HZP	HFP
Fuel temperature [K]	551	900
Cladding temperature [K]	551	600
Moderator temperature [K]	551	562
Moderator density [kg/m^3]	766	784.4
Reactor power [MW_t]	2772	2772

Table 6.5: Parameters of Kozloduy-6 VVER-1000 unit cell

Parameter	value
Unit cell pitch [mm]	12.75
Fuel pellet diameter [mm]	7.56
Fuel pellet material	UO_2
Fuel density [g/cm^3]	10.4
Fuel enrichment [w/o]	3.3
Central void diameter [mm]	1.4
Central void material	dry air
Cladding outside diameter [mm]	9.1
Cladding thickness [mm]	0.69
Cladding material	Zr + 1 % Nb
Cladding density [g/cm^3]	6.44
Gap material	He
Moderator material	H_2O

most of the uncertainties.

6.1.2 Exercise I-2 specifications

Within Exercise I-2, different stand-alone neutronics single fuel assembly and minicore test problems have been proposed. In this work the solutions for the Kozloduy-6 VVER-1000 fuel assembly will be presented. Figure 6.2 shows the geometry of the analysed fuel assembly.

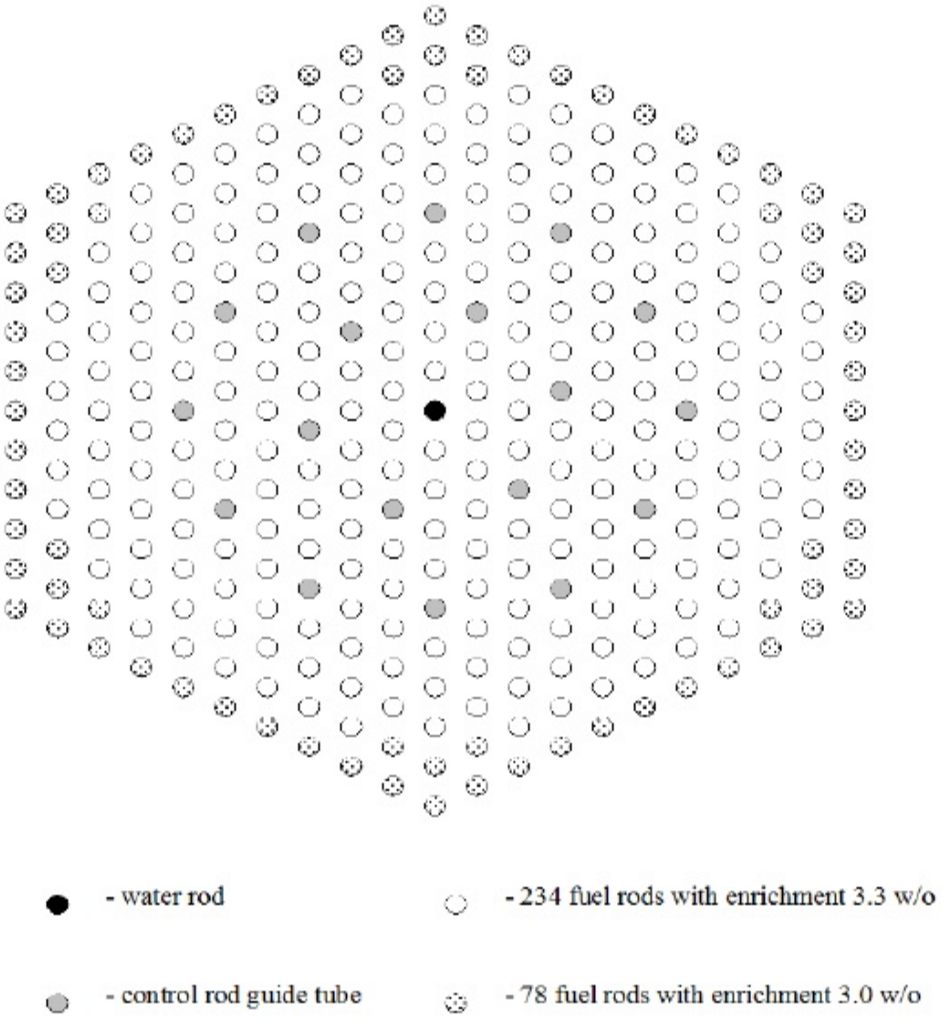

Figure 6.2: Kozloduy-6 VVER-1000 fuel assembly

This problem should be analysed at Hot Zero Power conditions as well as Hot Full Power conditions as defined for the Exercise I-1 and a reflective boundary condition should be used. Both conditions with the control rods completely inserted and with the control rods completely withdrawn should

be studied. The parameter used for modelling this assembly are listed in table 6.7.

More informations about the benchmark specifications may be found in K. Ivanov, Avramova, et al. 2013, especially in chapter 2.4 for the three unit cells and in chapter 3.2 for the VVER-1000 fuel assembly.

6.2 Results of the UAM benchmark

The k-eff values and associated uncertainties calculated with TSUNAMI and SAMPLER are presented in table 6.8 for Exercise I-1 and in table 6.9 for Exercise I-2. Uncertainties are shown in terms of $\%\Delta R/R$. It is possible to notice that the reactivities calculated for all the cases at HFP conditions are consistently lower than those at HZP conditions, because of the negative fuel Doppler coefficient. The computed uncertainties of the k-eff show a good agreement between the two codes. They have been evaluated to be 0.5%–0.6% for all the test cases.

Figure 6.3 shows the five cross-sections which contribute the most to the k-eff uncertainty for the Exercise I-1. The data plotted in this chart have been obtained only with the TSUNAMI code, because the SAMPLER code has not a similar capability. For the three unit cells the five highest contributions are the same. The first three are also in the same order: the ^{238}U(n,γ) is the most important, followed by the ^{235}Unubar (average number of neutrons per fission reaction—ν) and ^{235}U(n,γ). The last two are ^{238}U(n,n') and the ^{235}U(n,fission), but for the VVER-1000 unit cell they are in reverse order.

The reasons to justify these contributions to the uncertainties can be three: the highest sensitivities associated to such reactions, the highest value of the associated covariances, or a combination of both. In the case of ^{238}U(n,γ) the k-eff is quite sensitive to its value (especially in the unresolved resonance regions), but, on the other hand, its evaluation is still quite "uncertain", and evaluated cross-sections from various sources differ by more than their assigned uncertainties [Trkov, Molnár, and Révay 2005].

Table 6.10 shows the explicit and implicit contributions to the total sensitivity coefficient of the five cross-sections which contribute the most to the k-eff uncertainty. Again, only with TSUNAMI it is possible to obtain this kind of result. These contributions are shown only for the VVER-1000 unit cell for the sake of brevity.

In the framework of Exercise I-1, the UAM benchmark has requested also the determination of the uncertainty associated to the calculation of the one-group absorption and fission microscopic cross-sections for ^{235}U and ^{238}U. The results are given in tables 6.11 and 6.12. The numbers in parenthesis are the uncertainties of each cross-sections values. The uncertainty of the microscopic cross-section values is around one order of magnitude higher than the one of the k-eff cases, ranging in between ~ 1 % and ~ 4 %. The routine

Table 6.6: Kozloduy-6 VVER-1000 operating conditions

Operating conditions	HZP	HFP
Fuel temperature [K]	552.15	900
Cladding temperature [K]	552.15	600
Moderator temperature [K]	552.15	562
Moderator density [kg/m^3]	767	752.5
Reactor power [MW_t]	3000	3000

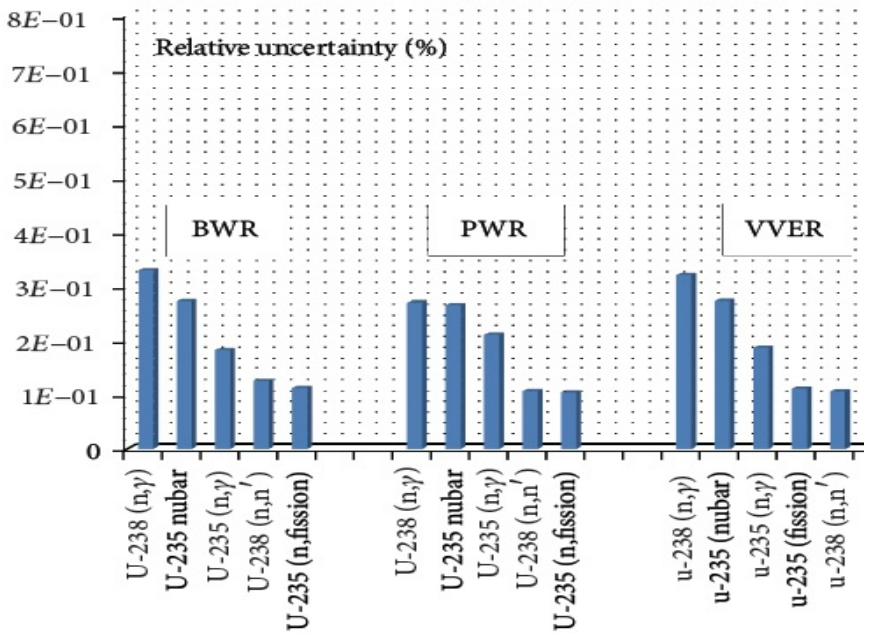

Figure 6.3: The top five contributions to the uncertainty of the k-eff for the BWR, PWR and VVER-1000 unit cells

Table 6.7: Parameters of Kozloduy-6 VVER-1000 fuel assembly

Parameter	value
Number of fuel rods	312
Number of fuel rods with 3.0 w/o enrichment	78
Number of fuel rods with 3.3 w/o enrichment	234
Number of water rods per FA	1
Number of guide tubes	18
Pellet diameter [mm]	7.56
Central void diameter [mm]	1.4
Cladding outside diameter [mm]	9.1
Cladding thickness [mm]	0.69
Fuel rods pitch [mm]	12.75
Guide tube outside diameter [mm]	12.6
Guide tube inside diameter [mm]	11.0
Absorber pellet diameter [mm]	7.0
Absorber cladding outside diameter [mm]	8.2
Water rod outside diameter [mm]	11.2
Water rod inside diameter [mm]	9.6

to calculate the microscopic cross-section values is not yet implemented in SAMPLER: at the moment only a beta version of this code is available. The highest uncertainty value was systematically found for the fission cross-section of ^{238}U.

In Tables 6.11 and 6.12, it is possible to see that all the cross-sections are almost the same for both the conditions (HZP and HFP) of each reactor type, with the only exception of the BWR in which the cross-section values double in the HFP conditions with respect of the HZP ones. This is due to the harder spectrum of the BWR HFP state, as a consequence of the imposed 40 % void fraction.

The benchmark requires for Exercise I-2 some homogenized macroscopic cross-sections with the associated uncertainties. The results are given in tables 6.13 and 6.14 for the HZP conditions and in table 6.15 and 6.16 for the HFP conditions. A two group subdivision (cutoff energy 0.625 eV) has been used.

The first energy group (E>0.625 eV) has generally the highest associated uncertainties. Moreover, as a general trend, the calculated uncertainties are very consistent within all the test cases and within the two codes. These tables highlight one of the most important capability of SAMPLER: in fact, while in TSUNAMI it is not possible to evaluate the uncertainty related to all the requested parameter, since each uncertainty evaluation requires an additional adjoint transport calculation, in SAMPLER it is possible to gather uncertainty informations about each of the requested parameter without any

Table 6.8: Exercise I-1: k-eff results

Test cases	TSUNAMI	Uncertainty [%]	SAMPLER	Uncertainty [%]
BWR				
HZP	1.34050	5.23E-01	1.34249	5.17E-01
HFP	1.22270	6.16E-01	1.22533	6.23E-01
PWR				
HZP	1.42290	4.82E-01	1.42635	4.79E-01
HFP	1.40424	4.89E-01	1.40670	4.88E-01
VVER-1000				
HZP	1.34498	5.13E-01	1.34879	5.04E-01
HFP	1.32725	5.20E-01	1.32993	5.12E-01

Table 6.9: Exercise I-2: k-eff results

Test cases	TSUNAMI	Uncertainty [%]	SAMPLER	Uncertainty [%]
VVER-1000				
HZP_{rodded}	0.94730	5.08E-01	0.94591	5.04E-01
HFP_{rodded}	0.93199	5.12E-01	0.93328	5.12E-01
$HZP_{unrodded}$	1.33818	5.03E-01	1.34050	4.83E-01
$HFP_{unrodded}$	1.32299	5.15E-01	1.32741	4.88E-01

Table 6.10: Explicit and implicit contributions to the total sensitivity coefficient for the VVER-1000 unit cell

Reaction	Explicit	Implicit
HZP		
^{238}U (n,γ)	-2.57E-01	1.01E-02
^{235}U nubar	9.41E-01	0.00
^{235}U (n,γ)	-1.39E-01	-1.11E-04
^{238}U (n,n')	-5.51E-03	-2.57E-06
^{235}U fission	2.83E-01	-4.14E-04
HFP		
^{238}U (n,γ)	-2.63E-01	1.05E-02
^{235}U nubar	9.40E-01	0.00
^{235}U (n,γ)	-1.40E-01	-2.07E-04
^{238}U (n,n')	-5.81E-03	-2.92E-06
^{235}U fission	2.83E-01	-4.57E-04

Table 6.11: Exercise I-1: microscopic absorption cross-sections

Test cases	^{235}U absorption [barn]	^{238}U absorption [barn]
BWR		
HZP	2.01E+01 (1.04E+00)	3.10E-01 (9.80E-01)
HFP	4.15E+01 (1.22E+00)	8.80E-01 (9.70E-01)
PWR		
HZP	4.41E+01 (1.09E+00)	9.42E-01 (9.65E-01)
HFP	4.30E-01 (1.10E+00)	9.64E-01 (9.71E-01)
VVER-1000		
HZP	5.98E+01 (1.02E+00)	1.02E+00 (9.88E-01)
HFP	5.84E+01 (1.03E+00)	1.04E+00 (9.90E-01)

Table 6.12: Exercise I-1: microscopic fission cross-sections

Test cases	^{235}U fission [barn]	^{238}U fission [barn]
BWR		
HZP	1.65E+01 (1.06E+00)	3.01E-02 (4.07E+00)
HFP	3.34E+01 (1.22E+00)	8.57E-02 (4.79E+00)
PWR		
HZP	3.57E+01 (1.10E+00)	9.91E-02 (3.92E+00)
HFP	3.47E+01 (1.11E+00)	9.91E-02 (3.94E+00)
VVER-1000		
HZP	4.90E+01 (1.04E+00)	9.26E-02 (3.86E+00)
HFP	4.78E+01 (1.05E+00)	9.27E-02 (3.88E+00)

Table 6.13: Exercise I-2: macroscopic cross-sections for HZP conditions with the control rods completely inserted

Reaction	Energy gr.	TSUNAMI [cm^{-1}]	SAMPLER [cm^{-1}]
Total	1	5.51E-01 (-)	5.50E-01 (8.95E-01)
	2	1.37E+00 (-)	1.37E+00 (1.50E-01)
Fission	1	2.41E-03 (5.07E-01)	2.43E-03 (5.50E-01)
	2	5.61E-02 (3.28E-01)	5.70E-02 (3.37E-01)
Absorption	1	1.41E-02 (1.34E+00)	1.41E-02 (9.08E-01)
	2	9.48E-02 (8.81E-01)	9.65E-02 (1.99E-01)
Scattering	1	5.37E-01 (8.43E-01)	5.36E-01 (8.99E-01)
	2	1.27E+00 (1.59E-01)	1.27E+00 (1.61E-01)
Nufission	1	6.16E-03 (-)	6.22E-03 (8.42E-01)
	2	1.37E-01 (-)	1.39E-01 (4.54E-01)

Table 6.14: Exercise I-2: macroscopic cross-sections for HZP conditions with the control rods completely withdrawn

Reaction	Energy gr.	TSUNAMI [cm^{-1}]	SAMPLER [cm^{-1}]
Total	1	5.62E-01 (-)	5.62E-01 (8.58E-01)
	2	1.37E+00 (-)	1.37E+00 (1.48E-01)
Fission	1	2.57E-03 (4.43E-01)	2.59E-03 (4.69E-01)
	2	5.60E-02 (3.28E-01)	5.67E-02 (3.36E-01)
Absorption	1	9.25E-03 (1.28E+00)	9.23E-03 (8.48E-01)
	2	8.21E-02 (8.68E-01)	8.31E-02 (2.28E-01)
Scattering	1	5.53E-01 (8.10E-01)	5.53E-01 (8.61E-01)
	2	1.29E+00 (1.58E-01)	1.29E+00 (1.56E-01)
Nufission	1	6.52E-03 (-)	6.58E-03 (7.30E-01)
	2	1.36E-01 (-)	1.38 E-01 (4.53E-01)

Table 6.15: Exercise I-2: macroscopic cross-sections for HFP conditions with the control rods completely inserted

Reaction	Energy gr.	TSUNAMI [cm^{-1}]	SAMPLER [cm^{-1}]
Total	1	5.43E-01 (-)	5.44E-01 (9.00E-01)
	2	1.34E+00 (-)	1.35E+00 (1.51E-01)
Fission	1	2.40E-03 (5.13E-01)	2.42E-03 (5.55E-01)
	2	5.56E-02 (3.29E-01)	5.65E-02 (3.37E-01)
Absorption	1	1.42E-02 (1.37E+00)	1.42E-02 (9.18E-01)
	2	9.40E-02 (8.85E-01)	9.56E-02 (2.00E-01)
Scattering	1	5.29E-01 (8.47E-01)	5.29E-01 (9.03E-01)
	2	1.25E+00 (1.60E-01)	1.25E+00 (1.63E-01)
Nufission	1	6.12E-03 (-)	6.19E-03 (8.48E-01)
	2	1.35E-01 (-)	1.38E-01 (4.54E-01)

Table 6.16: Exercise I-2: macroscopic cross-sections for HFP conditions with the control rods completely withdrawn

Reaction	Energy gr.	TSUNAMI [cm^{-1}]	SAMPLER [cm^{-1}]
Total	1	5.55E-01 (-)	5.55E-01 (8.62E-01)
	2	1.34E+00 (-)	1.35E+00 (1.49E-01)
Fission	1	2.55E-03 (4.47E-01)	2.58E-03 (4.72E-01)
	2	5.54E-02 (3.28E-01)	5.62E-02 (3.36E-01)
Absorption	1	9.40E-03 (1.30E+00)	9.38E-03 (8.60E-01)
	2	8.12E-02 (8.72E-01)	8.22E-02 (2.29E-01)
Scattering	1	5.45E-01 (8.14E-01)	5.45E-01 (8.65E-01)
	2	1.26E+00 (1.59E-01)	1.26E+00 (1.57E-01)
Nufission	1	6.49E-03 (-)	6.56E-03 (7.33E-01)
	2	1.35E-01 (-)	1.37E-01 (4.53E-01)

increase of the computational time (or with a meaningless one).

One of the other interesting features of SAMPLER is the possibility to study the physics of the analysed system by means of the correlation matrix printed by the code. An example of correlation matrix, and in particular that for the VVER-1000 unit cell in the HFP conditions, is provided by figure 6.4. The figure represents only one half of the matrix, but all the informations are preserved anyway, given the symmetry of the matrix. The coloured numbers help in the understanding of this useful tool. The number in the cell between the macroscopic total cross-section of the group 1 and the macroscopic absorption cross-section of the group 1 is close to 1 (0.75) and this means that there is a direct correlation between these two quantities. Physically, if the absorption cross-section increased, also the total cross-section would increase, since it is the sum of absorption and fission cross-sections. Vice versa the red number (-0.61) is negative and quite close to -1: the fission and absorption macroscopic cross-sections are anticorrelated. Nothing can be said about those quantities with a number of correlation close to 0, whether positive or negative.

The SAMPLER outputs include the histogram of the frequency with whom the results occur. The global shape of the columns of this histogram should look like the gaussian curve, since this distribution has been assumed as initial hypothesis for the samples. Figure 6.5 shows two histograms for the VVER-1000 unit cell in the HFP conditions, respectively using 93 and 662 samples. These numbers have been chosen because they coincide with the number of samples predicted, respectivel, by the 95%/95% and the 99%/99% criteria of the Wilk's formula for the two-sided tolerance limit. Comparing these two plots, we can see that the shape of the columns becomes more similar to the gaussian distribution with the increase of the number of the

k_{inf}	1,00								
$\Sigma_{a,\,gr.1}$	0,01	1,00							
$\Sigma_{a,\,gr.2}$	-0,27	0,17	1,00						
$\Sigma_{f,\,gr.1}$	0,44	-0,61	-0,09	1,00					
$\Sigma_{f,\,gr.2}$	0,52	-0,19	0,32	0,17	1,00				
$\Sigma_{t,\,gr.1}$	-0,33	0,75	0,11	-0,58	-0,08	1,00			
$\Sigma_{t,\,gr.2}$	0,06	-0,09	0,04	-0,08	0,01	-0,07	1,00		
$\Sigma_{e,\,gr.1}$	-0,33	0,74	0,11	-0,58	-0,08	1,00	-0,07	1,00	
$\Sigma_{e,\,gr.2}$	0,08	-0,11	-0,03	-0,07	-0,01	-0,08	1,00	-0,08	1,00
	k_{inf}	$\Sigma_{a,\,gr.1}$	$\Sigma_{a,\,gr.2}$	$\Sigma_{f,\,gr.1}$	$\Sigma_{f,\,gr.2}$	$\Sigma_{t,\,gr.1}$	$\Sigma_{t,\,gr.2}$	$\Sigma_{e,\,gr.1}$	$\Sigma_{e,\,gr.2}$

Figure 6.4: The correlation matrix for the VVER-1000 unit cell in the HFP conditions

samples.

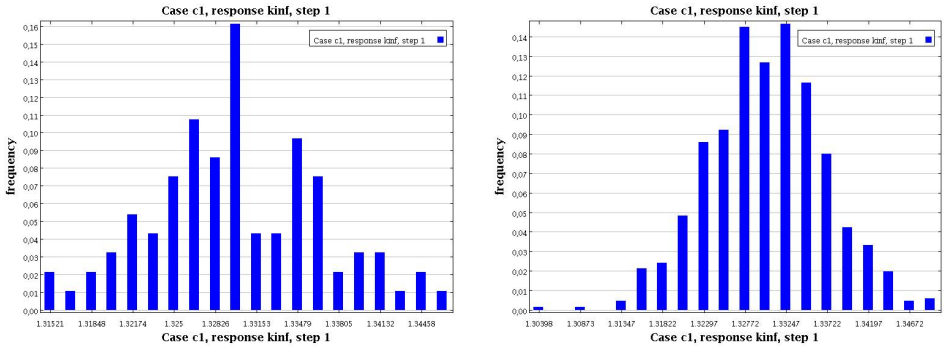

(a) 93 *samples* (b) 662 *samples*

Figure 6.5: Frequency plots for VVER-1000 with 93 and 662 samples

6.3 Uncertainty results for the OECD benchmark

As said in the introduction of this chapter, the two assemblies presented in the OECD VVER-1000 LEU and MOX assembly computational benchmark and four different pincells have been analysed. In this section the four pincells will be briefly described and the results of this study will be presented and commented.

Table 6.17 shows the k-eff values of both assemblies and the associated uncertainties, while the five cross-sections which contribute the most to the k-eff uncertainty are given in table 6.18. The global uncertainty associated to the k-eff of the MOX fuel assembly is almost twice that associated to the k-eff of LEU assembly and this outcome can be explained with the presence of plutonium. In fact, the predominant component to the total uncertainty comes from the ^{239}Pu nubar for the high sensitivities associated to it. It is followed by the ^{239}Pu fission and ^{239}Pu(n,γ). Particularly the most important reaction in the MOX fuel assembly, the ^{239}Pu nubar, has three times higher contribution than the corresponding reaction in the LEU fuel assembly (^{238}U(n,γ)).

The macroscopic cross-sections for the two fuel assemblies are given in tables 6.19 and 6.20. As it was done for the VVER-1000 fuel assembly of the UAM benchmark, a two group division has been adopted with a cutoff energy of 0.625 eV. The numbers in parenthesis represent the uncertainty (%) associated to each value of cross-section. The results obtained with TSUNAMI are in excellent agreement with those obtained with SAMPLER, both for cross-sections and for associated uncertainties.

To better understand how the presence of gadolinium and an increasing

Table 6.17: Values of the k-eff and its uncertainty for LEU and MOX fuel assemblies

TSUNAMI	Uncertainty [%]	SAMPLER	Uncertainty [%]
LEU			
1.16750	5.12E-01	1.17067	5.15E-01
MOX			
1.19183	1.09E+00	1.19030	1.05E+00

Table 6.18: Highest contributions to the k-eff uncertainty for LEU and MOX assemblies

Covariance matrix		Uncertainty [%]
Nuclide-Reaction	Nuclide-Reaction	
LEU		
^{238}U (n,γ)	^{238}U (n,γ)	3.01E-01
^{235}U nubar	^{235}U nubar	2.64E-01
^{235}U (n,γ)	^{235}U (n,γ)	1.67E-01
^{238}U (n,n')	^{238}U (n,n')	1.41E-01
^{235}U chi	^{235}U chi	1.17E-01
MOX		
^{239}Pu nubar	^{239}Pu nubar	9.10E-01
^{239}Pu fission	^{239}Pu fission	2.86E-01
^{239}Pu (n,γ)	^{239}Pu (n,γ)	2.83E-01
^{239}Pu fission	^{239}Pu (n,γ)	2.66E-01
^{238}U (n,γ)	^{238}U (n,γ)	2.40E-01

Table 6.19: Macroscopic cross-sections for LEU fuel assembly

Reaction	Energy gr.	TSUNAMI [cm^{-1}]	SAMPLER [cm^{-1}]
Total	1	5.36E-01 (-)	5.39E-01 (9.28E-01)
	2	1.34E+00 (-)	1.31E+00 (1.61E-01)
Fission	1	2.94E-03 (4.20E-01)	2.96E-03 (4.23E-01)
	2	6.29E-02 (3.26E-01)	6.32E-02 (3.34E-01)
Absorption	1	1.04E-02 (1.32E+00)	1.04E-02 (9.24E-01)
	2	1.05E-01 (6.39E-01)	1.05E-01 (1.92E-01)
Scattering	1	5.26E-01 (7.23E-01)	5.29E-01 (9.32E-01)
	2	1.23E+00 (1.38E-01)	1.20E+00 (1.75E-01)
Nufission	1	7.45E-03 (-)	7.50E-03 (6.61E-01)
	2	1.53E-01 (-)	1.54E-01 (4.52E-01)

Table 6.20: Macroscopic cross-sections for MOX fuel assembly

Reaction	Energy gr.	TSUNAMI [cm^{-1}]	SAMPLER [cm^{-1}]
Total	1	5.28E-01 (-)	5.28E-01 (9.35E-01)
	2	1.42E+00 (-)	1.42E+00 (1.41E-01)
Fission	1	2.67E-03 (6.50E-01)	2.66E-03 (6.40E-01)
	2	1.11E-01 (7.30E-01)	1.11E-01 (7.81E-01)
Absorption	1	1.12E-02 (1.33E+00)	1.11E-02 (9.28E-01)
	2	2.01E-01 (8.23E-01)	2.01E-01 (3.00E-01)
Scattering	1	5.17E-01 (9.20E-01)	5.17E-01 (9.38E-01)
	2	1.22E+00 (1.63E-01)	1.22E+00 (1.70E-01)
Nufission	1	7.58E-03 (-)	7.55E-03 (9.83E-01)
	2	3.18E-01 (-)	3.17E-01 (1.22E+00)

content of plutonium may affect the results of an uncertainty analysis, four unit cells have been studied. The pincell with gadolinium, named GD1, has an enrichment of 3.6 wt% of ^{235}U and an overall content of 4.0 wt % of Gd_2O_3. The gadolinium is composed by seven isotopes, but two of them have a predominant significance: ^{155}Gd and ^{157}Gd. The three pincells with plutonium, namely PU1, PU2 and PU3, have respectively a 2.0 wt %, 3.0 wt % and a 4.2 wt % of fissile plutonium (consisting of 93 wt % of ^{239}Pu).

Table 6.21: Values of the k-eff and its uncertainty for gadolinium unit cell

TSUNAMI	Uncertainty [%]	SAMPLER	Uncertainty [%]
0.36112	1.24	0.33372	1.36

Table 6.22: Values of the k-eff and its uncertainty for plutonium unit cells

TSUNAMI	Uncertainty [%]	SAMPLER	Uncertainty [%]
PU1			
1.13092	1.11	1.17013	1.07
PU2			
1.16638	1.10	1.20916	1.06
PU3			
1.19461	1.09	1.23747	1.05

Tables 6.21 and 6.22 show the values of k-eff for the gadolinium unit cell and for the three plutonium unit cells, respectively. These tables show also the uncertainties associated to the values of k-eff. By comparing the uncertainties given in these tables with those of LWRs unit cells in table 6.8,

it is possible to notice that the presence of plutonium or gadolinium in the pin induces a doubling of the uncertainty.

The five cross-sections which contribute the most to the k-eff uncertainty are given in table 6.23. It is interesting that the ^{238}U(n,γ) reaction, which is the most important contribution to the uncertainty of uranium unit cells (see figure 6.3), is no more present in the ranking of the gadolinium unit cell and has an importance which descreases with the increase of the plutonium content in the plutonium unit cells. Moreover the capture reactions of ^{155}Gd and of ^{157}Gd, as expected, have a great relevance in pincells with gadolinium and enter the ranking in fourth and fifth place.

As far as the plutonium pins are concerned, the most important contribution is given by ^{239}Pu nubar, followed by the capture of ^{238}U and ^{239}Pu, with the exception of PU3 in which the capture of ^{239}Pu overcomes the capture of ^{238}U.

Table 6.23: Highest contributions to the k-eff uncertainty for gadolinium and MOX unit cells

Covariance matrix		Uncertainty [%]
Nuclide-Reaction	Nuclide-Reaction	
GD1		
^{238}U (n,n')	^{238}U (n,n')	9.54E-01
^{235}U chi	^{235}U chi	5.10E-01
^{238}U nubar	^{238}U nubar	2.81E-01
^{157}Gd (n,γ)	^{157}Gd (n,γ)	2.37E-01
^{155}Gd (n,γ)	^{155}Gd (n,γ)	2.09E-01
PU1		
^{239}Pu nubar	^{239}Pu nubar	8.89E-01
^{238}U (n,γ)	^{238}U (n,γ)	3.11E-01
^{239}Pu (n,γ)	^{239}Pu (n,γ)	2.86E-01
^{239}Pu fission	^{239}Pu fission	2.74E-01
^{239}Pu fission	^{239}Pu (n,γ)	2.66E-01
PU2		
^{239}Pu nubar	^{239}Pu nubar	8.99E-01
^{238}U (n,γ)	^{238}U (n,γ)	2.84E-01
^{239}Pu (n,γ)	^{239}Pu (n,γ)	2.84E-01
^{239}Pu fission	^{239}Pu fission	2.59E-01
^{239}Pu fission	^{239}Pu (n,γ)	2.50E-01
PU3		
^{239}Pu nubar	^{239}Pu nubar	9.04E-01
^{239}Pu (n,γ)	^{239}Pu (n,γ)	2.75E-01
^{238}U (n,γ)	^{238}U (n,γ)	2.65E-01
^{239}Pu fission	^{239}Pu fission	2.50E-01
^{238}U (n,n')	^{238}U (n,n')	2.33E-01

Chapter 7

Conclusions

The burnup analysis phase of the work presented in this thesis covers several aspects of the burnup calculations with both Monte Carlo and deterministic codes. The OECD VVER-1000 LEU and MOX burnup computational benchmark has been analyzed by means of the SERPENT and SCALE codes and new solutions have been produced using ENDF/B-VII and JEFF3.1 nuclear data libraries. The comparison of our results with the ones available in literature shows generally a good agreement over all the reactor states considered in terms of reactivity values, pin-by-pin fission rates distributions and nuclide concentration.

The SERPENT models for the LEU and MOX assemblies have also been tested with JEFF2.2 data and the corresponding results show excellent agreement with previously obtained MCNP4B/JEFF2.2 solutions making of this work also a new Monte Carlo reference solution for the benchmark exercise with modern NDLs.

The accuracies and performances of depletion algorithms for full systems of nuclides have been evaluated in the SERPENT code. In particular, the higher order Stochastic Implicit Euler (SIE) algorithm, implemented only in the latest version of the code, has been compared with the more validated Predictor-corrector algorithm. The results show that the former has still some problem in the prediction of the k-inf values, both with LEU and MOX assembly.

A sensitivity study on the division of the burnup steps into substeps has been performed and the results have been described. This analysis states that a small improvement ($\sim$ 100 pcm) in the results of calculations of k-inf can be achieved in assemblies with gadolinium bearing pins. This outcome confirms the results of Lee, Rhodes, and Smith 2013, even if our differences in the k-inf values are less significant than those reported in that article. This is probably due to the lower number of gadolinium bearing pins in our assemblies (12) than that of the article (17).

The effects of a gadolinium pin mesh refinement in the SCALE code have

been studied. The improvement in the reactivity values has been found to be negligible (~ 20).

The neutronics modelling of some selected test cases within the "Neutronics Phase" of the OECD UAM Benchmark and of the LEU and MOX assemblies of the OECD VVER-1000 burnup computational benchmark has been presented. A S/U analysis on the impact of the uncertainty in the basic nuclear data on the calculation of the multiplication factor and microscopic and macroscopic cross-sections have been performed using the perturbation methodologies and the statistical sampling methodology.

The just released implementation of the GRS method within the SCALE package has been used and compared against TSUNAMI over an extensive number of test cases representative of LWRs configurations (and particularly of VVER-type).

The values and the associated uncertainties of the k-eff computed for the unit cells, both in Hot Full Power and in Hot Zero Power conditions, show a good agreement between the two codes. The uncertainties have been evaluated to be 0.5%–0.6% for all the test cases. The absorption and fission microscopic cross-sections of ^{235}U and ^{238}U have been calculated only with the TSUNAMI code and the associated uncertainties have been found to be higher (up to $\sim 4\%$) than those for the k-eff.

Some homogenized macroscopic cross-sections (total, absorption, fission and scattering) have been calculated with both codes and the associated uncertainties have been estimated to be between $\sim$ 1%–4%.

By analysing the unit cells with gadolinium and plutonium, we have found that the presence of these elements cause a doubling of the uncertainty related to the values of k-eff.

The explicit and implicit contributions to the total sensitivity coefficient of the five cross-sections which contribute the most to the k-eff uncertainty have been presented.

The ^{238}U capture cross-section and the ^{239}Pu nubar were found to be the highest contributors to the total uncertainty for the UOX and MOX LWR's representative test cases. Moreover, the ^{238}U (n,n') cross-section had the most important contribution to the total uncertainty for the gadolinium bearing pins. The capture reactions of the two most significant gadolinium isotopes, ^{155}Gd and ^{157}Gd, also represented a relevant contribution to the total uncertainty of this type of fuel pin.

We have shown some of the capabilities that make of the SAMPLER code an interesting alternative to the TSUNAMI code, but more generally to all those codes based on the perturbation theory. The correlation matrix allows to have a better understanding of the physics of the problem, while the statistical sampling methodology permits to gather informations about the uncertainty of every desired parameter without any increase of the computational time (or with a meaningless one).

7.1 Future perspectives

The results of the OECD VVER-1000 LEU and MOX burnup computational benchmark are quite conclusive, while the S/U analysis did not include some results requested by the OECD UAM benchmark and only some of the proposed test cases have been studied.

The informations provided in Chapter 6 can be useful for a more extensive analysis of the cases and to extend the study to the core level foreseen by the Exercise I-3 of the benchmark.

Some of the functionalities described in the SAMPLER manual are not yet implemented in the actual beta version of the code. The calculation of the microscopic cross-sections with SAMPLER will be possible as soon as the corresponding module will be implemented. The study, suggested by the OECD UAM Benchmark, of the uncertainties associated to little perturbations of geometrical parameters (e.g., radius of the fuel rod and of the cladding) and material compositions will be also feasible with the next versions of this code.

Bibliography

Alioshin, S.S. et al. (2001). *VVER-1000 Gadolinium Core with 30 % MOX*. Oak Ridge, Tennesse: Presentation at the American-Russian Technical Meeting on MOX Fuel Disposition in VVER-1000.

Ball, Matthew Ryan (2011). 'Uncertainty in Lattice Reactor Physics Calculations'. PhD thesis. Hamilton, Ontario, Canada: McMaster University.

Bateman, Harry (1910). 'Solution of a system of differential equations occurring in the theory of radio-active transformations'. In: *Math. Proc. Cambridge* 15, pp. 423–427.

Bevington, Philip R. and Keith Robinson (2002). *Data Reduction and Error Analysis for Physical Sciences*. ISBN 0-07-247227-8, Third edition. McGraw-Hill.

Bonavigo, L. and M. De Salve (2011). *Issues for Nuclear Power Plants Steam Generators*. URL: `http://www.intechopen.com/books/steam-generator-systems-operational-reliabilityand-%20efficiency/issues-for-nuclear-power-plants-steam-generators`.

Brown, Forrest (2006). *On the Use of Shannon Entropy of the Fission Distribution for Assessing Convergence of Monte Carlo Criticality Calculations*. Vancouver, BC, Canada: PHYSOR-2006, ANS Topical Meeting on Reactor Physics.

— (2009). *A Review of Best Practices for Monte Carlo Criticality Calculations*. Richland, WA, USA: American Nuclear Society 2009 Nuclear Criticality Safety Topical Meeting.

Cacuci, Dan G. (2003). *Sensitivity and Uncertainty Analysis: Theory*. ISNB 1-58488-115-1. Boca Raton, Florida, USA: Chapman and Hall/CRC.

Cacuci, Dan G., M. Ionescu-Bujor, and M. I. Navon (2005). *Sensitivity and Uncertainty Analysis: Applications to Large Scale Systems*. Vol. 2. Boca Raton, Florida, USA: Chapman & Hall/CRC.

Cetnar, J. (2006). 'General solution of Bateman equations for nuclear transmutations'. In: *Annals of Nuclear Energy* 33, pp. 640–645.

Chadwick, M.B. et al. (2006). 'ENDF/B-VII.0: Next Generation Evaluated Nuclear Data Library for Nuclear Science and Technology'. In: *Nuclear Data Sheets* 12. ISBN 926402314-3, pp. 2931–3060.

D'Auria, F. (2012). *The origins of the uncertainty*. Conference at Daejeon, South Korea.

DeHart, M.D. and Bowman S.M. (2011). 'Reactor physics methods and analysis capabilities in SCALE'. In: *Nuclear technology* 174, pp. 196–213.

Dufek, J. and W. Gudowski (2006). 'Stochastic approximation for Monte Carlo calculation of steady-state conditions in thermal reactors'. In: *Nuclear Science and Engineering* 152, pp. 274–283.

Dufek, J. and J.E. Hoogenboom (2009). 'Numerical Stability of Existing Monte Carlo Burnup Codes in Cycle Calculations of Critical Reactors'. In: *Nuclear Science and Engineering* 162, pp. 307–311.

Dufek, J., D. Kotlyar, et al. (2013). 'Numerical Stability of the Predictor-Corrector Method in Monte Carlo Burnup Calculations of Critical Reactors'. In: *Annals of Nuclear Energy* 56, pp. 34–38.

Gandini, A. (1967). 'A generalized perturbation method for bi-linear functionals of the real and adjoint neutron fluxes'. In: *Journal of Nuclear Energy* 21.10, pp. 755–765.

— (2014). *Lezioni di Ingegneria del Nocciolo*. Chapter 11. URL: `http://xoomer.virgilio.it/augandin/University/Indice.htm`.

Gauld, I.C. et al. (2011). 'Isotopic depletion and decay methods and analysis capabilities in SCALE'. In: *Nuclear technology* 174, pp. 169–195.

Gehin, J.C. et al. (2004). *Issues in the Use of Weapons-Grade MOX Fuel in VVER-1000 Nuclear Reactors: Comparison of UO_2 and MOX Fuels*. ORNL/TM-2004/223.

Gehin J.C.and Carbajo, J.J. and R.J. Ellis (2004). *Issues in the Use of Weapons-Grade MOX Fuel in VVER-1000 Nuclear Reactors: Comparison of UO2 and MOX Fuels*. Oak Ridge National Laboratories. Oak Ridge, Tennesse.

Gidropress website (2014). URL: `http://www.gidropress.podolsk.ru/en/projects/wwer1000.php`.

Glaeser, Horst (2008). 'GRS Method for Uncertainty and Sensitivity Evaluation of Code Results and Applications'. In: *Science and Technology of Nuclear Installations*.

Greene, N.M., L.M. Petrie, and M.L. Williams (2011). *XSDRNPM: A One-Dimensional Discrete-Ordinates Code for Transport Analysis*. Version 6.1. Oak Ridge National Laboratories. Oak Ridge, Tennesse. Chap. F03.

Guerrini, Bruno and Sandro Paci (1998). *Appunti di impianti nucleari*. Vol. I: aspetti generali. Chapter 4, pagg. 206-209. Pisa: SEU.

International nuclear society website (2014). URL: `http://insp.pnnl.gov/-profiles-reactors-vver230.htm`.

InternationalAtomicEnergyAgency, ed. (2011). *Status report 93 - VVER – 1000*.

Isotalo, A.E. (2011). 'Comparison of depletion algorithms for large systems of nuclides'. In: *Annals of Nuclear Energy* 38, pp. 261–268.

— (2013). 'Computational methods for burnup calculations with Monte Carlo neutronics'. PhD thesis. Aalto university.

Isotalo, A.E. and P.A. Aarnio (2011a). 'Higher order methods for burnup calculations with Bateman solutions'. In: *Annals of Nuclear Energy* 38, pp. 1987–1995.

— (2011b). 'Substep methods for burnup calculations with Bateman solutions'. In: *Annals of Nuclear Energy* 38, pp. 2509–2514.

Isotalo, A.E., J. Leppänen, and J. Dufek (2013). 'Preventing xenon oscillations in Monte Carlo burnup calculations by enforcing equilibrium xenon distribution'. In: *Annals of Nuclear Energy* 60, pp. 78–85.

Ivanov, B. et al. (2002). *VVER-1000 Coolant Transient Benchmark (V1 000-CT). Phase 1 – Final Specification*. NEA/NSC/DOC (2002)6.

Ivanov, K., A. Avramova, et al. (2013). *Benchmark for Uncertainty Analysis in Modelling (UAM) for the Design, Operation and Safety Analysis of LWRs*. NEA/NSC/DOC (2013) 7.

Ivanov, K., T. Beam, et al. (1999). *PWR MSLB Benchmark. Volume 1: Final Specifications*. NEA/NSC/DOC (99)8.

Jesse, M.A. and M.D. DeHart (2011). *TRITON: a multipurpose transport, depletion and sensitivity and uncertainty analysis module*. Version 6.1. Oak Ridge National Laboratories. Oak Ridge, Tennesse. Chap. T1.

Kalugin, M. et al. (2002). *VVER-1000 LEU and MOX Assembly Computational Benchmark*. NEA/NSC/DOC (2002) 10.

Krzykacz, B., E. Hofer, and M. Kloos (2014). *A Software System for Probabilistic Uncertainty and Sensitivity Analysis of Results from Computer Models*. PSAM-II, San Diego, California, USA.

Lamarsh, John R. (1966). *Introduction to Nuclear Reactor Theory*. ISNB 0201041200. Addison-Wesley Publishing Company.

Lee, D., J. Rhodes, and K. Smith (2013). 'Quadratic Depletion Method for Gadolinium Isotopes in CASMO-5'. In: *Nuclear Science and Engineering* 174, pp. 79–86.

Leppänen, J. (2007). 'Development of a New Monte Carlo Reactor Physics Code'. In: 640.

— (2008). *PSG20Serpent—A Continuous-Energy Monte Carlo Reactor Physics Burnup Calculation Code*. available on the Internet at http:00montecarlo.vtt.fi VTT Technical Research Centre of Finland.

Leppänen, J. and M. Pusa (2009). *Burnup calculation capability in the PSG2/ Serpent Monte Carlo reactor physics code*. Saratoga Springs, New York: International Conference on Mathematics, Computational Methods, Reactor Physics.

Lewins, J. (1960). 'Time dependent importance of neutrons and precursors'. In: *Nuclear Science and Engineering* 7, p. 268.

Lewis, E.E. and W.F. Miller (1984). *Computational Methods of Neutron Transport*. ISNB 0-89448-452-4. Wiley-Interscience.

Library, The JEFF2.2 Nuclear Data (2000). *NEA/JEFF Report 17*.

Library, The JEFF3.1 Nuclear Data (2006). *NEA/JEFF Report 21*. ISBN 926402314-3.

Lux, Ivan and Laszlo Koblinger (1991). *Monte Carlo Particle Transport Methods: Neutron and Photon Calculations*. ISNB 0-8493-6074-9. CRC press: EDP sciences.

Mahlers, Y.P. (2009). 'VVER-1000 neutronics calculation with ENDF/B-VII data'. In: *Annals of Nuclear Energy* 36, pp. 1224–1229.

Mercatali, L. (2013). 'SCALE Modeling of Selected Neutronics Test Problems within the OECD UAM LWR's Benchmark'. In: *Science and Technology of Nuclear Installations*.

Mervin, Brenden T. and Guillermo I. Maldonado (2011). *Uncertainty analysis for localized tallies in Monte Carlo eigenvalue calculations*. Rio de Janeiro, Brazil: International Conference on Mathematics, Computational Methods Applied to Nuclear Science, and Engineering.

Metropolis, N. (1987). 'The Beginning of the Monte Carlo Method'. In: *Los Alamos Science*, pp. 125–130.

NationalRegulatoryAgency, ed. (2011). *European stress test for nuclear power plants, National report of Bulgary.*

NEA website (2014). URL: `http://www.oecd-nea.org/tools/abstract/detail/ccc-0750`.

Nikolay, F. (2013). *VVER design overview.* Putra Jaya, Malaysia: IAEA Safety Assessment Education and Training Program, Essential Knowledge Workshop on Safety Analysis Report.

OECD/NEA Data Bank Computer Program Services (2014). URL: `www.oecd-nea.org/tools/abstract/detail/nea-1840`.

ORNL/TM-2005/39, Version 6.1. Oak Ridge National Laboratory. Radiation Safety Information Computational Center at Oak Ridge National Laboratory as CCC-785, ed. (2011). *SCALE: A Comprehensive Modeling and Simulation Suite for Nuclear Safety Analysis and Design.*

Palmiotti, G. and M. Salvatores (2012). 'Developments in Sensitivity Methodologies and the Validation of Reactor Physics Calculations'. In: *Science and Technology of Nuclear Installations.*

Pavlovitchev, A.M. et al. (2000). *Kinetics Parameters of VVER-1000 Core with 3 MOX Lead Test Assemblies to be used for Accident Analysis Codes.* Kurchatov Institute.

— (2004). *Analysis of Alternative In-Core Fuel Core Management with Increased Disposition Pu Rate in VVER-1000.* Kurchatov Institute: Final Report for Task 2 of Work Release KI-WR13JCG.

Pavlovitchev, A.M. et al. (2001). *Mission Fuel Kinetics Input and RELAP-Like Calculations of VVER-1000.* Oak Ridge National Laboratories. Oak Ridge, Tennesse.

Petrov, N., G. Todorova, and N.P. Kolev (2013). 'APOLLO2 and TRIPOLI4 solutions of the OECD VVER-1000 LEU and MOX assembly benchmark'. In: *Annals of Nuclear Energy* 55, pp. 93–107.

Pusa, M. and J. Leppänen (2010). 'Computing the matrix exponential in burnup calculations'. In: *Nuclear Science and Engineering* 164, pp. 140–150.

Rearden, B.T. (2011). *TSUNAMI-3D: CONTROL MODULE FOR THREE-DIMENSIONAL CROSS-SECTION SENSITIVITY AND UNCERTAINTY*

ANALYSIS FOR CRITICALITY. Version 6.1. Oak Ridge National Laboratories. Oak Ridge, Tennesse. Chap. C09.

Rearden, B.T., M.E. Dunn, et al. (2013). *Overview of SCALE 6.2*. NCSD-2013 Conference, Wilmington, North Carolina, USA: Oak Ridge National Laboratory.

Rearden, B.T., M.A. Jesse, and L.M. Williams (2011). *TSUNAMI-1D: CONTROL MODULE FOR ONE-DIMENSIONAL CROSS-SECTION SENSITIVITY AND UNCERTAINTY*. Version 6.1. Oak Ridge National Laboratories. Oak Ridge, Tennesse. Chap. C08.

Rearden, B.T., L.M. Petrie, and M.A. Jessee (2011). *SAMS: Sensitivity Analysis Module for SCALE*. Version 6.1. Oak Ridge National Laboratories. Oak Ridge, Tennesse. Chap. F22.

Rearden, B.T., M.L. Williams, et al. (2011). 'SENSITIVITY AND UNCERTAINTY ANALYSIS CAPABILITIES AND DATA IN SCALE'. In: *Nuclear Technology* 174, pp. 236–288.

Reuss, Paul (2008). *Neutron physics*. ISNB 9782759800414. Les Ulis: EDP sciences.

ROSATOM, ed. (2013). *The VVER today: Evolution, Design, Safety*.

Rose, P.F. (1991). *ENDF-201, ENDF/B-VI Summary Documentation*. BNL-NSC-17541, 4th edition.

Rutherford, Ernest (1905). *Radio-Activity*. Second Edition. Cambridge University Press.

SCALE website (2014). URL: `http://scale.ornl.gov/index.shtml`.

SERPENT website (2014). URL: `http://montecarlo.vtt.fi`.

Current Reactor Technology, Part III (2010). Czech Technical University Prague.

Solis, J. et al. (2001). *BWR TT Benchmark. Volume I: Final Specifications*. NEA/NSC/DOC (2001)1.

Spanier, J. and E.M. Gelbard (2008). *Monte Carlo Principles and Neutron Transport Problems*. ISNB 0486462935. Dover Publications.

Stacey, W.M. (2001). *Nuclear reactor physics*. ISBN 0-471-39127-1. New York: John Wiley and sons, Inc.

Team, X-5 Monte Carlo (2005). *MCNP – A General N-Particle Transport Code, Version 5 – Volume 1: Overview and Theory*. Los Alamos, USA: Los Alamos National Laboratory.

Thilagam, L. et al. (2009). 'A VVER-1000 LEU and MOX assembly computational benchmark analysis using the lattice burnup code EXCEL'. In: *Annals of Nuclear Energy* 36, pp. 505–519.

Trkov, A., G.L. Molnár, and Z. Révay (2005). 'Revisiting the ^{238}U thermal capture cross section and gamma-ray emission probabilities from ^{239}Np decay'. In: *Nuclear Science and Engineering* 150.3, pp. 336–348.

Trunov, N. B et al. (2008). 'Steam generators – horizontal or vertical (which type should be used in nuclear power plants with VVER?)' In: *Atomic Energy* 105.3.

Usachev, L.N. (1955). *Equation for the value of neutrons, reactor kinetics and perturbation theory*. Vol.5, pag. 503. Geneva, Switzerland: Proceedings of the International Conference on the Peaceful Uses of Atomic Energy.

— (1963). 'Perturbation theory for the breeding factor, and other ratios of a number of different processes in a reactor'. In: *Atomic Energy* 15.6, p. 472.

VVER page on Wikipedia (2014). URL: `http://en.wikipedia.org/wiki/VVER`.

Weinberg, A. and E. Wigner (1958). *The Physical Theory of Neutron Chain Reactors*. The University of Chicago Press.

Wilks, S.S. (1941). 'Determination of sample sizes for setting tolerance limits'. In: *Annals of Mathematical Statistics* 12.1, pp. 91–96.

— (1942). 'Statistical prediction with special reference to the problem of tolerance limits'. In: *Annals of Mathematical Statistics* 13.4, pp. 400–409.

Williams, M.L. (2011). 'Resonance Self-Shielding Methodologies in SCALE'. In: *Nuclear Technology* 174.

Williams, M.L., Frantisek Havluj, et al. (2013). *SCALE Uncertainty Quantification Methodology for Criticality Safety Analysis of Used Nuclear Fuel*. NCSD-2013 Conference, Wilmington, North Carolina, USA: Oak Ridge National Laboratory.

Williams, M.L., G. Ilas, et al. (2013). 'A Statistical Sampling Method for Uncertainty Analysis with SCALE and XSUSA'. In: *Nuclear Technology* 183, pp. 515–526.

Williams, M.L. and B.T. Rearden (2008). 'Sensitivity/Uncertainty Analysis Capabilities and New Covariance Data Libraries in SCALE'. In: *Nuclear Data Sheets* 109.

BIBLIOGRAPHY

Williams, M.L., D. Wiarda, et al. (2011). *SCALE Nuclear Data Covariance Library*. ORNL/TM-2005/39. Oak Ridge, Tennesse.

Zaritsky, S.M. et al. (2004). *Results of RPV Fluence Calculations*. Kurchatov Institute.

Appendix A

TRITON input example

In this and in the following appendices some inputs for TRITON, TSUNAMI and SAMPLER are presented as examples. The input for the SERPENT code is not included in these appendices for its lenght (more than 5000 lines). This appendix contains the input for the LEU assembly of the OECD VVER-1000 LEU and MOX burnup computational benchmark.

LEU assembly input with TRITON

```
=t-depl parm=(addnux=3,centrm)
LEU burnup
v7-238
read comp
'U rod
u-235 1 0 8.6264e-04 1027 end
u-238 1 0 2.2169e-02 1027 end
o-16  1 0 4.6063e-02 1027 end
'U/Gd rod
u-235  11 0 7.2875e-04 1027 end
u-238  11 0 1.9268e-02 1027 end
o-16   11 0 4.1854e-02 1027 end
gd-152 11 0 2.5159e-06 1027 end
gd-154 11 0 2.7303e-05 1027 end
gd-155 11 0 1.8541e-04 1027 end
gd-156 11 0 2.5602e-04 1027 end
gd-157 11 0 1.9480e-04 1027 end
gd-158 11 0 3.0715e-04 1027 end
```

```
gd-160 11 0 2.6706e-04 1027 end
'cladding
wtptzr-nb   2 6.44 3 40000 99 41000 0.98 72000
                          0.02 1 575 end
wtptzr-nb  12 6.44 3 40000 99 41000 0.98 72000
                          0.02 1 575 end
'moderator for fuel (with and without gadolinium)
h-1   3 0 4.843E-2 575 end
o-16  3 0 2.422E-2 575 end
b-10  3 0 4.794E-6 575 end
b-11  3 0 1.942E-5 575 end
h-1  13 0 4.843E-2 575 end
o-16 13 0 2.422E-2 575 end
b-10 13 0 4.794E-6 575 end
b-11 13 0 1.942E-5 575 end
end comp
read celldata
latticecell triangpitch hpitch=0.6375  3
                fuelr=0.386 1 cladr=0.4582  2 end
latticecell triangpitch hpitch=0.6375 13
                fuelr=0.386 11 cladr=0.4582 12 end
end celldata
read depletion
101 102 111 112 end
assign  1 101 102 end
assign 11 111 112 end
end depletion
read burndata
power=35.88399169 burn=27.86757975 down=0 nlib=1 end
power=35.88399169 burn=0.1          down=0 nlib=1 end
....
power=35.88399169 burn=139.3378987 down=0 nlib=1 end
power=35.88399169 burn=0.1          down=0 nlib=1 end
power=35.88399169 burn=139.3378987 down=0 nlib=1 end
power=35.88399169 burn=0.1          down=0 nlib=1 end
end burndata
```

```
read opus
matl=101 102 111 112 end
sort=no
units=atoms time=days typarms=nucl libtyp=all
title= Fuel concentrations of nuclides
symnuc=u-232 u-235 u-236 u-238
       pu-236 pu-238 pu-239 pu-240 pu-241 pu-242
       cm-244 ce-137 xe-135 sm-149 gd-155 gd-157 end
end opus
read model
Infinite lattice VVER pin cell
read parm
epsilon=1e-3 sn=6 converg=mix
drawit=yes echo=yes xnlib=4
run=yes clearint=no combine=yes
end parm
read materials
mix=101 pn=1 com='UO2 pin'     end
mix=102 pn=1 com='UO2 pin'     end
mix=111 pn=1 com='UO2/Gd pin' end
mix=112 pn=1 com='UO2/Gd pin' end
mix=2   pn=1 com='Zr-Nb'       end
mix=3   pn=2 com='water'       end
end materials
read homog
500 all 101 102 111 112 2 3 end
end homog
read collapse
200r1 38r2
end collapse
read geom
unit 1
com='UO2 Fuel Rod'
cylinder 10 0.3860
cylinder 20 0.4582
hexprism 30 0.6375
```

```
media 101 1 10
media 2   1 20 -10
media 3   1 30 -20
boundary 30    4 4
unit 7
com='UO2 Fuel Rod'
cylinder 10 0.3860
cylinder 20 0.4582
hexprism 30 0.6375
media 102 1 10
media 2   1 20 -10
media 3   1 30 -20
boundary 30    4 4
unit 2
com='UO2/Gd Fuel Rod'
cylinder 10 0.3860
cylinder 20 0.4582
hexprism 30 0.6375
media 111 1 10
media   2 1 20 -10
media   3 1 30 -20
boundary 30    4 4
unit 8
com='UO2/Gd Fuel Rod'
cylinder 10 0.3860
cylinder 20 0.4582
hexprism 30 0.6375
media 112 1 10
media   2 1 20 -10
media   3 1 30 -20
boundary 30    4 4
unit 3
com='Central tube'
cylinder 10 0.48
cylinder 20 0.5626
hexprism 30 0.6375
```

```
media 3 1 10
media 2 1 20 -10
media 3 1 30 -20
boundary 30    4 4
unit 4
com='Guide tube'
cylinder 10 0.545
cylinder 20 0.6323
hexprism 30 0.6375
media 3 1 10
media 2 1 20 -10
media 3 1 30 -20
boundary 30    4 4
unit 9
com='water'
hexprism 30 0.6375
media 3 1 30
boundary 30    4 4
global unit 5
rhexprism 6 11.8
array 1 6 place 12 12 0 0
media 3 1 6
boundary 6     2 2
end geom
read array
ara=1 typ=shexagonal nux=23 nuy=23
fill
0 0 0 0 0 0 9 9 9 9 9 9 9 9 9 9 9 0 0 0 0 0
 0 0 0 0 0 9 1 1 1 1 1 1 1 1 1 1 1 9 0 0 0 0 0
0 0 0 0 0 9 1 1 1 1 1 1 1 1 1 1 1 1 9 0 0 0 0
 0 0 0 0 9 1 1 1 1 1 1 2 1 1 1 1 1 1 9 0 0 0 0
0 0 0 0 9 1 1 1 1 1 1 1 1 1 1 1 1 1 1 9 0 0 0
 0 0 0 9 1 1 1 1 1 1 1 4 1 1 1 1 1 1 1 9 0 0 0
0 0 0 9 1 1 1 1 1 4 1 1 1 1 4 1 1 1 1 1 9 0 0
 0 0 9 1 1 2 1 1 1 1 1 1 2 1 1 1 1 2 1 1 9 0 0
0 0 9 1 1 1 1 4 1 2 1 4 1 1 1 1 4 1 1 1 1 9 0
```

```
 0 9 1 1 1 1 1 1 1 1 1 1 4 1 1 1 1 1 1 1 9 0
0 9 1 1 1 1 1 1 1 4 1 1 1 1 1 2 1 1 1 1 1 1 9
 9 1 1 1 1 1 4 1 1 1 1 3 1 1 1 1 4 1 1 1 1 1 9
0 9 1 1 1 1 1 1 2 1 1 1 1 1 4 1 1 1 1 1 1 1 9
 0 9 1 1 1 1 1 1 1 4 1 1 1 1 1 1 1 1 1 1 1 9 0
0 0 9 1 1 1 1 4 1 1 1 1 4 1 2 1 4 1 1 1 1 9 0
 0 0 9 1 1 2 1 1 1 1 2 1 1 1 1 1 1 2 1 1 9 0 0
0 0 0 9 1 1 1 1 1 4 1 1 1 1 4 1 1 1 1 1 9 0 0
 0 0 0 9 1 1 1 1 1 1 1 4 1 1 1 1 1 1 1 9 0 0 0
0 0 0 0 9 1 1 1 1 1 1 1 1 1 1 1 1 1 1 9 0 0 0
 0 0 0 0 9 1 1 1 1 1 1 8 1 1 1 1 1 1 9 0 0 0 0
0 0 0 0 0 9 1 1 1 1 1 1 1 1 1 1 1 1 9 0 0 0 0
 0 0 0 0 0 9 7 1 1 1 1 1 1 1 1 1 1 9 0 0 0 0 0
0 0 0 0 0 0 9 9 9 9 9 9 9 9 9 9 9 9 9 0 0 0 0 0
end fill
end array
read bounds
all=white
end bounds
end model
end
```

Appendix B

TSUNAMI input example

The input for the unit cell PU1 taken from OECD VVER-1000 LEU and MOX burnup computational benchmark is presented below.

VVER-1000 assembly input with TSUNAMI

```
=tsunami-1d
LEU pincell with Gd
v7-238
read comp
'U/Gd rod
u-235   1 0 4.2672E-5 1027 end
u-238   1 0 2.1025E-2 1027 end
o-16    1 0 4.3047E-2 1027 end
pu-239 1 0 4.2414E-4 1027 end
pu-240 1 0 2.7250E-5 1027 end
pu-241 1 0 4.5228E-6 1027 end
'cladding
wtptzr-nb    2 6.44 3 40000 99 41000 0.98 72000 0.02 end
'moderator for fuel
h-1    3 0 4.843E-2 575 end
o-16   3 0 2.422E-2 575 end
b-10   3 0 4.794E-6 575 end
b-11   3 0 1.942E-5 575 end
end comp
read celldata
latticecell triangpitch hpitch=0.6375  3
```

```
        fuelr=0.386  1 cladr=0.4582  2 end
end celldata
read geometry
cylindrical white white end
1 0.386
2 0.4582
3 0.6375
end geometry
read definitions
response 1 nuclide=92235 reaction=102
mixture=1 micro end response
response 2 nuclide=92235 reaction=18
mixture=1 micro end response
response 3 nuclide=92238 reaction=102
mixture=1 micro end response
response 4 nuclide=92238 reaction=18
mixture=1 micro end response
response 5 unity multimix 1 end
end response
end definitions
read systemresponses
ratio 1 numer 1 2 end denom 5 end
title='U235-abs'  end ratio
ratio 2 numer   2 end denom 5 end
title='U235-fis'  end ratio
ratio 3 numer   1 end denom 5 end
title='U235-capt' end ratio
ratio 4 numer 3 4 end denom 5 end
title='U238-abs'  end ratio
ratio 5 numer   4 end denom 5 end
title='U238-fis'  end ratio
ratio 6 numer   3 end denom 5 end
title='U238-capt' end ratio
end systemresponses
read sams
  prtgeom
```

```
   prtimp
end sams
end
```

Appendix C

SAMPLER input example

The input for the VVER-1000 unit cell in the HFP conditions with 93 samples is presented below.

VVER-1000 unit cell input with SAMPLER

```
=%sampler
read parameters
n_samples=93
library="xn238v7"
perturb_xs = yes
perturb_decay = yes
perturb_yields = yes
csv=yes
print_corr=yes
print_cov=yes
end parameters
read case[c1]
sequence=t-depl parm=(bonami,addnux=0)
VVERpincell model
xn238v7
read composition
uo2 1 den=10.4 1 900 92234 0.0054 92235 3.3
                          92238 96.6946 end
wtptzr-nb 2 6.44 2 40000 99.0 41093 1.0 1 600 end
h2O 3 den=0.7525 1 560 end
he 4 1 900 end
```

```
wtptair 5 0.00129 2 7000 79.0 8016 21.0 1 900 end
end composition
read celldata
latticecell atriangpitch pitch=1.275 3 fuelr=0.378 1
gapr=0.386 4 cladd=0.9100 2 imodr=0.07 5 end
end celldata
read depletion -1 end depletion
read burndata
power=33.58179038 burn=7.4445 down=0 nlib=1 end
end burndata
read model
read materials
mix=1 com='fuel' end
mix=2 com='clad' end
mix=3 com='moderator' end
mix=4 com="gap gas" end
mix=5 com="air" end
end materials
read geom
global unit 1
com='UO2 Fuel Rod'
cylinder 10 0.07
cylinder 20 0.378
cylinder 30 0.386
cylinder 40 0.455
hexprism 50 0.6375
media 5 1 10
media 1 1 20 -10
media 4 1 30 -20
media 2 1 40 -30
media 3 1 50 -40
boundary 50 4 4
end geom
read collapse
150r1 88r2
end collapse
```

```
read homog
500 mini 1 2 3 4 5 end
end homog
read bounds
all=white
end bounds
end model
end sequence
end case
read response[hmgxs]
type = triton
mixture = 1
data = kinf sigma_absorption sigma_capture
sigma_fission sigma_total sigma_elastic nu_fission
nu chi flux kappa_fission end
end response
end
```